MECHNICAL AND THERMAL DAMAGE OF HARD CHROMIUM COATINGS ON 416 STAINLESS STEEL

by

Abdullah Almotairi

Submitted in partial fulfilment of the requirements
for the degree of Master of Applied Science

at

Dalhousie University
Halifax, Nova Scotia
June 2016

To my wonderful wife and family – those who suffered

Table of Contents

List of Tables

List of Figures

Abstract

Hard chromium coating has a wide range of applications in automotive and aerospace industries. However, the open literature lacks a comprehensive study on the failure of hard chromium coatings. This research focuses on the mechanical and the thermal damage of hard chromium coatings on 416 stainless steel. Mechanical damage of hard chromium coatings is first investigated as a function of coating thickness. Then, an investigation of thermal damage of the coating as a function of heat temperature was carried out. A novel method was developed in this research to analyze the strain field occurring in the stainless steel substrate due to spherical indentation.

List of Abbreviations and Symbols Used

Abbreviations

BCC	Body-Centered Cubic
ICP	Inductively Coupled Plasma Mass Spectrometry
SEM	Scanning Electron Microscopy
XRD	X-ray Diffraction
PDF	Powder Diffraction Files
EDS	Energy Dispersive Spectroscopy

Symbols

P	Indentation applied load
P_c	Critical load
ρ	Radial distance
σ_m	Maximum tensile stress
a	Radius of elastic contact
r	Sphere radius
E	Young's modulus
v	Poisson ratio
k	A constant
E'	Young's modulus of the indenter
v'	Poisson ratio of the indenter
P_0	Mean pressure
τ_m	Maximum shear stress
σ_ρ	Stress in direction of radial axis
σ_θ	Stress in direction of θ axis

σ_z	Stress in direction of z
σ_m	Maximum stress
u	A constant
σ_{11}	Maximum principal stress
σ_{22}	Principal hoop stress
σ_{33}	Minimum principal stress
τ_{13}	Maximum shear stress
r_c	Radius of plastic zone
da	Displacement in core diameter
dr_c	Displacement in radius of plastic zone
λ	Wavelength
h	Hour
h_c	Contact depth of penetration
h_l	Total penetration depth
dP/dh	Unloading-curve slop
P_{max}	Maximum load
E^*	System's Young's modulus
H	Hardness
HV	Vickers hardness
K_I	Fracture toughness
l	Crack length
R_a	Average Surface Roughness
Rz	Mean Roughness depth
E_s	Young's modulus of the substrate
E_c	Young's modulus of the coating
A	A proportionality coefficient
d	Coating thickness
B'	A coefficient
R	Radial distance from loading axis

b	Constant coefficient
c	Constant coefficient

Acknowledgements

In the name of Allah, the Most Merciful, the Most Compassionate

First and Foremost praise is to ALLAH, the Almighty, the greatest of all. I would like to thank all those who have helped me during the degree. Foremost, I would like to express my sincere gratitude to my supervisors Prof. Andrew Warkentin and co-supervisor Prof. Zoheir Farhat for the continuous support and encouragement throughout my masters. They provided me with direction, technical support and became more of a mentor and friend, than a professor. There is so much I have learned from them. Thank you again for making this possible. In addition to my supervisors, I would like to thank the rest of my supervisory committee members, Dr. Marek Kujath and Dr. Uday Venkatadri for their time and feedback.

I am thankful to Dr. Md. Aminul Islam for his support during my experimental work. He never hesitated to help me. Thank you for training me on how to run key experiments for my research at the Advanced Tribology Laboratory and elsewhere. My thanks go also to Dr. Al-Mokhtar Mohammed for training me and sharing his knowledge and expertise. I also want to express my appreciation to my friends and collogues for their help, namely Tahrim Alam, Iris and Chenxin Jin. I also would like to acknowledge the Mechanical Engineering staff for their help throughout my time at Dalhousie University, namely Selina Cajolais, Kate Hide, Mark MacDonald and Peter Jones.

I am grateful to the Ministry of Education of Saudi Arabia for providing me with a full scholarship through King Abdullah Scholarship Program. My thanks also go to King Abdullah (may Allah have mercy on him) for launching such a program for the sake of developing the Kingdom of Saudi Arabia. I would like to thank Atlantic Hardchrome Limited and Natural Science and Engineering Research Council (NSERC) (RGPIN/217203-2013 and RGPIN/327449-2012) for funding this project.

Finally, I would like to give special thanks to my wife and love, Alaa, for her continuous support. I know how much she did in order to help me accomplish my goals. She kept encouraging and motivating me during my studies. She did everything possible; she sacrificed, to assist me to complete this degree. I want to thank my motivators, my kids, Rytal and Saad, for whom I work hard in order to provide them with a better life. I hope to raise you very well. I would like to thank my parents for their care and support since childhood. I will do the best just for you, to be proud of me. Thank you to the rest of the family and my loved ones for their support.

Abdullah Almotairi

Halifax, June, 2016

Chapter 1

Introduction

Hard chromium plating has a wide range of applications in the aerospace and automotive industries. Chromium plated components are often used in key applications, such as piston rings, shock absorber rods, and hydraulic shafts. Parts are chromium electroplated when some of the following characteristics are required: low coefficient of friction, high melting point, high hardness, and a resistance to wear and corrosion. The presence of all these properties together in a single metal makes chromium deposits unique. Chromium electrodeposition is also used to salvage or refurbish worn components. For example, when a component is worn out, the component can be plated again with chromium and it will be as good as a new one.

Chromium electroplating is brittle and produces rough surfaces. Therefore, grinding is an essential process in manufacturing of hard chromium electroplated parts since it can produce fine surfaces. It can also remove brittle material more efficiently than other conventional processes, such as turning. Furthermore, grinding can achieve high tolerance that is required by the key application of hard chromium coating. However, during grinding, high forces and heat are involved which may lead to mechanical or thermal damage.

1.1 Motivation

Excessive heating during grinding may introduce damage to the chromium coating and/or the substrate underneath. Unfortunately, the open literature lacks a comprehensive study on the thermal damage of chromium coatings. Therefore, an investigation of the failure mechanism of chromium coatings as a result of thermal damage, caused by heating during service or downstream manufacturing processes such as grinding, is crucial. Furthermore, excessive loads during service may damage the chromium coatings. Hence, it is important to understand the failure mechanism of hard chromium coatings due to mechanical damage, such as impact and denting during service of hard chromium coatings before grinding. Unfortunately, a comprehensive study on the mechanical damage of hard chromium coatings is lacking in the open literature.

1.2 Objectives

The objective of this research work is to:

1. Investigate the mechanical damage of chromium coatings due to spherical indentation as a function of thickness and load

2. Investigate thermal damage of hard chromium coatings as a function of heating temperature and its effects on the mechanical response of the coatings

3. Conduct FIB (focused ion beam) work and SEM observation for a detailed investigation on:

    - Inherent and Indentation cracks interaction

- The strain distribution and direction in the stainless steel substrate due spherical indentation

1.3 Thesis Outline

This thesis consists of 5 chapters. Chapter 2 covers the background information needed to understand the work in this research. An extensive literature review is also provided in this chapter. Chapter 3 presents the substrate material characterization and experimental producers followed in this research. The experimental results acquired from this research work are provided in Chapters 4. The results are also extensively discussed in this chapter. Chapter 5 is the last chapter, in which the summary of the conclusions of this research, contributions and recommendations for future work are presented.

Chapter 2

Background and Literature Review

This chapter will provide readers with background on the content covered throughout this thesis. An extensive literature review on chromium electroplating and its process, indentation damage, and thermal damage is provided.

2.1 Hard Chromium Electroplating Process

Chromium electroplating is different from electroplating of other platable metals. Geng [1] points out that chromium can be deposited only from an aqueous solution that contains chromic acid, water, and one or more catalysts. Another difference is that the anode is not made of chromium as in any other deposition processes in which the anode is made of the same metal to be deposited and sacrificed to replenish the bath for the depleted metal. Instead, the anode in chromium electrodeposition is made of lead or lead alloys [2].

Figure 2-1 shows a schematic diagram of the chromium electroplating process. Geng [1] explains the plating mechanism saying that chromium is electroplated onto an object by connecting a negative charge to the object and dipping it into a solution containing chromic acid. Chromic ions carry a positive charge and are deposited on the object. according to Newby [3] there are basic reactions that occur at cathode and anode. When

the current is connected to the bath, three reactions occur at cathode. The first reaction is the reduction of hexavalent chromium to trivalent chromium, followed by reducing hydrogen ions to hydrogen gas. In the last reaction, hexavalent chromium reduces to chromium metal which is then deposited on the object. The proportion of current ions used in the reduction of hexavalent chromium to chromium metal represents the current efficiency. This proportion is relative to the efficiency of the catalyst used; the more efficient the catalyst, the higher current efficiency can be obtained.

Newby [3] adds that three basic reactions occur at the anode which is usually made of a lead alloy. First, the anode surface oxidizes to form a chocolate-brown lead dioxide. The second reaction is oxygen generation. The third is trivalent chromium that deoxidizes to hexavalent chromium. The later reaction cannot occur without lead dioxide which acts as a catalyst for this reaction.

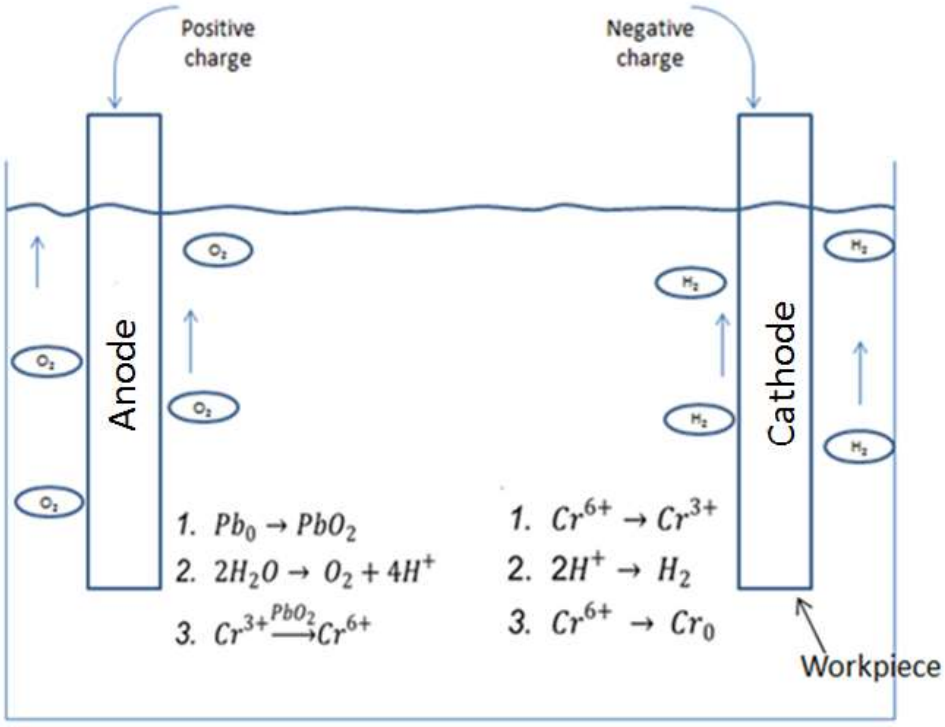

Figure 2-1 Illustration of chromium electroplating process.

Several bath chemistries can be utilized in the process of chromium electroplating. Plating speed and deposit characteristics depend on the particular bath chemistry employed. Process parameters (i.e., current density and bath temperature) involved in electroplating must be well controlled to produce the desired deposit [4]–[6].

2.2 Residual Stress and Inherent Cracks

Chromium is deposited in the form of a pure metal or a metal hydride, depending on solution composition and other operating conditions. The metallic form of chromium has a body-centered cubic (BCC) crystal structure, while the metal hydride takes either a hexagonal or face-centered cubic structure. Hydrides are not stable and decompose to produce BCC chromium metal and hydrogen. The decomposition results in a shrinkage in

volume that induces tensile stress causing the coating to crack [7]. Guffie [2] suggested that internal residual stress increases with coating thickness. When residual stresses exceed the chromium's tensile strength cracking occurs and stress is released. As electrodeposition proceeds, another layer of chromium heals over the existing cracks and stresses start to accumulate again until another set of cracks forms. This cyclic process continues during electroplating. Consequently, healed-over cracks and open cracks are observed on chromium coating surfaces. Dennis et al. [8] explained the cracking mechanism using an instantaneous stress/thickness curve along with images of cracking patterns at different coating thicknesses, where stress increases with thickness and when it cracks, a sharp decrease in stress is observed, as shown in Figure 2-2. Inherent crack density increases with increasing thickness. These cracks do not extend to the base metal. Dennis et al. [8] concluded that inherent cracks are usually preferred in applications, such as hydraulics as they can hold lubricants. However, they can be potential sites for crack propagation. Inherent cracks and residual stress may play a role in mechanical failure, such as impact and denting during service of hard chromium coating.

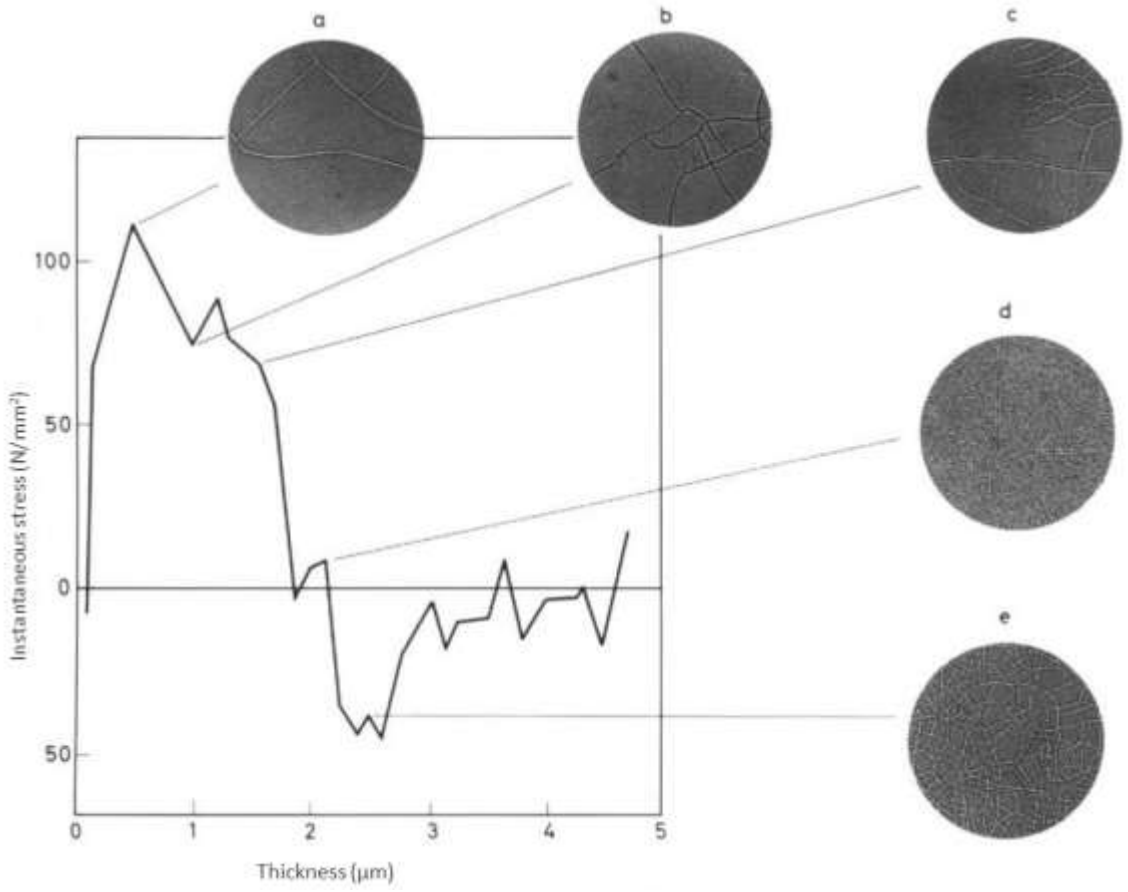

Figure 2-2 Instantaneous stress/thickness curve showing cracking mechanism [8].

2.3 Indentation Damage

Indentation has a variety of applications, one of which is investigation of mechanical damage of materials. In an indentation test, an indenter is applying a specified load at a slow rate perpendicular to the surface of the tested part. When the specified load is reached, the load is maintained for a specified time (generally 10 to 15 second) after which the indenter is unloaded. A diversity of indenters are available for conducting the indentation, such as spheres and Vickers indenters. Indenter shape and other factors may

vary resulting damage (stress distribution) from test to another. A background of mechanical damage due to indentation shall be provided in the next sections.

2.3.1 Monolithic Materials

A variety of cracks may form by indentation contact on brittle materials. Five main types of cracks due to indentation of brittle monolithic materials were identified in the literature [9]. Cone cracks are generated during elastic loading when a blunt indenter is employed. A cone crack is first generated at the surface as a ring at the periphery contact and then it propagates downward and outward at a characteristic angle with the symmetry axis forming a cone-shaped crack. Radial cracks are generated when a sharp indenter or high loading of a blunt indenter is applied. They form during elastic-plastic loading that leaves plastic impression in the surface. In such circumstance, radial cracks might propagate parallel to the loading axis, generally starting at the edge of the impression (commonly at the impression corner). Another type of crack is median cracks that may be formed parallel to the loading axis during elastic-plastic contact, below the quasi plastic zone, bounded by plastic zone or the surface. Lateral cracks can form underneath the plastic deformation zone, parallel to the material surface. Lastly, half-penny cracks are a mixture of median and radial cracks and can develop during unloading. This type of crack begins either with radial cracks propagating downward or median cracks extending upward. The type of cracking present depends on several factors including material, indenter, maximum applied load, and environment. Generally, one cracking system or more may be present in a single indentation event [9]. Chen [10] reported that these types of cracks were identified on brittle thick coatings as well.

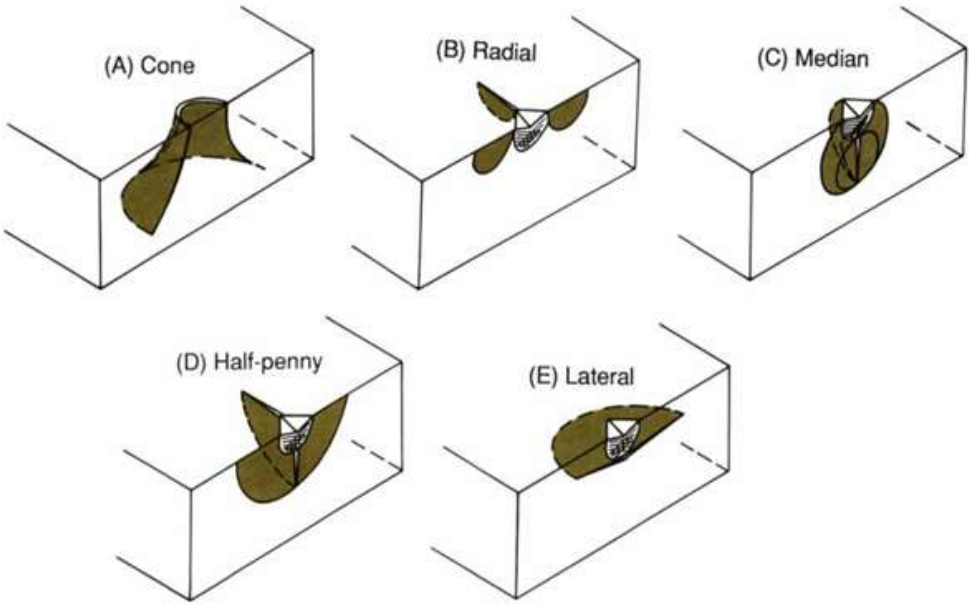

Figure 2-3 **Schematic diagrams showing the crack morphologies of (A) cone Hertzian crack, (B) radial crack, (C) median crack, (D) half-penny crack and (E) lateral crack [9].**

2.3.1.1 Hertzian Contact

Often Hertzian-type contact test is used to evaluate damage mode during contact of brittle monolithic materials and coatings. These tests involve a spherical indenter and flat workpiece surface. It has the advantage of well-developed analytical solutions. It assumes that surfaces are perfectly smooth and that there is no contact friction. In monoliths, two modes of failure are well identified when such testing is employed. The first type is cone (Hertzian) crack that starts on the surface as a ring. If the applied load P exceeds a critical load P_c, the ring crack extends downwards and outwards forming a cone-shape crack as shown in Figure 2-4 [11], [12]. Hertzian cracks form at a radial distance ρ from the contact center, outside the circular contact area of radius a where the maximum tensile stress σ_m is. The radius of elastic contact a can be calculated according to [11],

$$a = \sqrt[3]{\frac{4\,k\,P\,r}{3\,E}} \qquad \text{Equation 2-1}$$

Where r is sphere radius; E is Young's modulus of the material being tested; k is a constant calculated according to,

$$k = \frac{9}{16}\left[(1-v^2) - (1-v'^2)\frac{E}{E'}\right] \qquad \text{Equation 2-2}$$

E' and v' are Young's modulus and the Poisson ratio of the indenter, respectively. v is the Poisson ratio of the tested material. The Hertzian ring crack initiates if the maximum tensile stress σ_m exceeds the strength of the material being indented. Maximum tensile stress σ_m can be found using,

$$\sigma_m = \frac{1}{2}\,(1-2v)\,P_0 \qquad \text{Equation 2-3}$$

where P_0 is the mean pressure that can be calculated according to,

$$P_0 = {}^{P}\!/_{\pi\,a^2} \qquad \text{Equation 2-4}$$

The second failure mode is quasi-plastic occurring in the subsurface below the indenter where the maximum shear stress τ_m is located. The maximum shear stress can be determined using [13],

$$\tau_m = 0.47\,P_0 \qquad \text{Equation 2-5}$$

The maximum shear stress is located at depth l that can be computed using,

$$l = 0.49\,a$$ Equation 2-6

The quasi-plastic mode has the appearance of plastic deformation, but is actually the formation a network of microcracks that are shear-driven [14], [15]. Cracks form perpendicular to stress that exceeds material strength and initiate where the maximum stress is located.

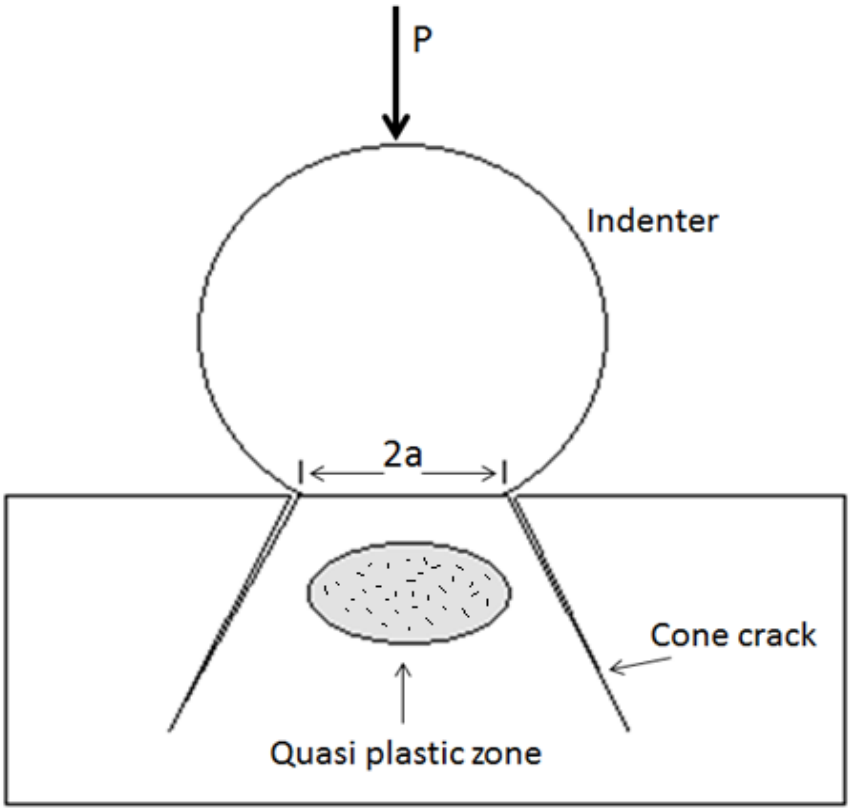

Figure 2-4 **Illustration of Hertzian contact of spherical indenter on brittle materials**

2.3.1.1.1 Stress Distribution

Understanding the stress distribution in the contact zone can help predict crack types (damage mode). Often a Hertzian-type contact test (spherical indenter) is used to evaluate damage mode during contact of monolithic materials and coatings. The stress at any point in the contact filed can be calculated using the following equations [13], where the spherical coordinates of the contact filed are (ρ, Θ, z) about the contact center, as shown in Figure 2-1,

$$\sigma_{\rho\rho}/_{P_0} = \frac{1}{2}(1-2v)\left(\frac{a}{\rho}\right)^2\left[1-\left(z/u^{1/2}\right)^3\right]$$
$$+\left[\frac{3}{2}(z/u^{1/2})\ [(1-v)\,u/(a^2+u)\right.$$
$$\left.+(1+v)\left(u^{1/2}/a\right)\arctan(a/u^{1/2})-2\right]$$

Equation 2-7

$$\sigma_{\theta\theta}/P_0 = \frac{1}{2}(1-2v)\left(\frac{a}{\rho}\right)^2\left[1-\left(z/u^{1/2}\right)^3\right]$$
$$+\left[\frac{3}{2}\left(z/u^{1/2}\right)^3\left[a^2u/(u^2+a^2z^2)\right]\right.$$
$$+\frac{3}{2}(z/u^{1/2})\ [(1-v)\,u/(a^2+u)$$
$$\left.+(1+v)\left(u^{1/2}/a\right)\arctan(a/u^{1/2})\right]+\ 2v]$$

Equation 2-8

$$\sigma_{zz}/P_0 = \frac{3}{2}\,(z/u^{1/2})^3\,[a^2u/(u^2+a^2z^2)] \qquad \text{Equation 2-9}$$

$$\tau_{\rho z} = \frac{3}{2}\,[\,\rho z^2/(u^2+a^2z^2)[a^2u^{1/2}/(a^2+u)] \qquad \text{Equation 2-10}$$

where,

$$u = \frac{1}{2}\,\{(\rho^2 + z^2 + a^2) + [(\rho^2 + z^2 - a^2)^2 + 4\,a^2\,z^2]^{1/2}\} \qquad \text{Equation 2-11}$$

Principal stresses are defined as $\sigma_{11} \geq \sigma_{22} \geq \sigma_{33}$, respectively and can be calculated at any point using [13],

$$\sigma_{11} = \frac{1}{2}\,(\sigma_{\rho\rho} + \sigma_{zz}) + \left\{\left[\frac{1}{2}\,(\sigma_{\rho\rho} + \sigma_{zz})\right]^2 + {\tau_{\rho z}}^2\right\} \qquad \text{Equation 2-12}$$

$$\sigma_{22} = \sigma_\theta \qquad \text{Equation 2-13}$$

$$\sigma_{33} = \frac{1}{2}\,(\sigma_{\rho\rho} + \sigma_{zz}) - \left\{\left[\frac{1}{2}\,(\sigma_{\rho\rho} + \sigma_{zz})\right]^2 + {\tau_{\rho z}}^2\right\} \qquad \text{Equation 2-14}$$

$$\tau_{13} = \frac{1}{2}\,(\sigma_{11} - \sigma_{33}) \qquad \text{Equation 2-15}$$

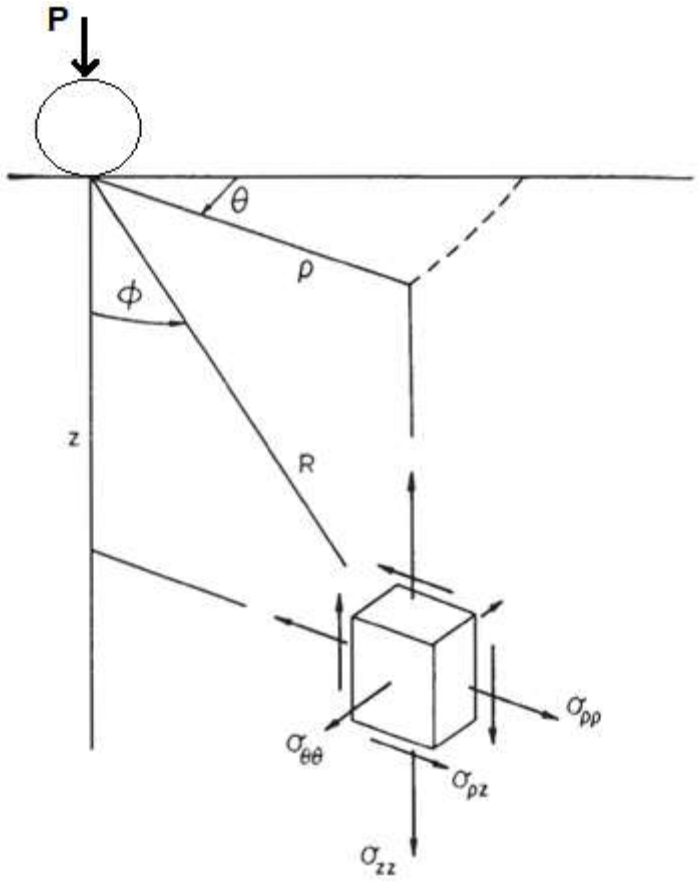

Figure 2-5 Coordinate system of the contact field of spherical indentation [16].

Figure 2-6 (a) and (b) show Hertzian stress trajectories and contours for the principal normal stresses, respectively. The former is used to display principal stress direction, while the latter is to display the principal stress distribution. The upper side of Figure 2-6 (a) is top view of the indention where the black region is the contact area of diameter a-a, whereas the lower part is cross-sectional view of the indention. The applied load has hemisphere distribution within the contact area under which all principle stress are compressive. Principal stress σ_{11} and σ_{33} are axially symmetric in plane with the loading axis. The circular hoop stress (σ_{22}) trajectories are perpendicular to those of σ_{11} in any plane through the axis of symmetry. The principal stress σ_{33} trajectories have a nearly

hyperbolic shape that meets the surface perpendicularly. Figure 2-6 (b) shows the stress contour for σ_{11},σ_{22} , and σ_{33}, respectively. The black region in σ_{11} contours indicates the maximum tensile stress (σ_m) induced by the indenter at a radial distance (ρ) from the center of contact, outside the contact area. The normal principal stress σ_{11} is tensile everywhere except in the compressive zone below the indenter. Hoop stress is tensile outside compressive zone and its trajectories form circles around the axis of symmetry. The principal stress (σ_{33}) is compressive everywhere and zero at any point lying outside the contact circle. Principal stress σ_{11} and σ_{22} cause Hertzian rings and radial cracks to initiate, respectively [11], [12], [16]–[18].

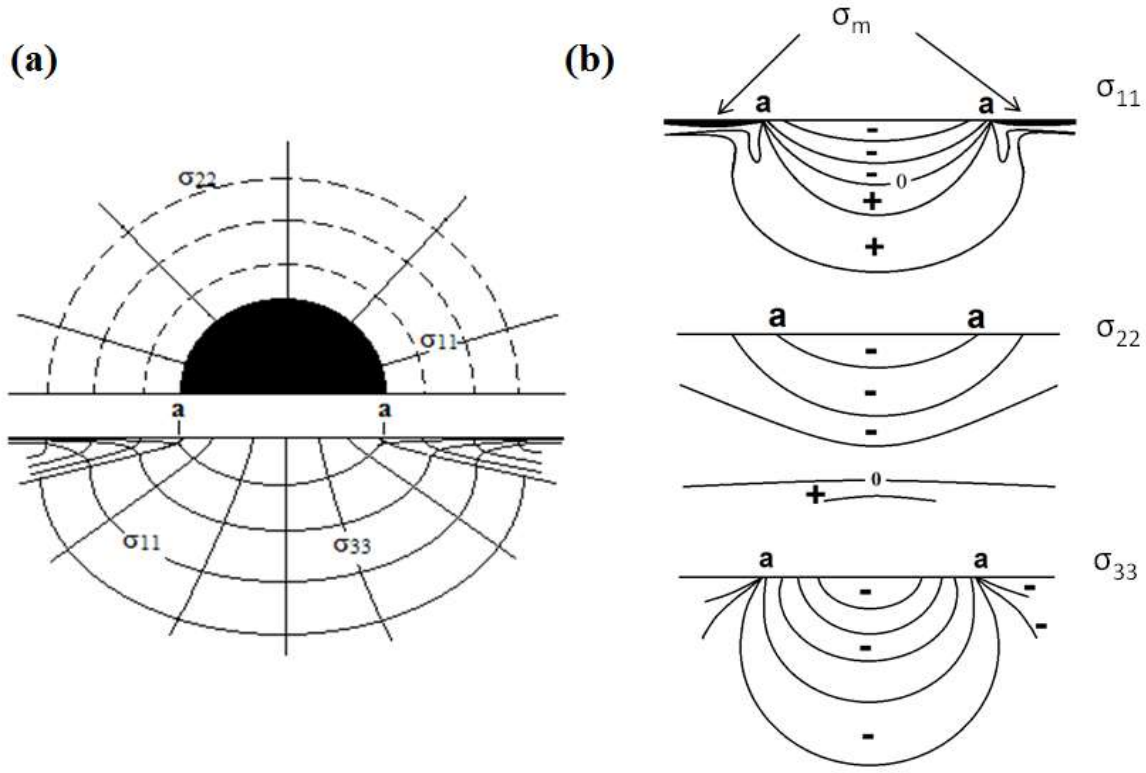

Figure 2-6 **a) Schematic diagram of principal stress trajectories of near-contact field, surface view (top) and side view (bottom), (b) principal stress contours.**

2.3.2 Layered Materials

In addition to monoliths, layered materials are also tested by Hertzian contact. In coatings, failure modes are dependent on a variety of factors including basic mechanical properties (hardness, toughness, modulus of elasticity, and strength), loading conditions, flaw states (i.e. size and density) and geometric factors (i.e. indenter geometry, coating thickness). At low contact loads, the coating controls the mechanical response, while the substrate plasticity dominates the response at higher loads because the quasi-plastic zone, which is a function of load, moves from within the coating into the substrate [14]. For thick coatings fracture dominates the response to the indentation loading because the quasi-plastic zone is contained in the coating. For thin coating, substrate plasticity is the predominant damage mode because the quasi-plastic zone falls in the substrate [15], [19], [20]. Although studies of indentation behavior for hard chrome coatings are sparse, a substantial body of work on indentation of brittle materials and coatings exists.

Brittle coatings on relatively soft materials (i.e. chromium coating on 416 stainless steel as the case in this work) are generally preferred so that the energy of contact loading can be somehow divided between coating fracture and substrate plastic deformation. However, having a strong adhesion is vital, to avoid coating delamination [15]. Damage modes of brittle coatings on compliant substrates shall be emphasized in this present work.

2.3.2.1 Damage Modes

Contact testing is a good method for identifying weakness in coatings [14]. In addition to the two modes described earlier (Hertzian ring and quasi plasticity), a third mode may

emerge when a coating is tested with Hertzian contact. This mode takes a form of radial cracks that initiate at the bottom surface of the coating and extend upwards. It is caused by the coating flexure as the substrate deforms followed by coating deflection in response to the contact loading. This mode generally takes place in an intermediate coating thickness region [21]–[23]. Previous studies [21], [24] indicate that radial cracking occurring at lower coating surface below the indenter is regarded as the most dangerous mode because it can initiate at lower loads than quasi-plastic and cone cracking for intermediate coating thicknesses. It is also hard to detect by a routine inspection as they are not visible on the surface. Therefore, it can be hard to anticipate this type of failure. In addition to Hertzian ring cracks, surface ring cracks due to bending of the coating may occur on brittle coatings on compliant substrate. Bend ring cracks typically form at a radial distance from the load axis and are is larger than that of Hertzian ring cracks [21]. This distance approaches the contact circle with diminishing coating thickness until bend ring cracks no longer occur [25]. Indeed, coating thickness highly controls what damage modes occur in a coating. Hertzian crack dominants the coating damage for thick and thin coatings, whereas bottom radial cracks are predominant for intermediate coating thickness [25]. The critical thickness at which one crack system dominates depends on the coating and substrate properties.

Other less common damage modes may occur in coatings. Delamination at the coating/ substrate interface may occur when the coating exhibits weak boding to the substrate or when a higher loads are applied [24], [25]. Delamination generally occurs because of compressive residual stress developed by the substrate during the unloading cycle as the substrate elastic recovery occurs [14], [26]. In addition, radial cracks may develop on the

coating surface parallel to the loading axis when applying a higher load. They may form at the edge of the impression left by the indenter and are caused by the hoop stress [9], [27].

2.3.2.2 Stress Distribution

Location of crack initiation is consistent with stress distribution. Therefore, analysis of stress distribution is of central importance because it can help locating stress concentration at which cracking may occur. Having a bilayer structure may vary the stress distribution of Hertzian contact from that of monolithic. As mentioned earlier, varying the coating thickness can also change the damage mode because of stress distribution within the coating has changed [10], [15]. Furthermore, under relatively high contact load, elastic-plastic behavior prevails. Fischer et al [26] indicates that substrate plasticity plays a significant role in stress distribution induced by indentation loading. In such situations, the stress distribution is a combination of both Hertzian elastic contact and residual stresses produced as a result of subsurface plastic zone formation. The elastic-plastic contact can be treated using the expanding cavity model [28]. In this model, the indenter is assumed to contact a hemispherical core having a radius equal to that of circular contact a, as shown in Figure 2-7. The core is surrounded by an incompressible plastic zone of radius r_c, which surrounded by an elastic zone. As the load increases, the indenter's penetration increases, thereby increasing the core diameter by da. This increase leads to an increase in the radius of the plastic zone by dr_c [29]. Substrate plastic deformation leads to induce bend stresses to the coating that may initiate ring cracks on the coating surface and/or radial cracks at the coating bottom surface [24], [30].

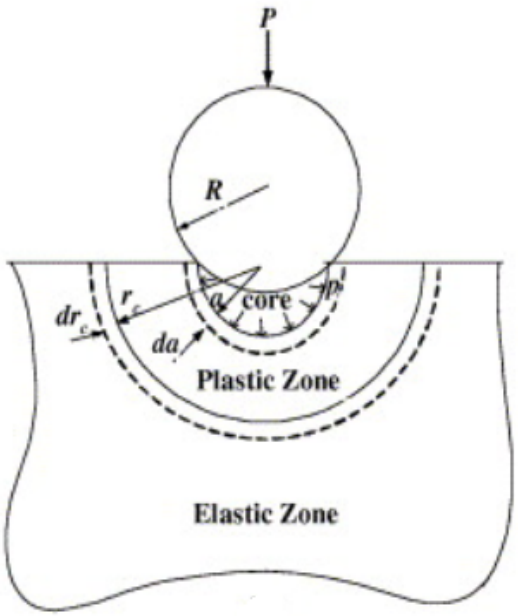

Figure 2-7 **Schematic diagram of elastic and plastic zones under spherical indentation [29].**

Coating can be assumed to be a flexural plate fixed at the edges far from the contact area and supported weakly by a soft material underneath [26]. In fact, when the ring crack forms far from the elastic contact region, the stress distribution is analogues to flexing a plate of fixed edge, as shown in Figure 2-8 [24], where the black region indicates the location of the maximum stress. Previous studies have proven that there is gradient stress in the contact zone that switches from tension to compression through the thickness. Location of maximum concentration stress is consistent with the location of fracture initiation [26]. For intermediate coating thickness, maximum tensile stress moves from the coating surface outside the contact area (as in thin and thick coatings) to coating lower surface below intender where radial crack may initiate. These changes in cracking pattern are evident of enhanced stress by the coating flexure supported by the soft substrate [21].

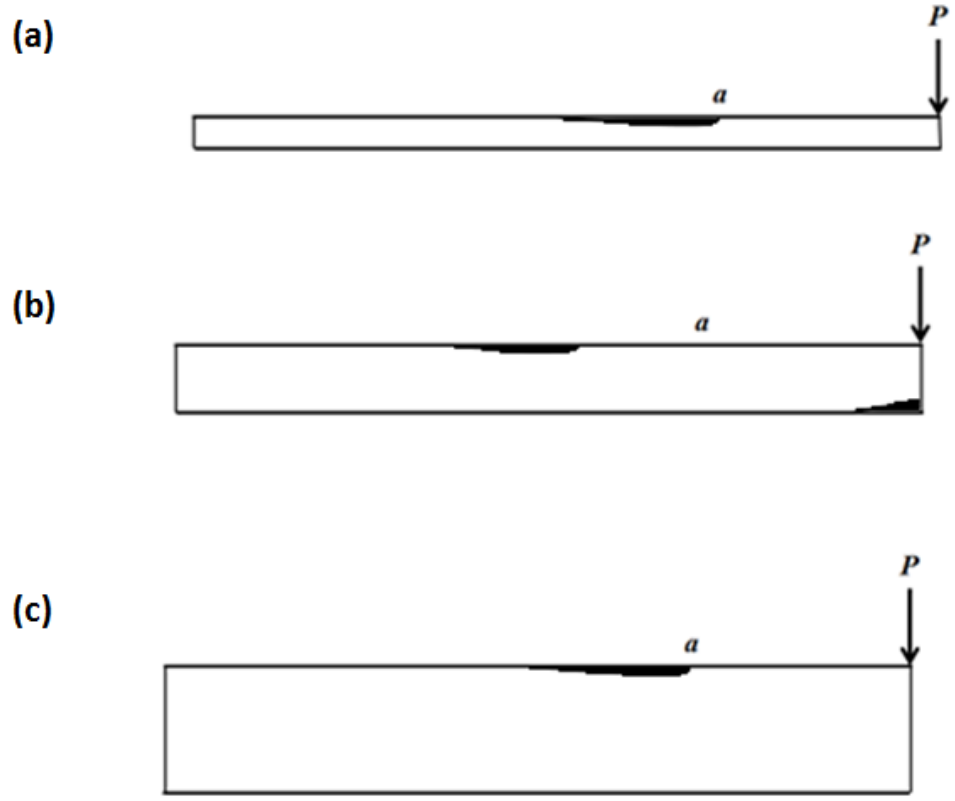

Figure 2-8 **Schematic diagrams showing the stress concentration (black region) of (a) thin (b) intermediate and (c) thick coating thickness under spherical indentation.**

2.3.2.3 Young's Modulus Mismatch

The ratio of Young's modulus of coating to that of substrate is important in terms of coating damage. Coating fracture can be inhibited by the soft substrate deformation when the mismatch is small. However, if the mismatch is large, it can promote the fracture due to bending because the coating and substrate will elastically deform at different rates. Single or multiple cone cracks may develop, as shown in Figure 2-9. If the substrate to coating Young's modulus ratio is 1:1, a straight cone similar to those formed in monoliths is generated [13], [27], [31]. Cone crack trajectories are changed from straight

line because of the mismatch in Young's modulus between substrate and the coating. In addition, cone crack deflects as it extends downward until it becomes almost parallel to the interface. Mismatch of the coating/substrate Young's modulus plays an important role in the impact of substrate elastic recovery on the coating cracking [14], [26]. As a result, high mismatch can also promote delamination [32].

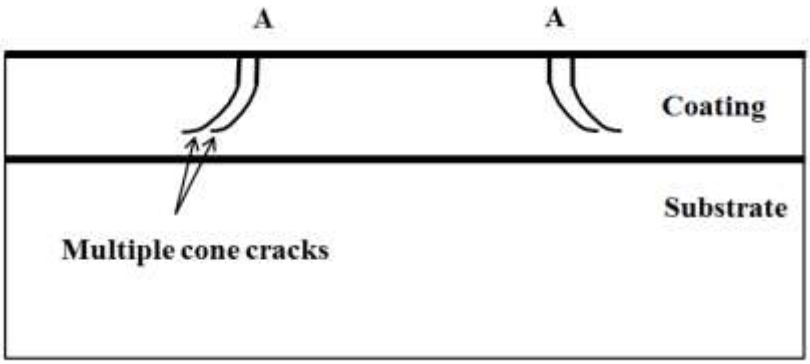

Figure 2-9 **Schematic showing multiple cone crack morphologies generated on the coating due to mismatch between the Young's modulus of the coating and that of the substrate.**

2.3.2.4 Critical load

Coating crack formation can be explained in terms of critical load at which cracks initiate. It was found that cracking event occurs on a certain coating when the applied load reaches a critical value. In fact, ring cracks have an indentation critical load different from that of radial cracks. The failure mode with the lower critical load will generate and may impede the other crack types from initiation. It has been well identified that the critical load of ring cracking is lower for thin and thick coatings on compliant substrates and, therefore, they are dominant in these regions. On the other hand, radial cracking has a lower critical indentation load than that of ring cracks for intermediate coating

thicknesses. As the coating thickness increases, the critical load of radial cracking increases until it becomes higher than that of ring cracking and, as a result, ring cracks dominant again. At a very thick coating when the substrate effect is eliminated, the brittle coating starts acting like monoliths and only Hertzian cone cracks can present. To conclude, the coating should be thick enough so that the critical load increases beyond the operational load of the intended application. However, it should not be too thick so that it may act similar to monoliths and substrate will not accommodate any of the contact loading [21], [24], [25], [33].

2.4 Thermal Damage

Thermal expansion is the tendency of a material to alter in size or shape when its temperature changes. Materials can expand when heated and contract when cooled because a rise in temperature increases the kinetic energy of molecules, thus increasing their movement and average separation [34]. The thermal expansion coefficient of a material indicates the rate of expansion due to an increase in temperature unit. The most commonly used unit for thermal expansion coefficient is μstrain/°C. When a heated component is constrained, thermal stress are induced in the component. At relatively higher temperatures, thermal stress may crack or plastically deform a constrained component depending on the material being used [35].

Thermal cycling (heating up then cooling down) can introduce or release residual stresses in steels depending on the cooling rate and maximum temperature. Slow cooling (furnace cooling) is capable of releasing residual stress. However, quenching (rapid cooling) can introduce significant differences in cooling rates (none-uniform cooling rate) within the

steel itself. The outer layer of material cools down at higher rate than the internal one. Therefore, the outer material contracts before the inner material. This puts the internal material in tensile stress and the outer material in compression [36].

Thermal expansion coefficient mismatch between a coating and a substrate complicates the process of thermal damage. Typically, the coating expands at a rate different from that of the substrate. This variance in expansion rates induces tensile stress to the material of lower thermal expansion coefficient and compressive stress in the material of higher thermal expansion [36], [37]. For example, if the substrate has higher coefficient than the coating, the coating will experience tensile stress and the substrate will encounter compressive stress. The larger the difference, the higher the tensile stress that can be induced. Depending on the material, fracture or plastic deformation may occur if the stress exceeds the material's ultimate strength or yield strength, respectively [37], [38]. At high enough temperatures, the mechanical properties of the system may be adversely affected.

Chapter 3

Substrate Characterization and Experimental Procedures

Characterization of the substrate, specimen's preparation, operating conditions and detailed layout of the experimental approaches utilized in this thesis are presented in this chapter.

3.1 Substrate Material

The substrate material was annealed 416 stainless steel bars (191 x 25.4 x 10 mm). The chemical and mechanical properties of the steel are given in Table 3-1 (a) and (b), respectively. The former was obtained by inductively coupled plasma (ICP) test, whereas the latter was acquired using a Bruker Universal Micro-Tribometer nano-indentation system. Scanning electron microscopy (SEM) analysis of the steel reveals the microstructure of 416 stainless steel which consists of a ferritic structure (most predominate phase) with chromium carbides at grain boundaries and manganese sulfide, as shown in Figure 3-1. X-ray diffraction (XRD) experiments were conducted utilizing a high-speed Bruker D8 Advance system that uses Cu-Kα radiation. Wavelength (λ), tube voltage and tube current were 0.154 nm, 40 kV and 40 mA, respectively. Figure 3-2

shows XRD pattern peaks that were identified to be those for steel found in the Powder Diffraction Files (PDF).

Table 3-1 Chemical and mechanical properties of 416 stainless steel

a) Chemical Composition (weight %)										
Fe	**C**	**Co**	**Cr**	**Cu**	**Mn**	**Mo**	**Ni**	**P**	**S**	**Si**
84.86	0.109	0.028	12.421	0.182	1.098	0.08	0.538	0.029	0.281	0.375

b) Mechanical Properties	
Young Modulus (GPa)	179 ±4
Hardness (GPa)	2 ±0.1
Vickers hardness (GPa)	1.6 ±0.1

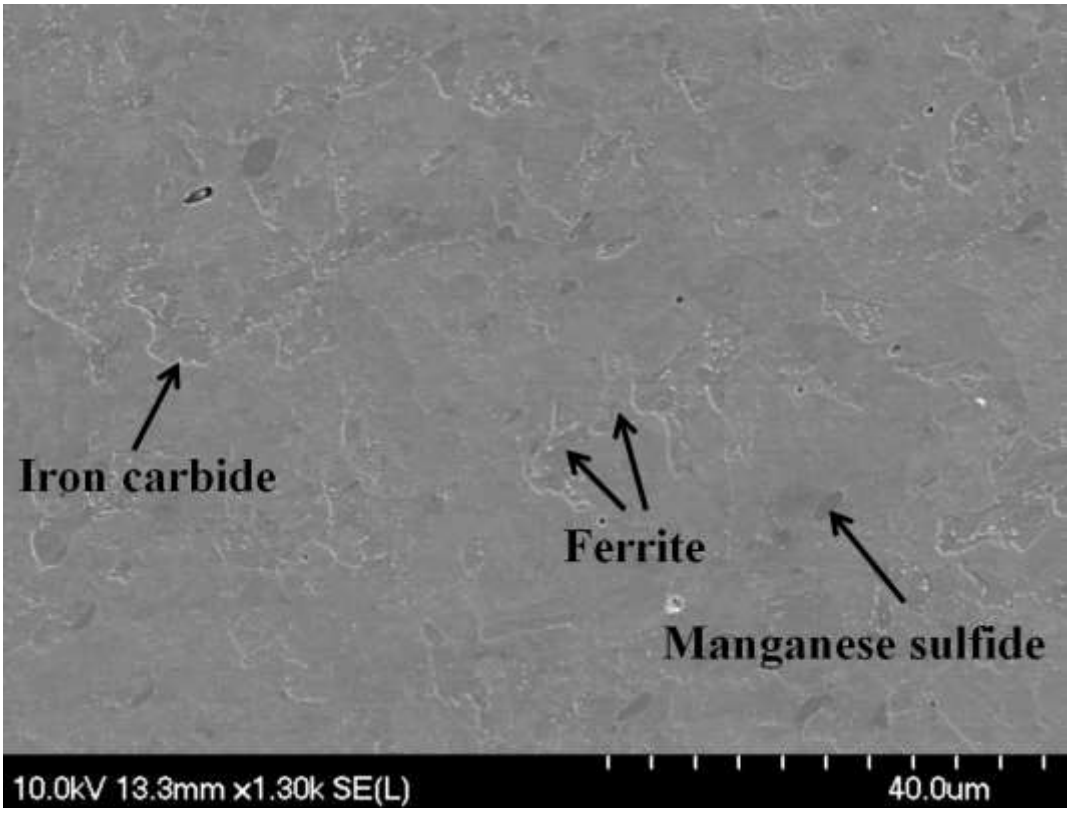

Figure 3-1 SEM micrograph of 416 stainless steel showing ferritic structure with carbides at grain boundaries

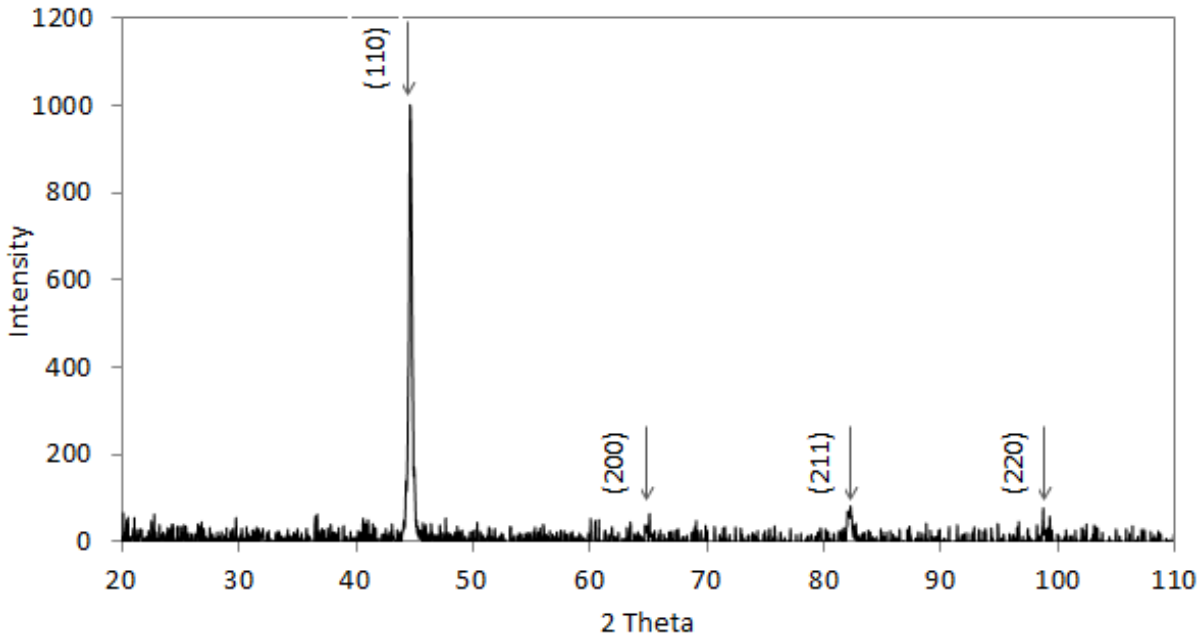

Figure 3-2 XRD Peaks of 416 stainless steel.

The Energy Dispersive X-ray Spectroscopy (EDS) technique was used to analyze the chemical composition of different phases in the microstructure of the substrate to verify those phases. In Figure 3-3, phases in the substrate are labeled with numbers and the chemical composition of each phase is given in Table 3-2 with the corresponding number. EDS analysis reveals that point 1 is manganese sulfide. Points 2 and 3 are iron carbide. Chromium carbide is precipitating on the grains in point 4.

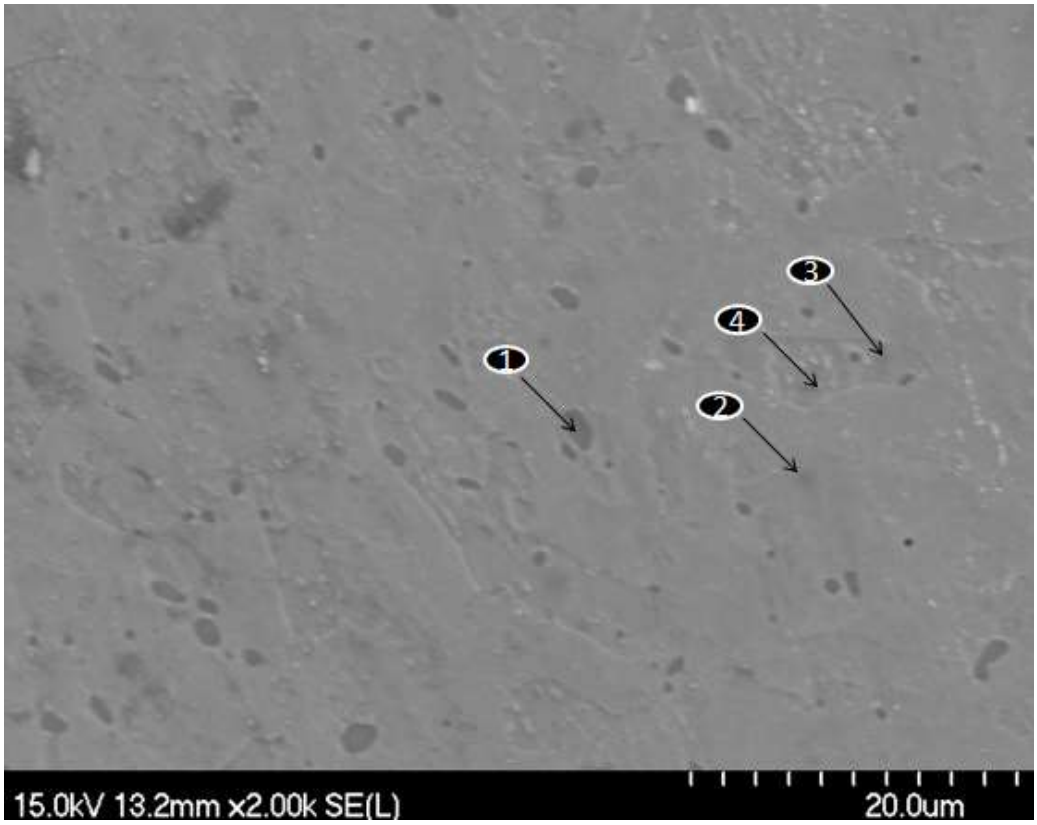

Figure 3-3 **Labeled phases in base metal to be analyzed using EDS.**

Table 3-2 **Chemical composition of different phases in substrate analyzed by EDS.**

Spectrum	C	Si	S	Cr	Mn	Fe	Cu	Total	Structure type
1	4.23		27.4	2.12	49.01	16.23	1.02	100	Manganese sulfide
2	3.97	0.42		11.68	0.61	83.04	0.27	100	Iron carbide
3	3.45	0.40		11.13	0.56	84.24	0.22	100	Iron carbide
4	5.75	0.22		23.07	0.44	70.45	0.07	100	Chromium carbide

3.2 Process Parameters for Chromium Electroplating

Steel samples were electroplated commercially using standard bath parameters which are given in Table 3-3. Different plating times (2, 10, 12, 14, 16, 20, 25 hrs) were used to produce coatings having different thicknesses. Plating thickness can also be changed by changing the current density of the process, but according to Guffie [2], current density plays a significant role in the mechanical properties of hard chromium coatings. Therefore, in order to investigate the effect of the plating thickness on the coating behavior, plating time was altered. Figure 3-4 shows a representative example of chromium electroplated stainless steel bar.

Table 3-3 Chromium electroplating process parameters

Bath Temperature (F)	120-130
Chromic Acid/ Catalyst Ratio	100:1
Chromic acid Concentration (g/L)	250
Sulfate concentration (g/L)	2.5
Current density (A/dm2)	31
Voltage (V)	8

Figure 3-4 Chromium electroplated stainless steel bar.

Chromium plated surfaces were ground using 240, 320, 400, and 600 grit SiC abrasive papers. When moving from one grit size to another, specimens were rotated 90 degree for efficient material removal. To obtain a fine surface finish, polishing was carried out using 1, 0.3 and 0.05 μm gamma alumina suspensions. An Olympus BX51 optical microscope and a Hitachi S-4700 scanning electron microscope were employed for examination of the specimens. Image-Pro® Plus software was used to analyze optical microscopy images and measure plating thickness.

3.3 Heat Procedure

Specimens with the plating time (16 h) were heated in a furnace for 5 minutes and then cooled either by water-quenching or by air cooling. Four different temperatures (200, 600, 800, and 1000° C) were employed.

3.4 Mechanical Properties Measurements

The mechanical properties of hard chromium coatings and the substrate material were obtained by means of a nano-indentation system employing a Berkovich diamond indenter, as shown in Figure 3- 5. Nine indentations were performed at various locations on the same sample using loads ranging between 10 and 400 mN to avoid any effects that may be introduced by irregularities on the surface. Instantaneous loads and depths were recorded and load vs depth profiles were plotted. Figure 3-6 shows a load/depth profile obtained from the nano-indentation system, where each line represents a complete indentation cycle. From load/depth profiles, hardness (H) and Young's modulus (E) were calculated using the Oliver and Pharr method [39]. Hardness is given by,

$$H = \frac{P}{24.5\ {h_c}^2} \qquad \text{Equation 3- 1}$$

where P is the load and h_c is the contact depth of penetration that can be calculated according to,

$$h_l = h_c + \left[\frac{2(\pi-2)}{\pi}\right]\frac{P_{max}}{dP/dh} \qquad \text{Equation 3- 2}$$

and h_l is the total penetration depth, dP/dh is the unloading-curve slop and P_{max} is the maximum load. Young's modulus can be calculated using

$$\frac{1}{E^*} = \frac{(1-v^2)}{E} + \frac{(1-{v_i}^2)}{E_i} \qquad \text{Equation 3- 3}$$

where,

$$E^* = \frac{dP}{dh}\frac{1}{2}\frac{\sqrt{\pi}}{\sqrt{A}} \qquad \text{Equation 3- 4}$$

and E^* is system's Young's modulus. E and v are Young's modulus and Poisson's ratio of the specimen, respectively. Similarly, Poisson's ratio and Young's modulus of the indenter were E_i and v_i.

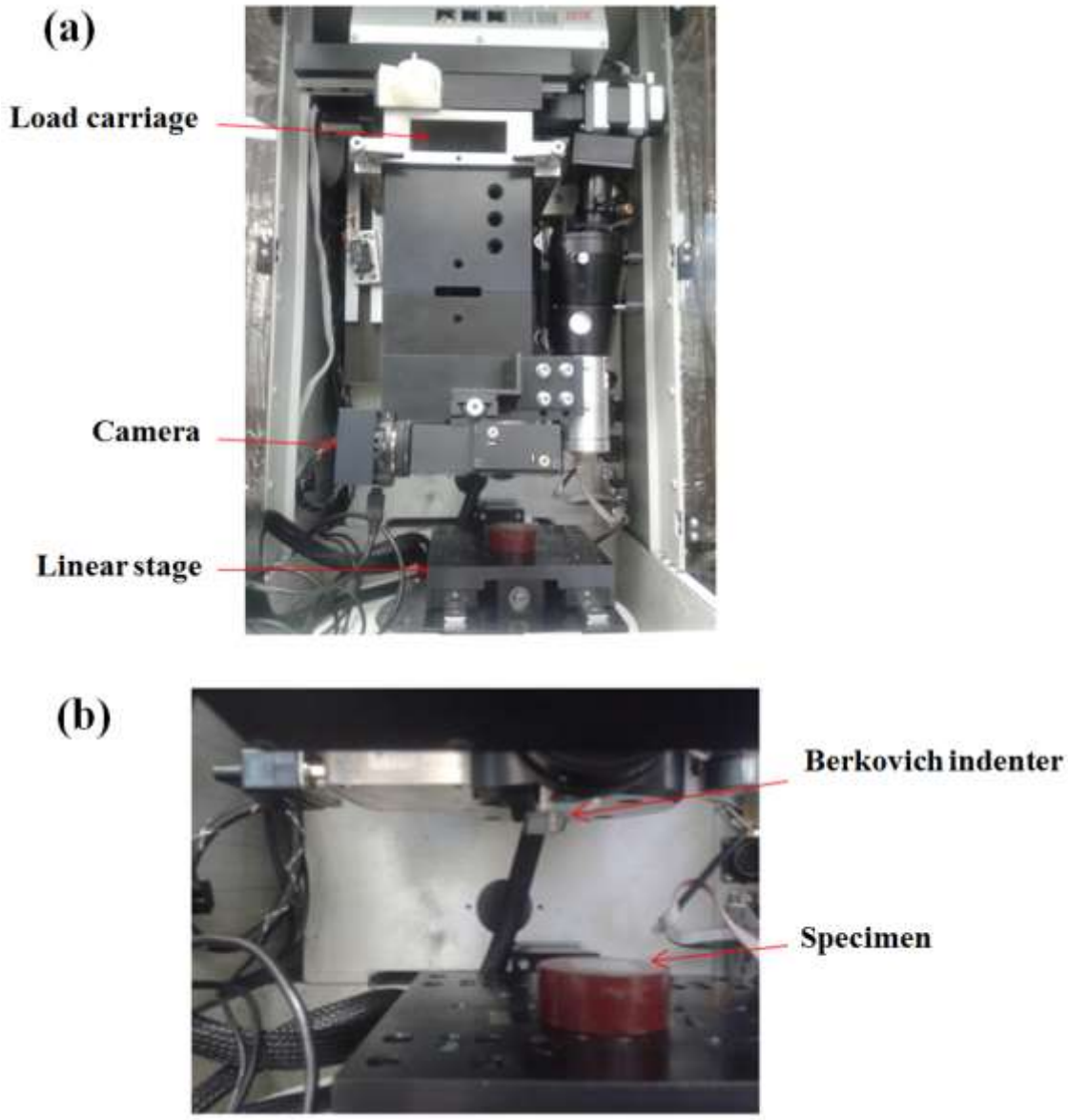

Figure 3- 5 **a) Nano-indentation setup (b) a close up image of the system showing the indenter and a test specimen.**

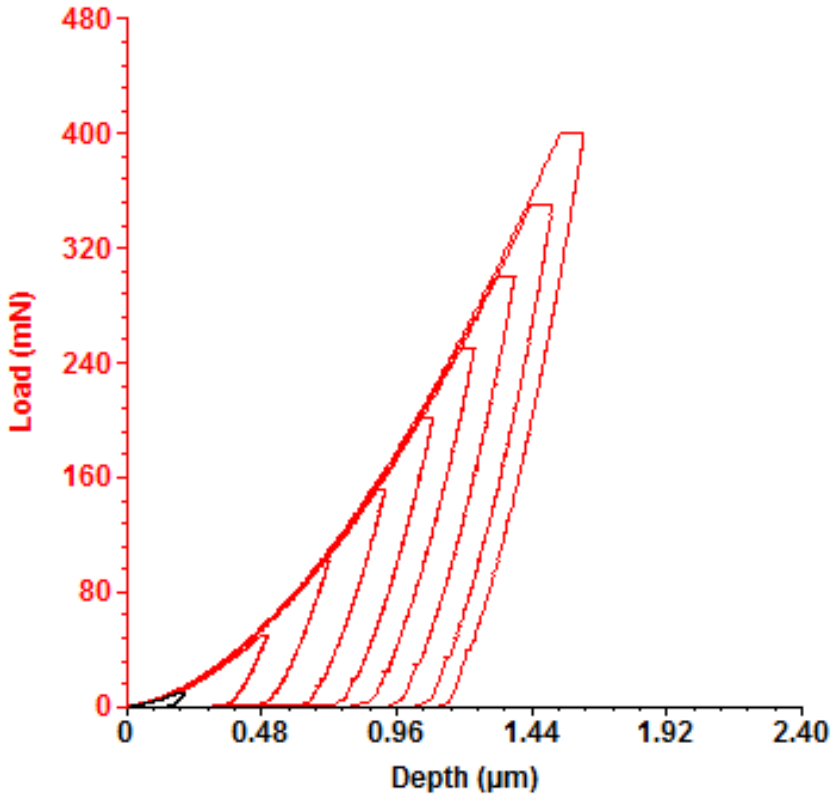

Figure 3-6 **A load/depth profile for hard chromium coating obtained from the nano-indentation.**

3.4.1 Vickers Hardness and Fracture Toughness

A Vickers tester was used to carry out Vickers hardness (HV) measurement of the coatings. A one kg load was applied to the coating surfaces. Each sample was tested three times to ensure repeatability and the HV was computed according to the following equation [40]:

$$HV = 1.8544 \times {}^{P}/_{d^2} \qquad \text{Equation 3- 5}$$

where, P is the applied load (kgf), and d is mean diagonal length of the indentation. Figure 3-7 shows a typical impression of Vickers indentation. The hardness of the coating

and substrate of the heated specimens was also measured after cooling as a function of heating temperature.

Impressions of the Vickers indenter were used to calculate the fracture toughness (K_I) of the chromium coatings using the following equation [41]:

$$K_I = 0.015 \left(\frac{a}{l}\right)^{1/2} \left(\frac{E}{H}\right)^{2/3} \frac{P}{c^{3/2}} \qquad \text{Equation 3- 6}$$

where l is crack length generated from the impression corners; a is half of diagonal length of the indentation; $c = a + l$ (see Figure 3-7).

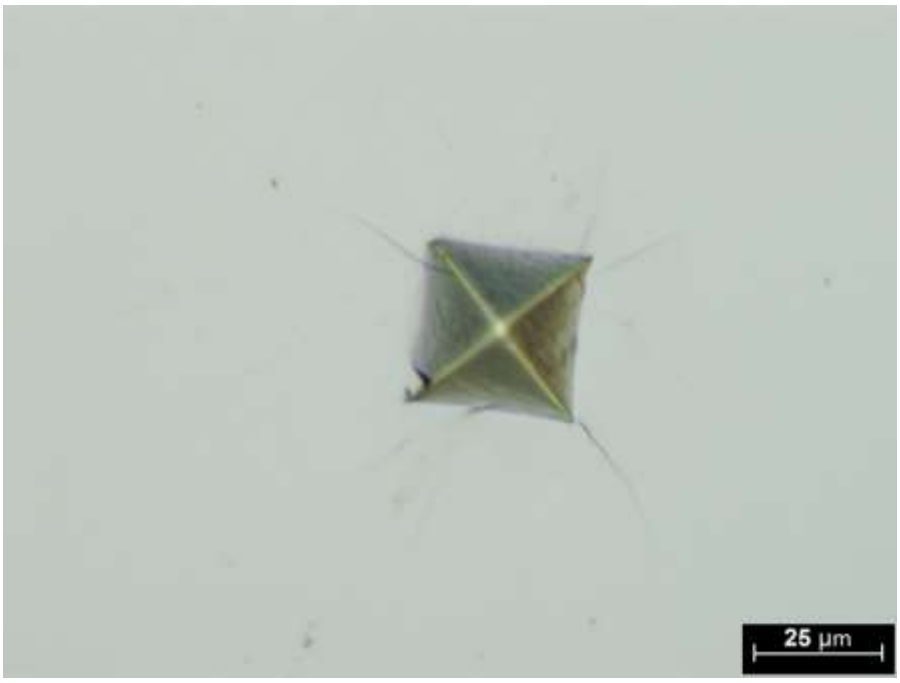

Figure 3-7 **Optical micrograph showing typical Vickers indenter impression on hard chrome coating using 1 kg load**

3.5 Residual Stress Measurement

An X-Ray diffraction technique was used to obtain residual stress in chromium coatings induced during the electroplating process [42]. A sample having a chromium coating thickness of 167 μm (labeled E) was scanned in different directions, 0°, 45°, and 90° from the perpendicular axis to the coating surface, as shown in Figure 3-8. Scanning was carried out at different depths 0, 50, 120, and 171 μm. The deepest scan was on the coating/substrate interface. An electropolishing process was employed for chromium layers removal. A second sample having a coating thickness of 40 μm (labeled B) was scanned in similar directions, but only a surface scan was conducted. XRD experiments were also conducted on specimens heated up to 600 and 1000° C (both quench and air cooled) in the same three directions.

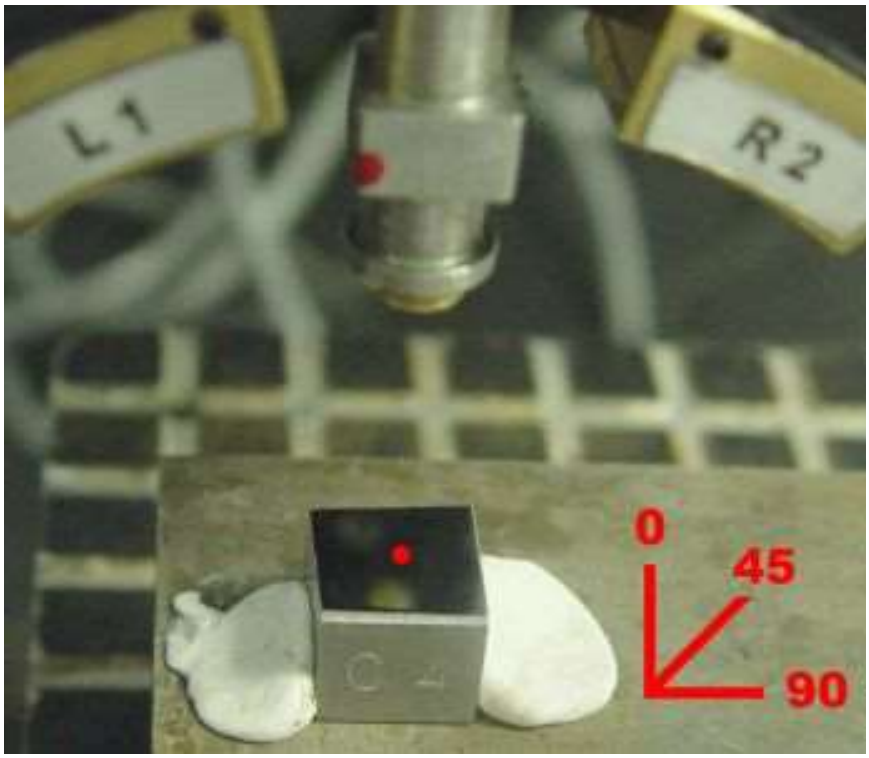

Figure 3-8 XRD experimental setup.

3.6 Crack Density Measurements

Inherent crack densities in the coating were determined on polished specimens. Image analysis of optical micrographs of the surface coating was performed using a technique developed by Nascimento and Voorwald [43]. Three random sites on a polished surface were captured using an optical microscope. Horizontal lines were superimposed on the images and intersection points between the inherent cracks and these lines were counted. Inherent crack densities were then computed by dividing the number of intersection points by the length of the horizontal lines. Figure 3-9 is an image of a coating showing the inherent cracks and horizontal lines. The same procedure was followed with all samples while keeping a constant magnification. Crack densities in the coating cross sections of heated specimens were also determined using the same procedure, as shown in Figure 3-10.

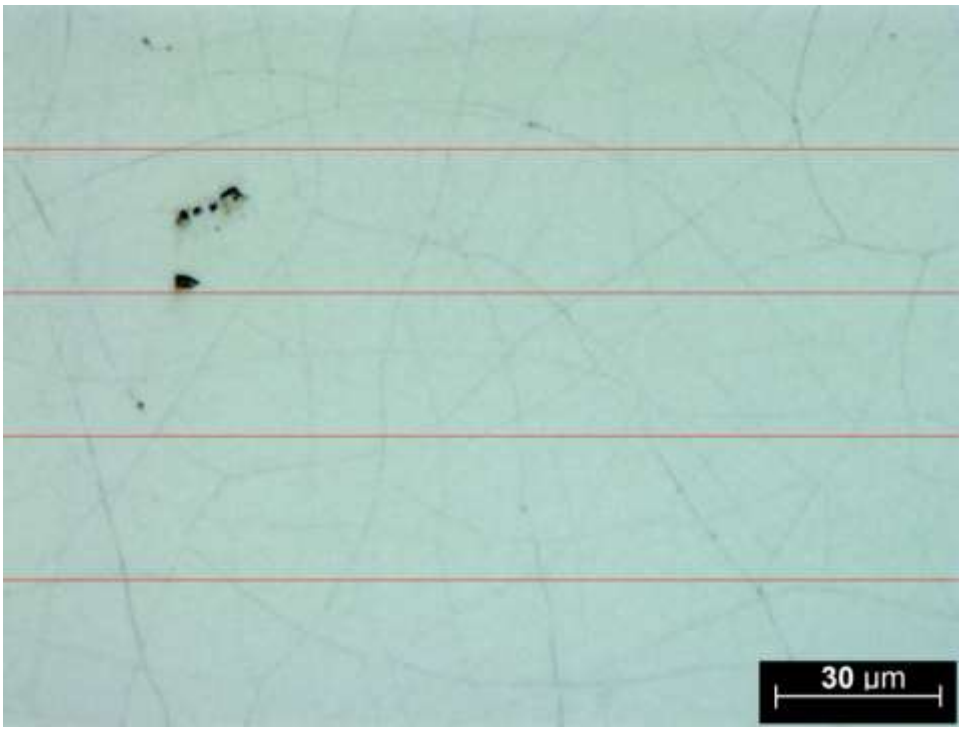

Figure 3-9 **Optical micrograph of a polished chromium coating surface showing horizontal lines superimposed on the image used to determine crack density.**

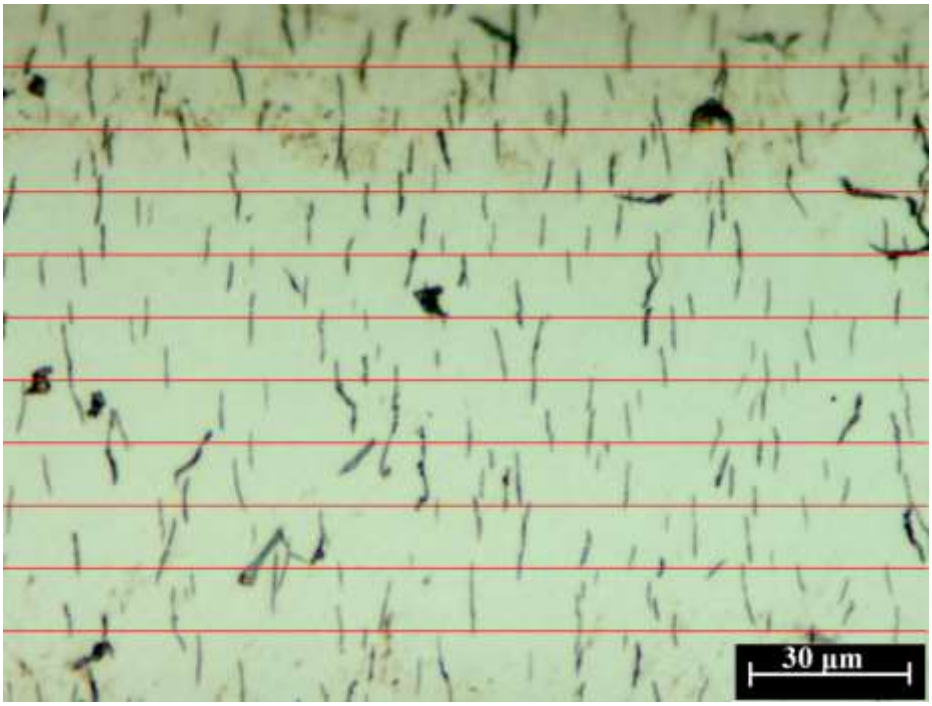

Figure 3-10 **A representative micrograph of a coating cross-section along with superimposed horizontal lines.**

3.7 Indentation Study

The mechanical response of hard chromium coatings on 416 stainless steel to Hertzian contact was also investigated. An indentation study was carried out using a Rockwell tester employing a spherical hardened steel indenter having a diameter of 1.59 mm. The indenter's Poisson's ratio and Young's modulus was 0.29 and 210 GPa, respectively. High contact loads were applied to ensure that contact damage in the form of coating fracture and substrate plastic deformation occurred. All thicknesses were indented with different loads (60, 100 and 150 kg) to assess the mechanical damage as a function of plating thickness and load. A single loading/unloading cycle in air was used for Hertzian contact test for a contact duration of 10 s. In order to investigate the effect of thermal damage on the mechanical response to the indentation load, a series of indentations were performed on heated specimens using only 100 kg load.

Specimens were then cross-sectioned to examine subsurface damage in the coatings and substrates. A Buehler isomet 1000 precision saw was used to cut the specimens using a diamond wafering blade (15.2 cm diameter and 0.5 cm thick). Cutting was carried out under a 100 g load and at rotational speed of 200 RPM to avoid any thermal or mechanical damage to the samples.

3.8 Strain Measurement

A novel method was used to investigate the permanent strain caused by the indentation tests on sample with a coating thickness of 167 μm and an applied load of 100 kg. In particular, a matrix of microscopic circles was drawn on two specimens using focused ion

beam (FIB). Circles of 65 μm diameter were milled on the coating surface of the first sample, as shown in Figure 3-11. A spherical indentation was performed on the matrix. Another specimen was cut into two halves; cut faces were polished and then circles were milled on one polished face, as shown in Figure 3-12. Two rows of circles of 32 μm diameter were placed on the coating and one row on the coating/substrate interface, as shown in Figure 3-13. Three rows of circles were placed on the steel substrate. By doing so, damage of both coating and substrate could be examined. After that, the two halves were held against each other using a holder. A small clamping force was used so that minimal additional stress was induced. Indentation was performed on the interface of the two blocks, as shown in Figure 3-14. The two blocks were separated for examination of circles to assess the sphere-indentation damage of the structure [32]. This method has not been used to investigate the indentation damage. In sheet metal, similar technique is used to investigate the formability of metals, but in the macroscale not in the microscale as the case in this study.

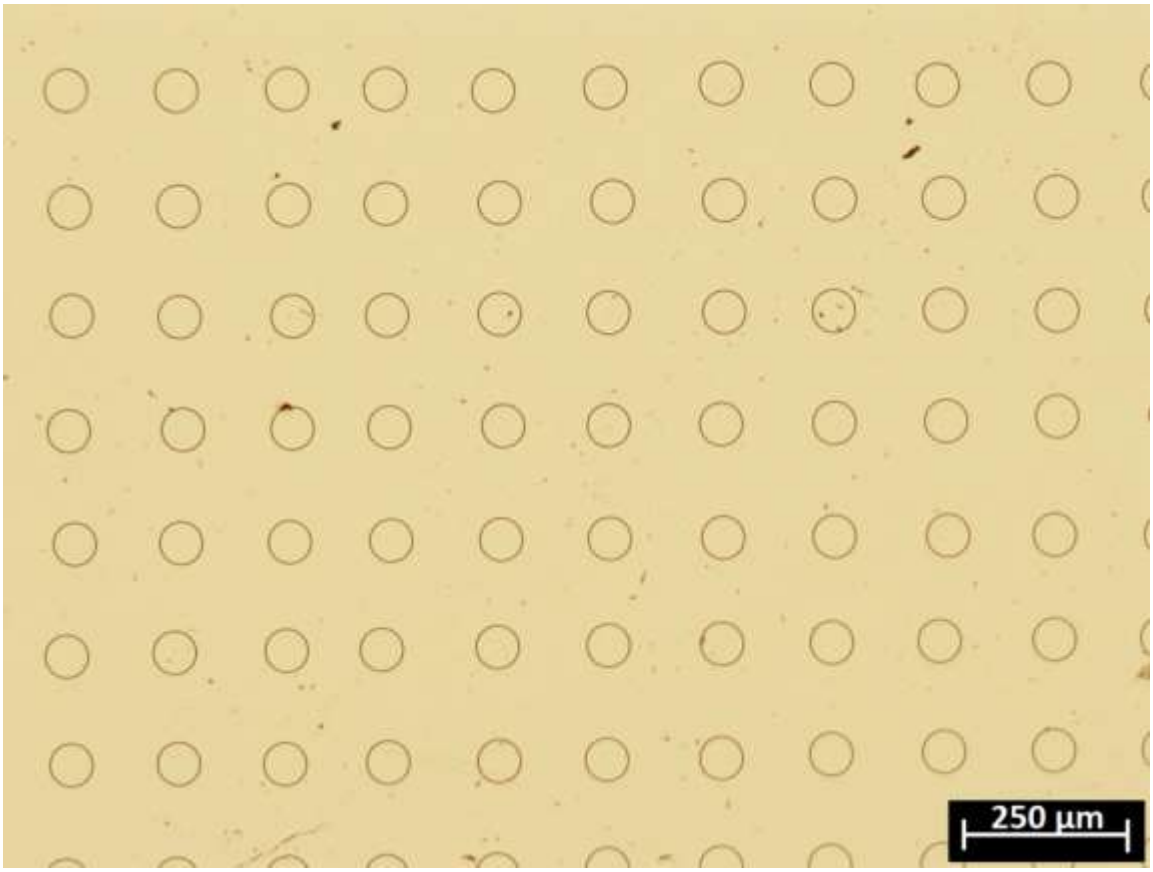

Figure 3-11 **An optical micrograph showing a matrix of circles on coating surface.**

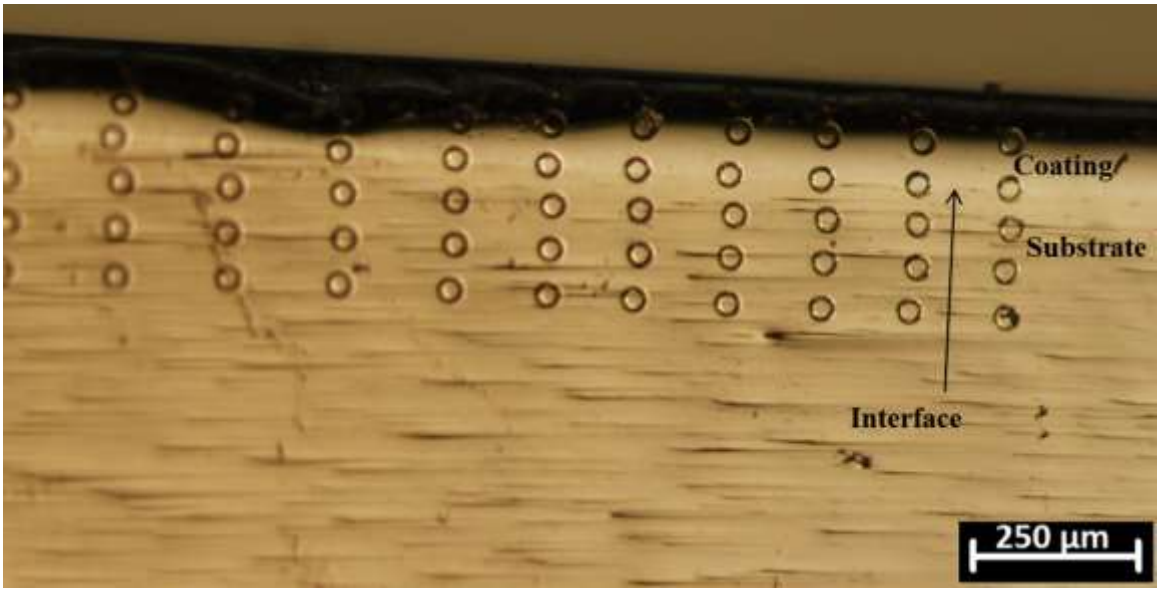

Figure 3-12 **Circle array on the coating cross-section before indentation.**

Figure 3-13 **Coating cross-section showing a circle on the coating/ substrate interface.**

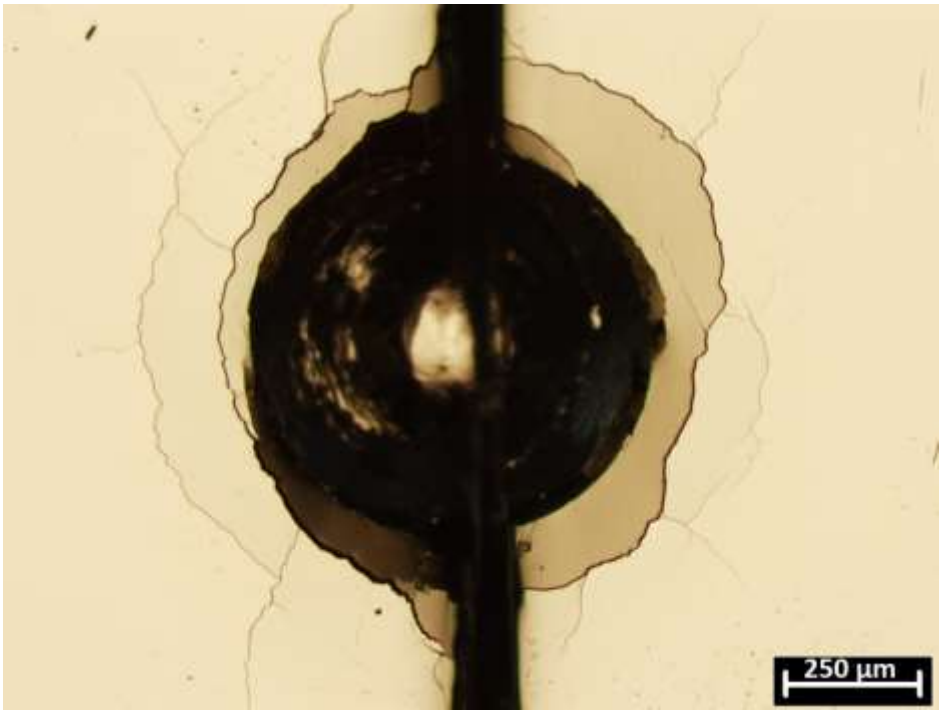

Figure 3-14 **Indentation impression on the trace of the interface of the two blocks.**

Plastic deformation due to indentation loading can distort the circles into ellipses. When an elliptical shape is produced, the longest diameter is called the major axis (major strain), while the shortest is named minor axis (minor strain), as shown in Figure 3-15. The former is caused by the maximum principal stress and the latter is caused by the minimum principal stress. If the length of one of the ellipse axis is larger than the initial diameter of the circle, then the deformation was caused by tensile stress. On the other hand, compressive stress is the cause of the deformation when the length of the ellipse axis is shorter than the original one. Principal strains were calculated by dividing the change in diameter over original diameter.

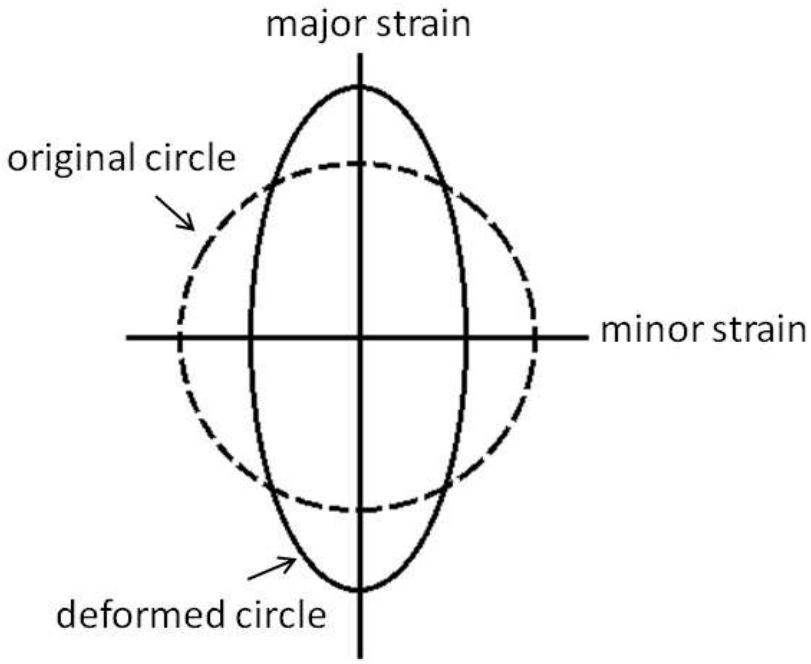

Figure 3-15 **Schematic diagram showing the effect of deformation on circle's dimension.**

Chapter 4

Results and Discussion

In this chapter, experimental results are presented and discussed. It is divided into 3 main sections. Mechanical damage as a function of coating thickness is discussed first. In the second section, thermal damage as a function of heating temperature as well as its effects on mechanical damage are investigated. Finally, an investigation of stresses and strains due to spherical indentation is presented.

4.1 Mechanical Damage

This section presents the general characterization of the coating first. Then, the investigation into the mechanical damage of coatings and factors affecting the damage mode is discussed.

4.1.1 Characterization of Chromium Coatings

An optical microscopy image of the as-deposited hard chromium coating along with substrate surface is shown in Figure 4-1. The image reveals an inherent crack network that developed during the electroplating process due to residual tensile stresses. Two types of cracks were identified. The first are dark cracks which were freshly formed cracks. The second are deeper in the coatings and appear brighter in the image. These

cracks formed first and then a layer of chromium partially covered them [8]. It was also observed that the coating surface topography replicates the substrate surface as shown in Figure 4-1 (insert). Paths of the cutting edge of the milling cutter that took place prior to plating are observed on the coating surface. This is because chromium electroplating does not show any kind of leveling. In other words, chromium deposition will not only reproduce substrate roughness, but also will magnify the peaks and valleys. Figure 4-2 shows the difference between leveling and none-leveling coating mechanisms. This feature is well documented in the literature of hard chromium electroplating [44].

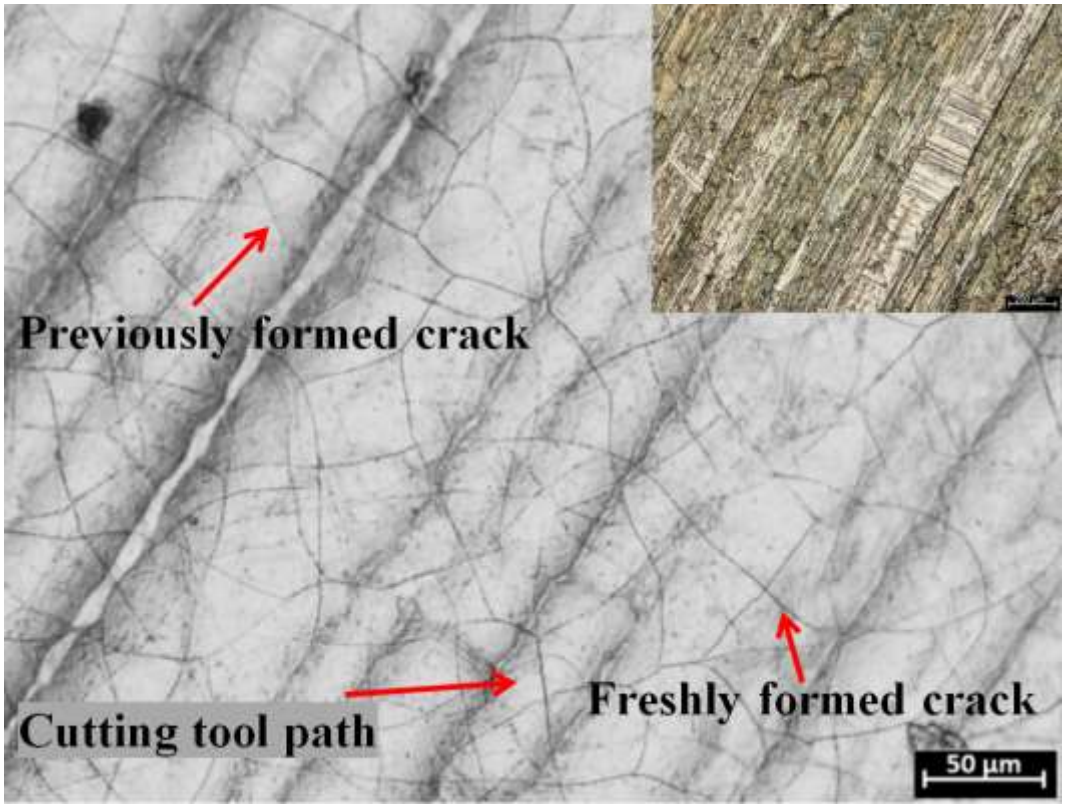

Figure 4-1 Micrograph of chromium plating surface along with substrate surface prior to plating (insert)

Figure 4-2 Schematic diagram showing leveling and no leveling mechanism.

Next, plated specimens were sectioned to examine the coatings cross sections, as shown in Figure 4-3. The coating appears uniform and dense with low porosity. The coating exhibits excellent bonding to the substrate as it shows a continuous interface with no defects. Inherent cracks, visible in the cross-section, are perpendicular to the substrate and are about 7 μm in length. They are randomly distributed along the cross-section and did not extend to, or into, the substrate, as shown in Figure 4-4.

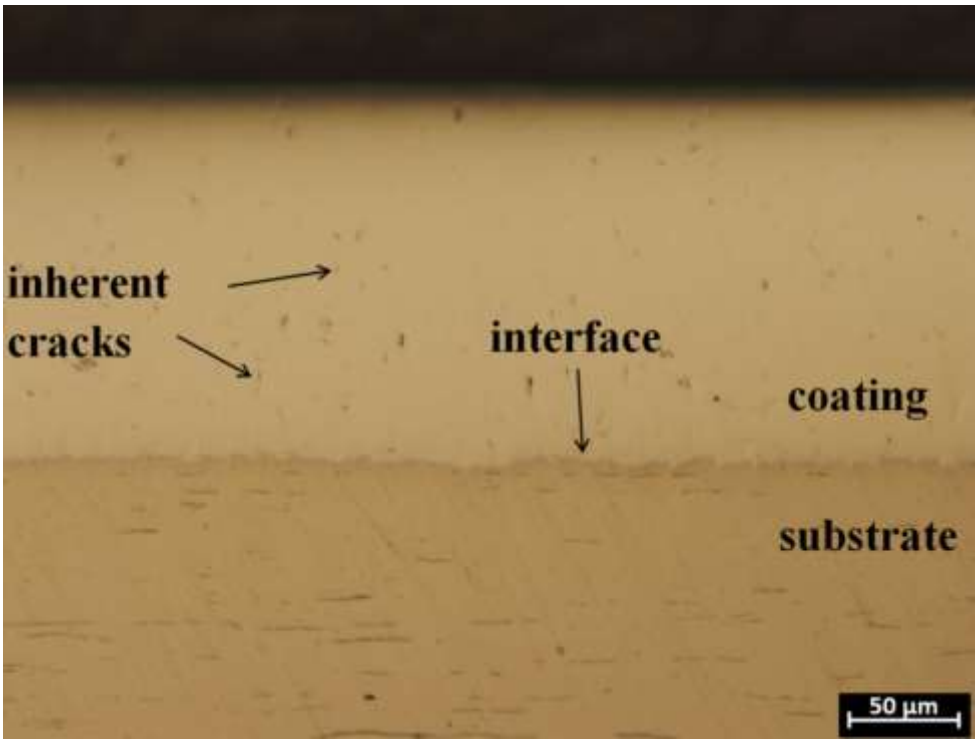

Figure 4-3 A representative cross-section of a chromium coating (plated for 16 h)

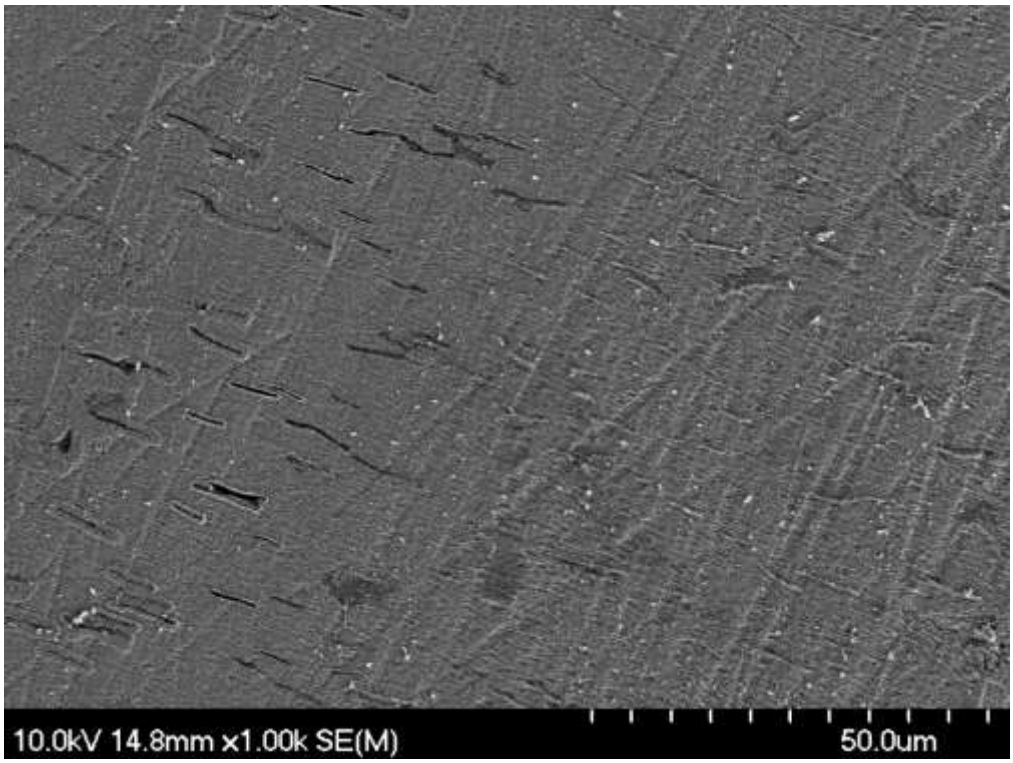

Figure 4-4 An SEM micrograph of chrome coating cross section showing the inherent cracks

Coating thickness as a function of plating time was measured using a distance measurement tool in the image analysis software. Table 4-1 shows the plating time and the corresponding coating thickness. It is observed that as the plating time increases, the plating thickness increases.

Table 4-1 Plating time and corresponding coating thickness

Sample	**A**	**B**	**C**	**D**	**E**	**F**	**G**
Plating time (hrs)	2	10	12	14	16	20	25
Coating thickness (μm)	11	40	87	100	167	184	194

The average surface roughness (Ra) of the substrate prior to plating was 0.68 ±0.08 μm. It is observed that plating thickness had no significant impact on surface roughness of the coating. The average Ra after plating for all thicknesses was 0.70 ±0.06 μm. It is interesting to note that the coating surface roughness is very similar to that of the substrate. This commonly occurs when using low current density during the plating process [2], [8] as the case in this study. Chromium plated parts are usually ground for surface finish and tolerance requirements. Rz is an important parameter in grinding because it works as an indicator for the minimum depth of cut required to obtain a flat surface, surface with no grooves. For studied samples, the depth of cut has to be more than 4 ±0.05 μm. Such finish is financially preferred because a little material required removal.

4.1.2 Mechanical Properties Results

Mechanical properties of chromium coatings were obtained using a nano-indentation system. Equation 3- 1 to Equation 3- 4 were used to calculate the hardness and Young's modulus of the samples, respectively. It was found that the plating thickness had no impact on either hardness or Young's modulus. The average hardness and Young's modulus of the coating obtained from nano-indentation testing was 9 ±1.5 and 290 ±67 GPa, respectively. Due to the small indentation depth (< 1.5 μm) of the nano- indentation test, any substrate effect was eliminated.

Vickers indentations were performed on coatings using 1 kg load. The average Vickers hardness was found to be 850± 25 kgf/mm² (8.5 GPa). Fracture toughness values were calculated from Vickers indenter impressions. Similar to hardness, coating thickness had

no significant impact on fracture toughness of the chromium coatings. The average fracture toughness is 6.1± 1.6 MPa*m1/2. All values of mechanical properties are in agreement with values found in the literature for nano-hardness [45], Young's modulus, fracture toughness [46] and Vickers hardness [5].

4.1.3 Residual Stress Results

Stress as a function of coating thickness profiles of sample 'E' measured at different direction were plotted, as shown in Figure 4-5. It was found that there is no significant difference between stress values measured at various directions. This indicates that residual stresses are isotopic in the plane of the coatings. Maximum and minimum principal stress versus coating thickness of sample 'E' were plotted, as shown in Figure 4-6. Both principal stresses were close in magnitude and exhibited a similar trend. At thickness zero (at coating/substrate interface), stresses were compressive due to interface mismatch. As the thickness increased the residual stresses rise and became tensile at a thickness greater than 13 μm. The tensile stresses continue rising to a value of 300 MPa at a thickness of about 120 μm. On the surface, the residual stress drop slightly. This drop could be because of the mechanical polishing done prior to XRD experiment, which tends to induce compressive stress.

Surface residual stress measurements were also performed on specimen 'B' having thickness of 40 μm. The maximum principal stress at the surface of this sample was +162 MPa. In order to compare the principal stresses of specimen 'E' and 'B' at the same coating thickness, a best fit line of the maximum stress in Figure 4-6 was generated. The maximum principal stress at thickness of 40 μm calculated using the best fit polynomial

was about +150 MPa which is close to result obtained for specimen 'B' at the same coating thickness. This indicates that as the chromium coating is building up, the residual stress increases and is purely a function of thickness and not affected by latter deposits of chromium.

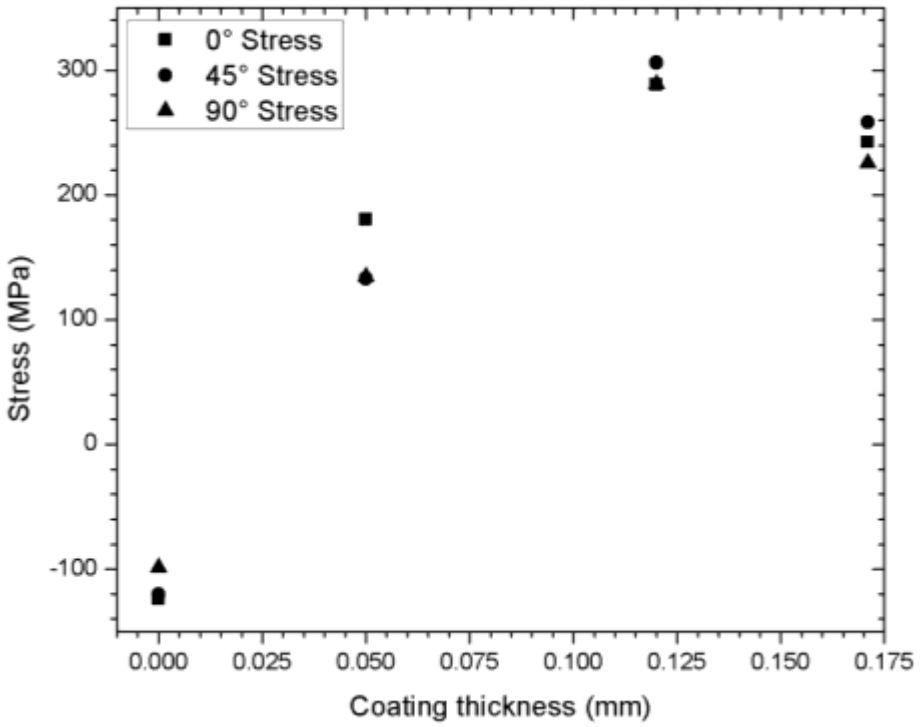

Figure 4-5 Stress in chromium coating measured at different scan angle as a function of coating thickness

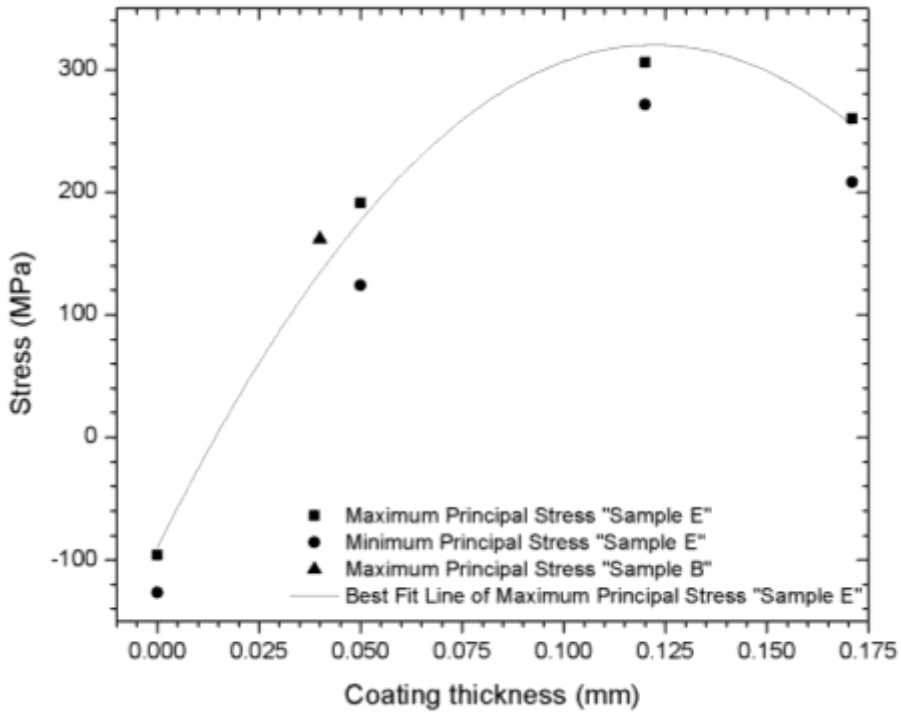

Figure 4-6 Maximum and minimum principal residual stresses in chromium coating as a function of thickness

4.1.4 Inherent Cracks Density on Coating Surface

Measurement of the inherent crack density on the surface of the chromium coatings was conducted on polished specimens. Inherent crack densities on the coatings surfaces with corresponding plating thickness are shown in Figure 4-7. It was observed that the surface inherent crack density increased with increasing thickness, which has also been observed by others [8]. The increase in crack density is caused by the rise in residual stresses as a result of increase in coating thickness previously noted. The overall average inherent crack density was 125 cracks/mm which is in agreement with other studies [47]. The question that now arises is whether cracking density and residual stresses would impact coating mechanical failure.

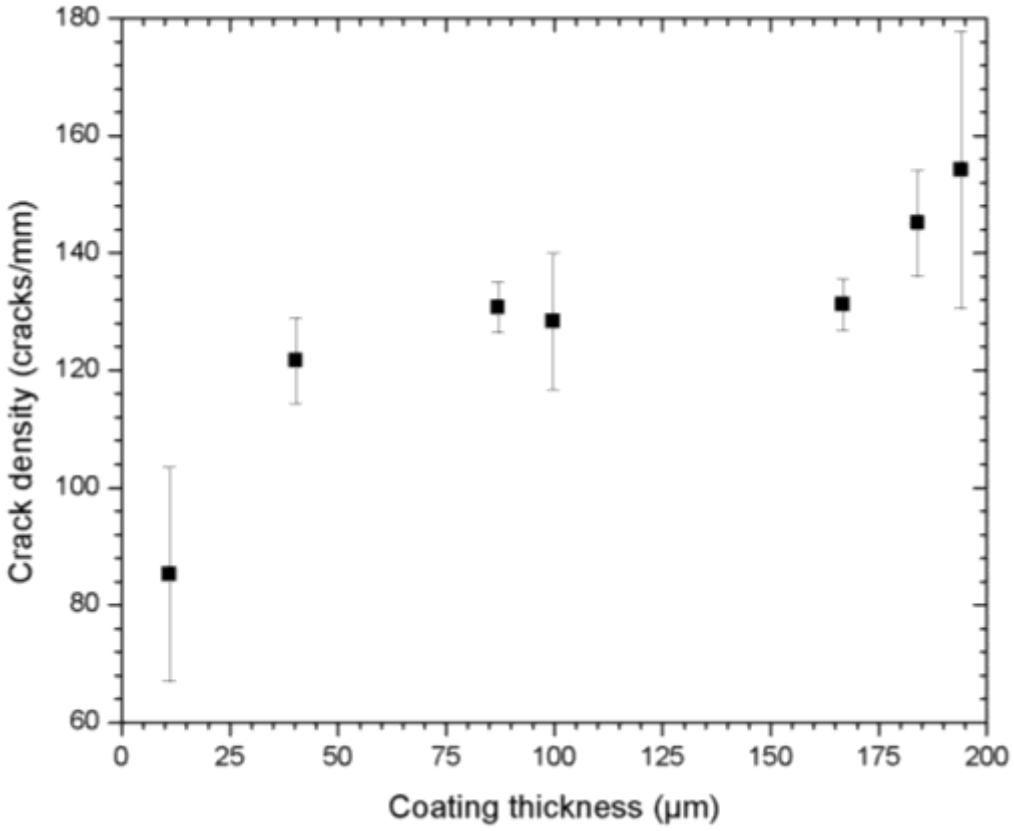

Figure 4-7 Inherent crack density observed on plating surfaces as a function of coating thickness

4.1.5 Indentation Results

In order to assess the coating behavior under indentation and its relationship to residual stresses and inherent cracks, a series of indentation experiments were conducted on the coatings. Indented coating surfaces and cross-sections were examined using optical microscopy to evaluate cracking damage resulting from the spherical indenter. Two types of surface cracks were identified: ring and radial cracks, as illustrated in Figure 4-8. Transverse cracks were observed on the cross-section, as shown in Figure 4-9. The diameter of ring cracks and the length of radial cracks increased with increasing load. Furthermore, size of indent impression increased with increasing load which indicates

more damage takes place with increasing load as expected. For all thicknesses, it was observed that pattern of cracking damage did not change with load. This indicates that change in load did not alter stress distribution (only stress magnitudes).

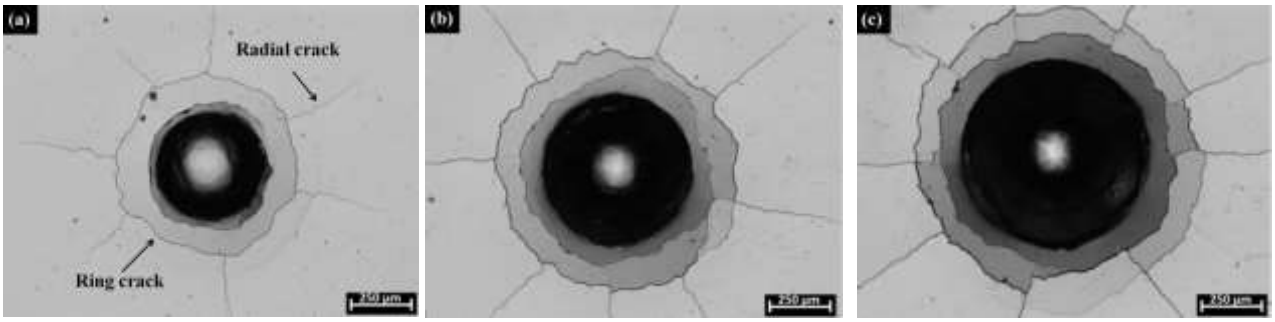

Figure 4-8 Optical micrographs showing cracking pattern of chromium coating (167 µm thick) indented with a sphere under a) 60, b) 100 and c) 150 kg load.

Figure 4-9 Optical micrographs showing cross-sections of cracking pattern of chromium coating (167 µm thick) indented with a sphere under a) 60, b) 100 and c) 150 kg load

Profilometry scans were carried out to assess geometric feature of the indentation impression. Figure 4-10 shows a representative example of a 3D representation of indents on a 167 thick coating as a function of load. As observed in optical microscopy images, increasing applied load remarkably enlarged indents impression. In particular, they become wider and deeper as the load increases. Hertzian and radial cracks are visible in the scans. This indicates that they are wide enough for the scan to recognize them. The

same trend was observed when looking at the indentation profiles, as shown in Figure 4-11. The depth of 60 and 150 kg indentation are 28 and 105 µm, respectively.

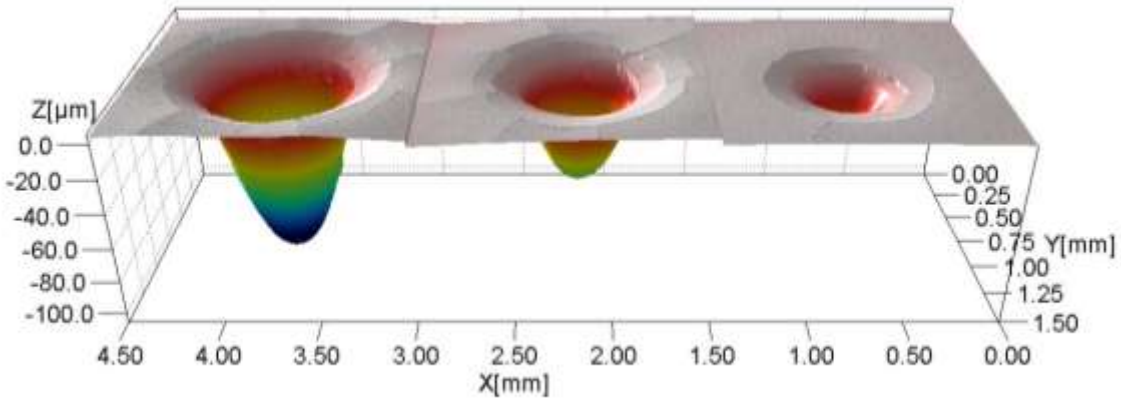

Figure 4-10 **3D representation of indents on hard chromium (167 µm thick) coating with loads of 60, 100, 150 kg, from right to left (aspect ratio 1:1:10)**

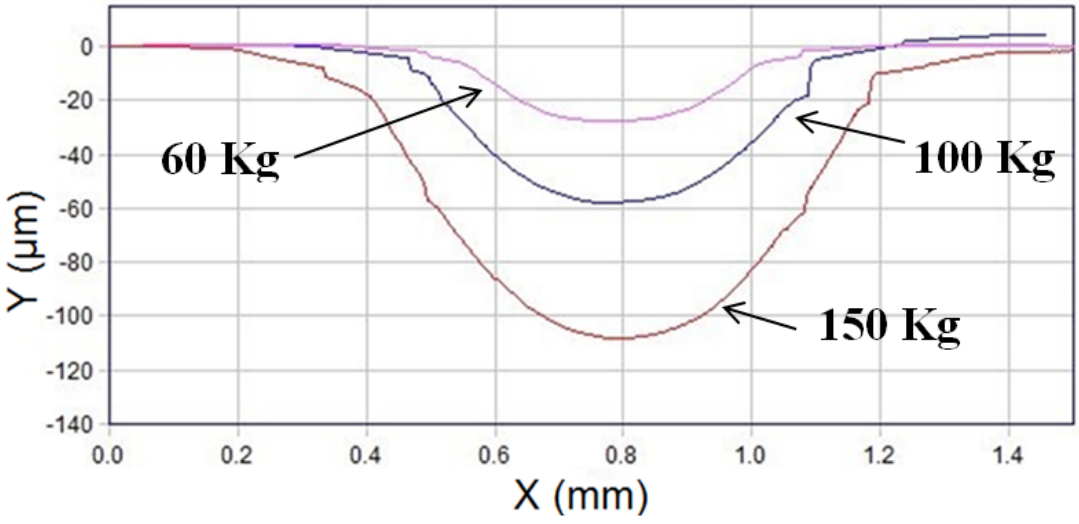

Figure 4-11 **2D representation of indents on hard chromium (167 µm thick) coating with loads of 60, 100, 150 kg, (aspect ratio 1:12)**

The damage cracks are those caused by the indentation loading. The relationship between cracking damage and coating thickness was also investigated. Gridlines were superimposed on optical microscopy images of indent impressions in order to measure density of cracks due to indentation, as shown in Figure 4-12. A similar procedure used to calculate inherent crack density was followed to determine crack density due to indentation. Figure 4-13 shows the cracking density as a function of coating thickness. Cracking density initially increased as the coating thickness increased. At intermediate coating thicknesses, cracking density reaches its highest value after which it declines. From this plot, one can identify three regions: thin, intermediate, and thick coatings. Each region has distinctive cracking pattern and shall be discussed below.

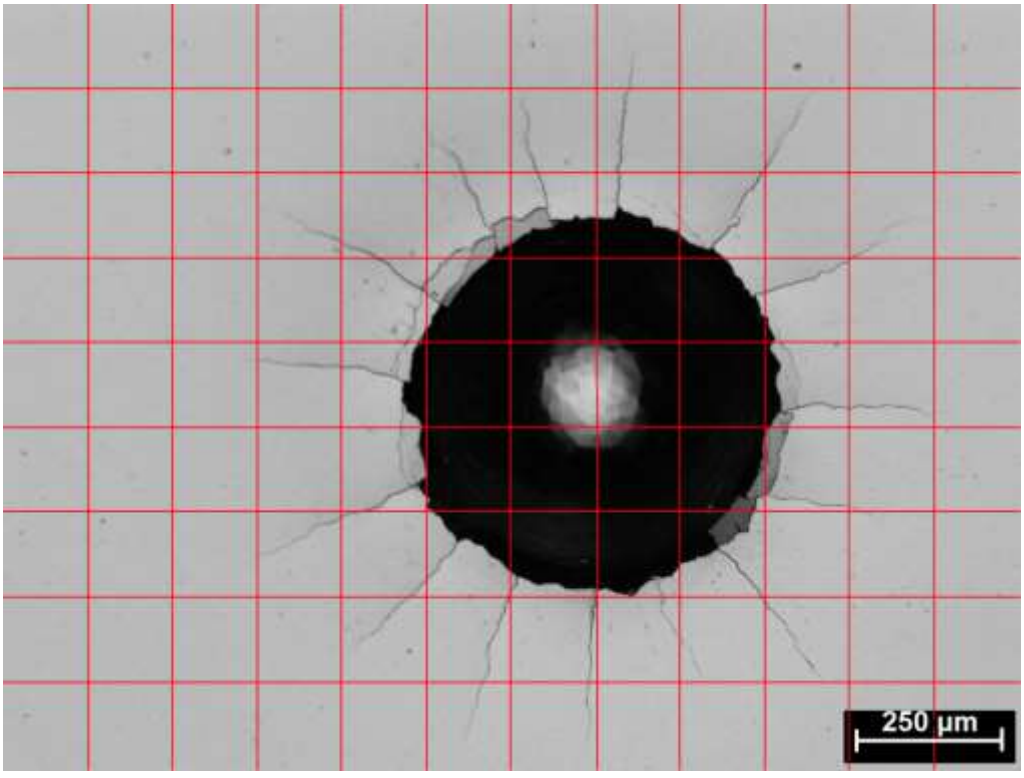

Figure 4-12 **A representative micrograph showing an indentation along with the superimposed grid lines.**

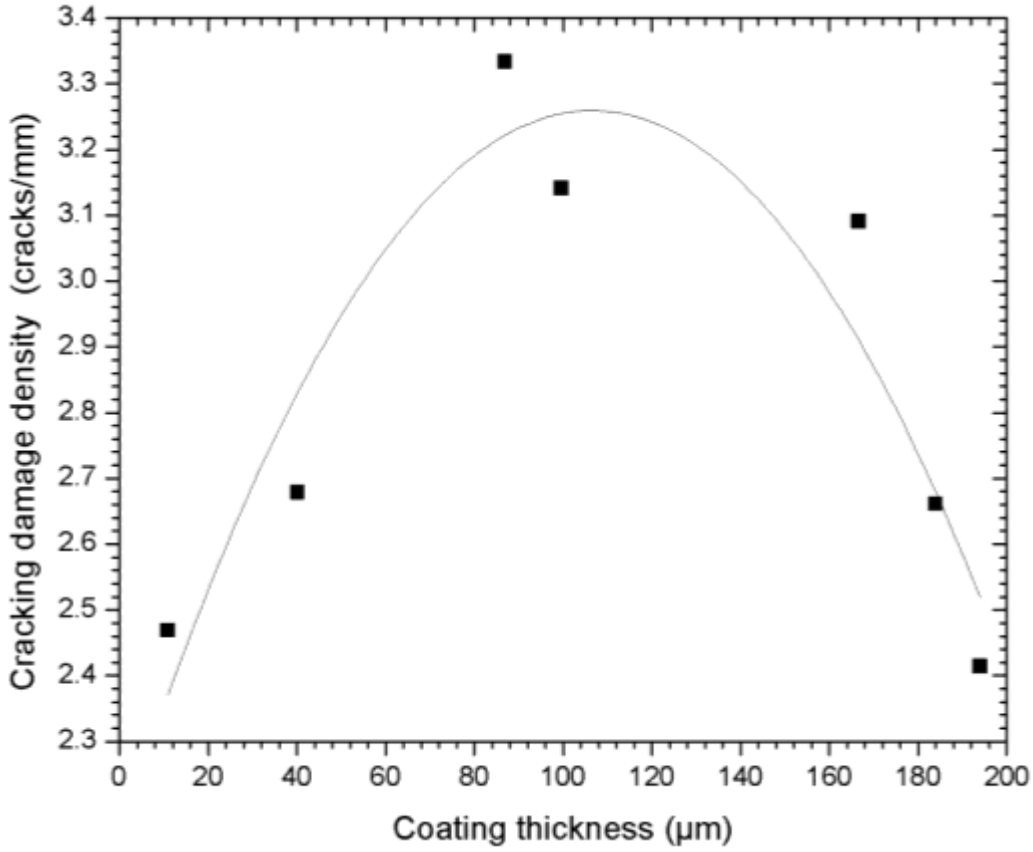

Figure 4-13 **Density of cracking due to indenting as a function of coating thickness.**

4.1.5.1 Thin Coatings (d ≤ 40 μm)

An example of the crack morphology for thin coating is shown in Figure 4-14 (b, c). The residual stresses in the thin thickness range are compressive as shown in Figure 4-6. In addition, inherent crack density is low (about 100 cracks/mm) compared to other regions (intermediate 133 cracks/mm, thick 154 cracks/mm). Two types of cracking patterns were observed in this region: ring and radial cracks. The former was likely due to Hertzian-type contact. This type of crack is initiated on the surface just outside the contact area where the maximum tensile principal stress (σ_{11}) is located and extended downward, initially propagates vertically then deviates sideways to form a cone as shown

in Figure 4-14 (c). The crack below the surface tends to extend along the σ_{33} trajectory [13], [48]. Rings in thin coatings can initiate if the applied load (P) exceeds the critical load (P_c), where P_c can be calculated using the following equation [16],

$$P_c = A\, S_c a^2 \left(\frac{E_s}{E_c}\right) \qquad \text{Equation 4- 1}$$

where E_s and E_c are the Young's modulus of the substrate and coating, respectively. S_c is the bulk strength of the coating. A is a proportionality coefficient and is given by $A = 2\pi/(1-2v_c)$ in Hertzian contact. Hertzian ring cracks may extend all the way through the coating. When crakcs reach the substrate, they stop propagating because the steel substrate is ductile and impedes crack propagation into the steel. Figure 4-14 (b) shows the surface of a representative image of cracking pattern in the thin coating region. Radial cracks were also initiated on the surface, but caused by the "hoop stress" (σ_{22}) [49]. During elastic-plastic contact, hoop stress becomes positive (tension) on the surface and equal to σ_{11} in magnitude [28]. Figure 4-14 (a) shows a schematic diagram of cracking damage in the thin coating region, where the upper view is the surface and lower view is the cross-section of the indentation. One can see the radial cracks and Hertzian ring cracks forming on the surface and extending downward and outward. Coatings in this region are approaching a membrane configuration as described by Chai [30] in which coatings are relatively flexible because they lack the thickness to support large bending loads. Instead, bending stress are concentrated near the edge of the indentation as evidenced by the sharp bend in the coating at the edge of the indentation. It is likely that the resulting bend cracks form in conjunction with the Hertzian cracks. For this reason, no ring or radial cracks due to bending are observed. The applied load is mostly

supported by the substrate which was evident by the large substrate plastic deformation compared to thick coatings.

Thin coating region, ($d \leq 40$ μm) Intermediate thickness coating ($40 < d \leq 184$ μm) Thick coating (d>184 μm)

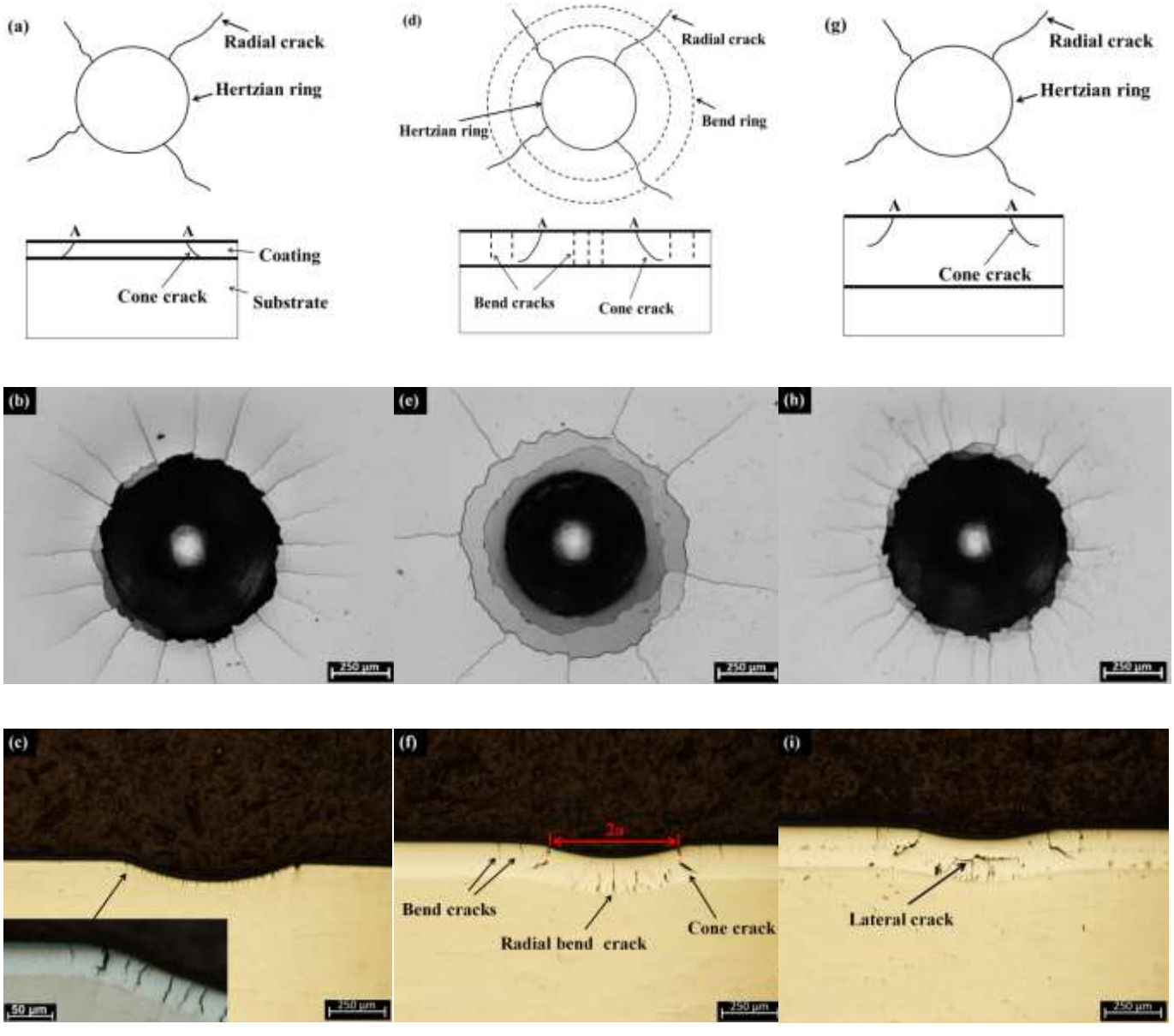

Figure 4-14 **Schematic diagrams and representative examples of thin, intermediate and thick coating crack morphology.**

4.1.5.2 Intermediate Coating (40 < d ≤ 184 μm)

Coatings in this region have tensile residual stress at the surface as shown in Figure 4-6. Inherent crack density of about 133 cracks/mm increases as a result of the increase in residual stress. Figure 4-14 (d) is a schematic diagram showing top and side view of indent. The figure shows the different cracks that develop in this thickness range. Figure 4-14 (e) is an optical micrograph showing a typical surface cracking pattern of coating with thickness in the intermediate range. Figure 4-14 (f) shows a representative profile morphology of the cracking damage under spherical indentation. Multiple ring and radial cracks are observed, but there are two types of ring cracks. The first is Hertzian-type ring crack and it is similar to that observed in thin coatings. The second is ring crack caused by bending of the coating. Ring cracks due to bending initiate when the applied load surpassed a critical load, which can be computed according to [30] for intermediate thickness,

$$P_c = \frac{(B' S_c d^2)}{log(C' E_s/E_c)} \qquad \text{Equation 4- 2}$$

where B' is a coefficient and d is coating thickness. Bend rings form outside the contact area, at distance R radially directed from the load axis, where R can be determined using the following equation [30],

$$R = b\, d\ \ log\, c\, E_c/E_s \qquad \text{Equation 4- 3}$$

where b and c are constant coefficients. In addition to being outside the contact area, they can be distinguished from Hertzian ring cracks by looking at the indent cross section as

shown in Figure 4-14 (f). Hertzian ring cracks extended downward and outward and forming a cone-shaped crack, while surface bend ring cracks extended downward vertically. Radial cracks also formed on the coating surface caused by hoop stress. In addition to surface radial cracks, bending of the coating induces tensile stress on the bottom surface of the coating causing radial cracks to initiate and extend upward to the surface. Radial and ring cracks caused by bending, drop with increasing thickness. One can notice that cone cracks did not penetrate to the substrate, yet they tend to deflect closely parallel to the interface [24]. This region has a mixed mode where Hertzian-type contact and coating flexural cracks both operate simultaneously.

4.1.5.3 Thick Coating (d>184 µm)

The last region is the thick coating region, in which, coatings are approaching monolithic material as shown in Figure 4-14 (h, i). Chromium coatings in this thickness range have residual tensile stresses at the surface that are higher than those in the intermediate coating region as shown in Figure 4-6 and a higher inherent crack density of about 154 cracks/mm at the surface. Hertzian ring cracks form on the surface at the edge of the contact area and are driven by the radial stress σ_{11}. They initiate when the applied load exceeded a critical load determined using [30],

$$P_c = A\, S_c a^2 \qquad \text{Equation 4- 4}$$

No surface bend ring cracks are observed because the thicker coating can support and distribute bending loads over a wider substrate area resulting in lower bending stresses in the coating. Similarly, no significant radial cracks are observed to initiate at the interface

between the coating and the substrate. The radial cracks formed on the coating surface are due to surface hoop stresses as a result of elastic-plastic contact.

Lateral cracks were observed in 4 samples out of 24. Delamination was also observed in 3 specimens. Indication that delamination and lateral cracks were not observed to be a major damage mode.

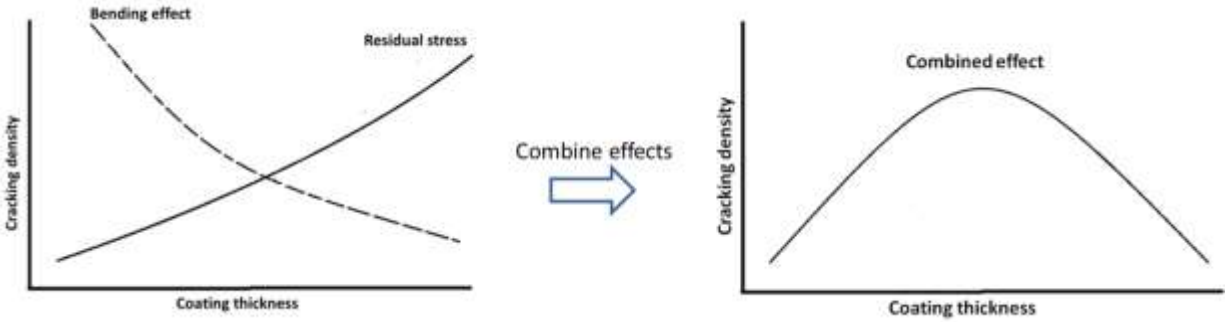

Figure 4-15 Schematic diagram of the effects causing cracking damage.

Trend in Figure 4-13 and Figure 4-14 can be better understood by considering the combined effects of bending and residual stresses. Bending effects decrease with increasing chromium coating thickness because thicker coating can resist bending more effectively than thinner ones. On the other hand, residual stresses increase as the plating thickness increases which promotes cracking damage. Furthermore, the inherent cracks associated with the residual stress increase and provide increasing sites for crack initiation. Consequently, the resultant effect of bending and residual stress reaches a highest value at intermediate coating thickness where the crack density caused by the indentation is the largest. The resultant effect is minimal for very thin and thick coatings where the cracking density is the smallest. Figure 4-15 demonstrates the idea of the combined effect. Note that as previously discussed, bending cracks for thin coatings are

not observed, as Figure 4-15 would suggest, because the cracks occur in conjunction with Hertzian cracks and are impossible to tell apart.

4.1.6 Summary

General characterization of the chromium coating was carried out. Chromium coatings exhibit excellent bonding to 416 stainless steel. Chromium coatings have inherent crack networks that form during plating process to release residual stress induced by the decomposition of chromium hydride to metallic chromium and hydrogen. Residual stress in the coating increases with increasing thickness leading to an increase in inherent crack density. The residual stress value at a given thickness is not affected by subsequent material deposits of chromium. Spherical indentation on chromium coatings causes different types of cracking damage including Hertzian cone, bend rings, surface radial and bottom surface radial cracks. Rare presence of lateral cracks and delamination indicates that they were not observed to be a primary failure mode. Damage severity increases with increasing load. Three thickness regions in which cracking pattern was different, were identified, namely thin, intermediate and thick coatings. Thin coatings are dominated by Hertzian ring and radial cracks. Intermediate coatings exhibit Hertzian and bend ring cracks, surface and bottom radial cracks. Thick coatings experienced Hertzian and radial cracks only. Indentation study suggests that two factors control cracking damage due to spherical indentation: bending effects and residual stress effects. The former increases with decreasing thickness, while the latter increases with increasing thickness. The combined effect is maximized at intermediate coating thickness and minimized for thin and thick coatings. The presence of diverse failure modes on hard

chromium coatings of 416 stainless steel due to indentation reveals the complexity of such damage. The present work provides a guide to hard chromium plating manufacturers on the appropriate thickness to be employed for a given application. The thickness should be higher than the point where the resultant effect of bending and residual stress is maximized. Thin coatings are not recommended as they may not be capable of supporting the operational load.

4.2 Thermal Damage

Investigation of thermal damage of chromium coatings is presented in this section. Sample 'E' plated for 16 hours was used for the heating effect study. The average chromium plating thickness was 167 ±7 μm, measured using an image analysis software, Image-Pro® Plus.

4.2.1 Mechanical Properties Results

The results of the Vickers hardness test on the plated surface are shown in Figure 4-16. There was no significant difference between the quenched and air cooled hardness values. Furthermore, hardness decreased substantially as the heating temperature increased. From room temperature to 600 °C, the hardness decreased by 15% and by a further 54% from 600 to 1000 °C. The Vickers hardness of the unheated specimen was included in the graphs at 25 °C. The substrate effect on the coating hardness was believed to be minimal since the coating thickness was 10 times larger than the impression depth for all samples. Vickers hardness measurements were also conducted on the substrate, as shown in Figure 4-17. Up to 800 °C, there was very little change in hardness. From 800

to 1000 °C, the data reveals that the substrate hardness more than doubled for both air cooled and quenched conditions. This increase was due to the formation of martensitic phase. When heating to 1000 °C, austenite forms and transforms to martensite upon rapid cooling. Because 416 stainless steel exhibits high hardenability, martensite can form even when air cooled. However, quenching can form more martensite than air cooling, which is evidenced by the difference in hardness as shown in Figure 4-17.

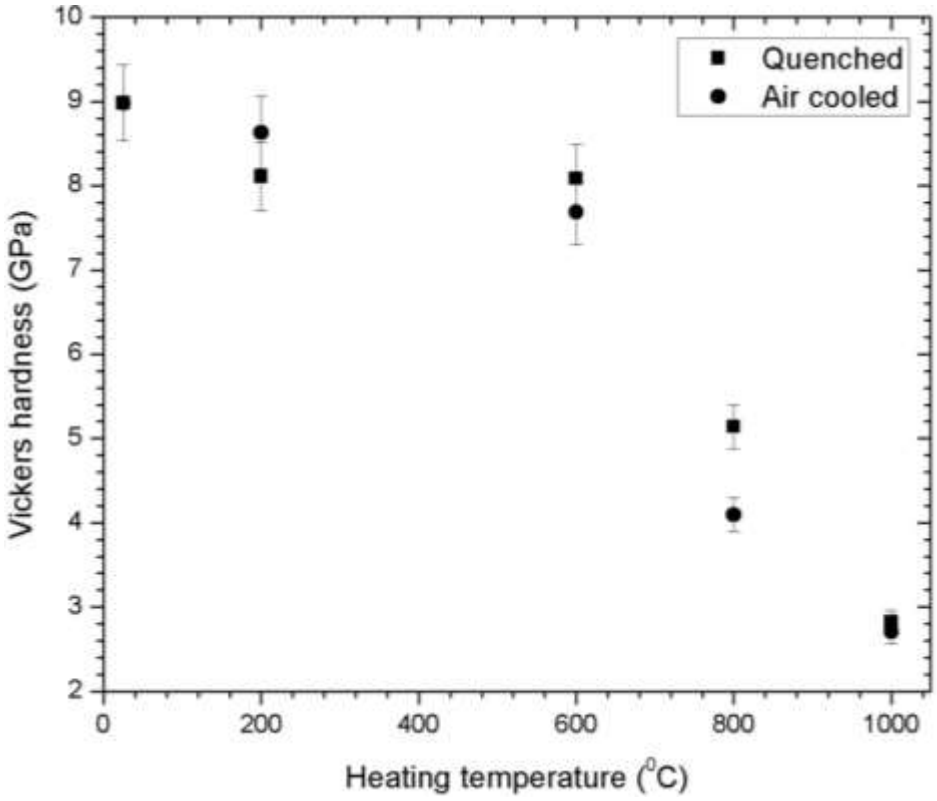

Figure 4-16 **Vickers hardness of quenched and air cooled coatings as a function of heating temperature.**

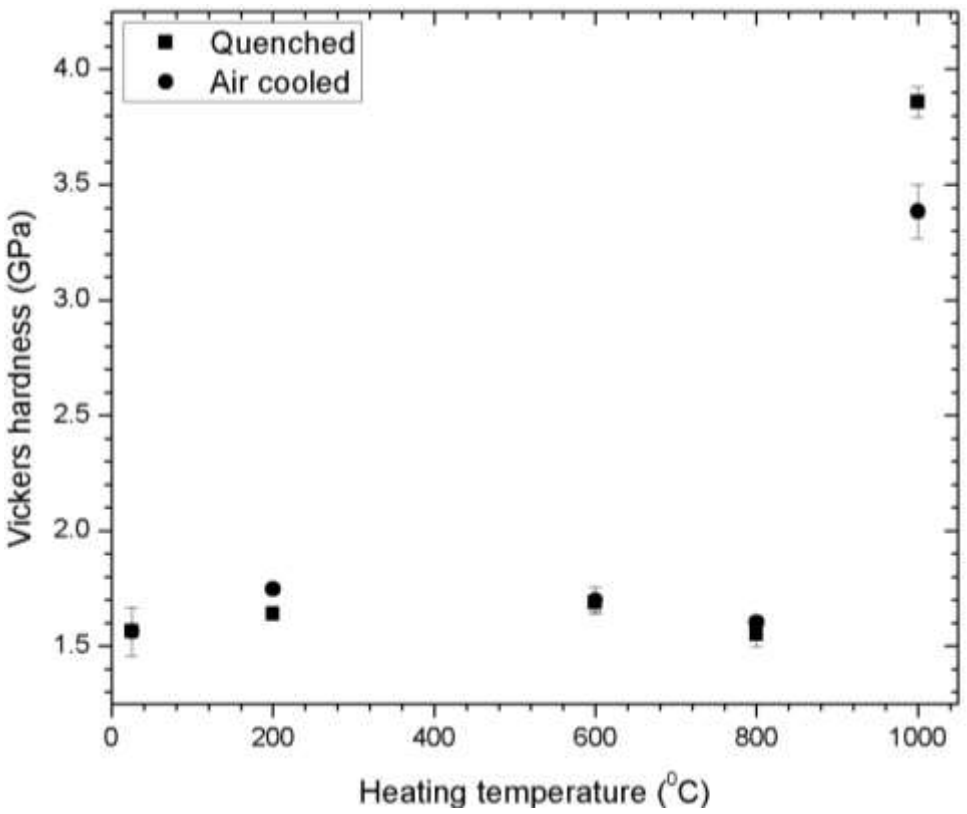

Figure 4-17 **Vickers hardness of the substrate as a function of heating temperature.**

4.2.2 Optical Microscopy Observation

The coatings were also examined using an optical microscope. A thin oxide film formed on the chromium coatings due to heating which was removed by fine polishing to make microstructural characterization of the coatings possible. The crack network on an unheated part is shown in Figure 4-18 for comparison purposes. Figure 4-19 shows micrographs of surfaces of the quenched and air cooled chromium coatings as a function of heating temperature. One can notice that up to 600 °C, no additional thermal cracks are visible. The cracking pattern is similar to that of the unheated surface shown in Figure 4-18. At 800 °C, thermally-induced cracks were formed on the coating surface. These cracks are likely a result of coating/substrate thermal expansion coefficient mismatch,

which is 7 μstrain/°C for chromium and 11 μstrain/°C for 416 stainless steel [46]. In other word, the steel substrate expanded at a higher rate than chromium during heating, thereby inducing tensile stresses. When the tensile stresses reached a critical value, cracks occurred. More cracks can be observed on the quenched specimens, which could be due to rapid cooling. Extensive cracking damage was observed when the coating was heated to 1000 °C and cooled. In addition to thermal expansion difference, the formation of martensite, discussed earlier, increased the volume of the substrate and induced additional tensile stress on the coating surface. Thermally-induced cracks seem to follow and extend the inherent cracks.

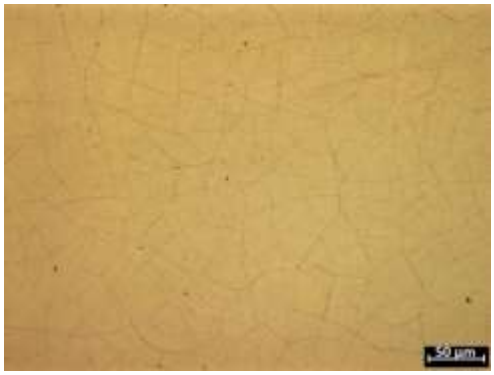

Figure 4-18 Optical micrograph showing polished surface of unheated specimen.

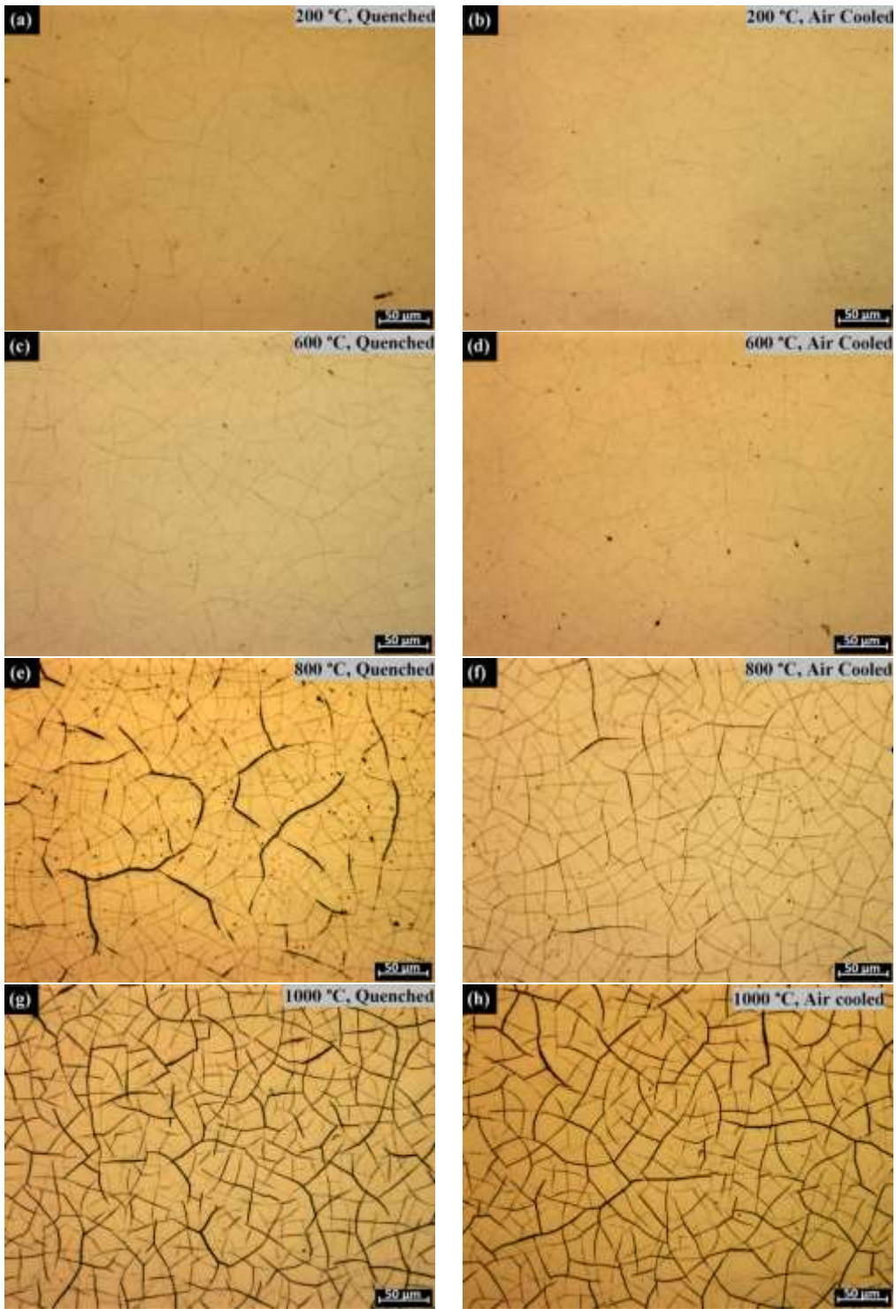

Figure 4-19 **Optical micrographs showing coating surface heated at (a) 200 °C and quenched, (b) 200 °C and air cooled, (c) 600 °C and quenched, (d) 600 °C and air cooled, (e) 800 °C and quenched, (f) 800 °C and air cooled, (g) 1000 °C and quenched and (h) 1000 °C and air cooled.**

Observation of specimens cross-sections revealed similar results to those of coating surfaces in terms of thermal damage, as shown in Figure 4-20 and Figure 4-21 (close up of coating). No thermally-induced cracks can be observed up to 600 °C. Thermal cracks start at 800 °C and increased with temperature. No significant difference in cracking damage between quenched and air cooled specimens were observed. Inherent cracks became longer and some connected to other cracks forming much longer cracks, but inherent cracks did not extend from the surface to or into the substrate. Cracks formed on the surface were observed extending downward into the coating for a few microns. Cracks parallel to the substrate were also formed in the coating. Coating delamination at the interface was not observed.

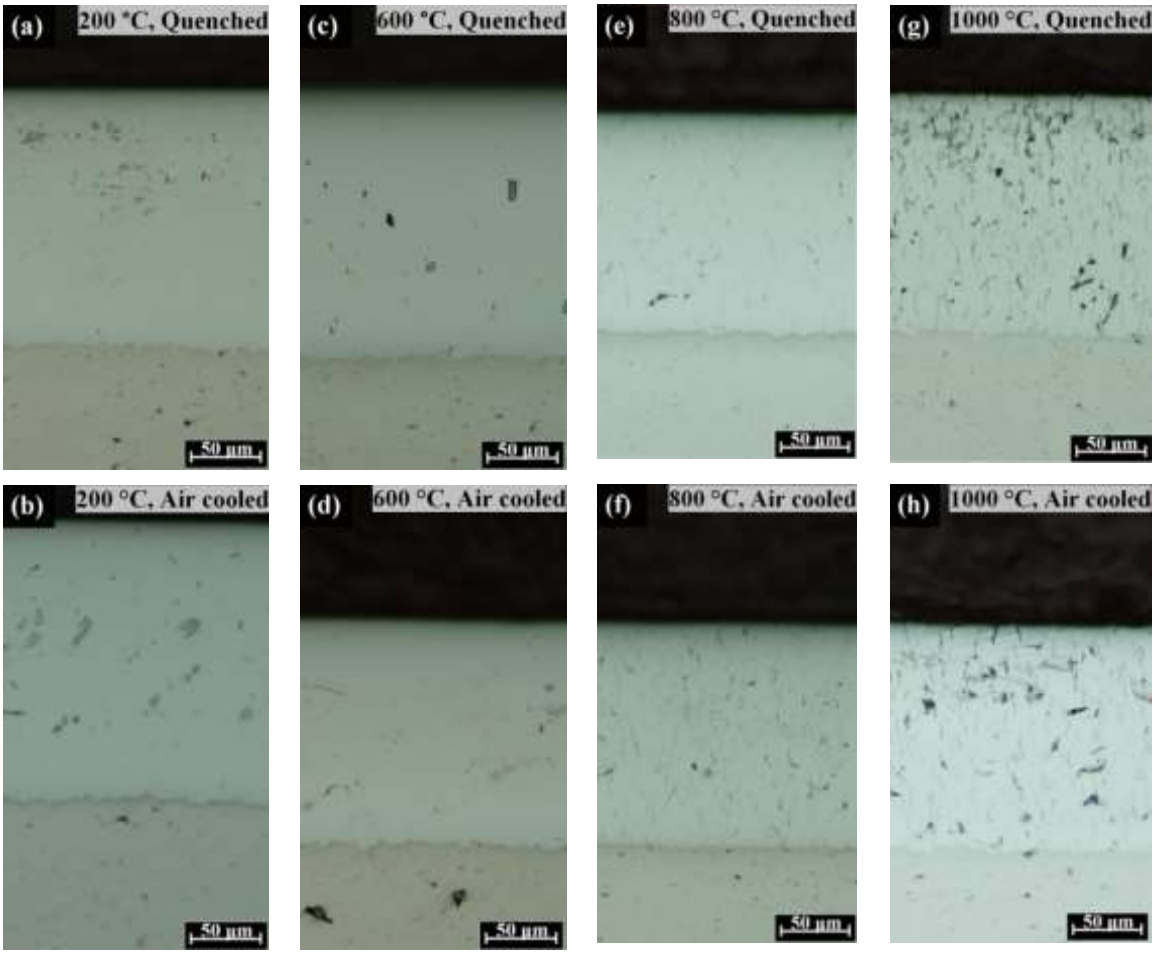

Figure 4-20 **Micrographs showing cross-sections of thermally cycled coating (a) 200 °C and quenched, (b) 200 °C and air cooled, (c) 600 °C and quenched, (d) 600 °C and air cooled, (e) 800 °C and quenched, (f) 800 °C and air cooled, (g) 1000 °C and quenched and (h) 1000 °C and air cooled.**

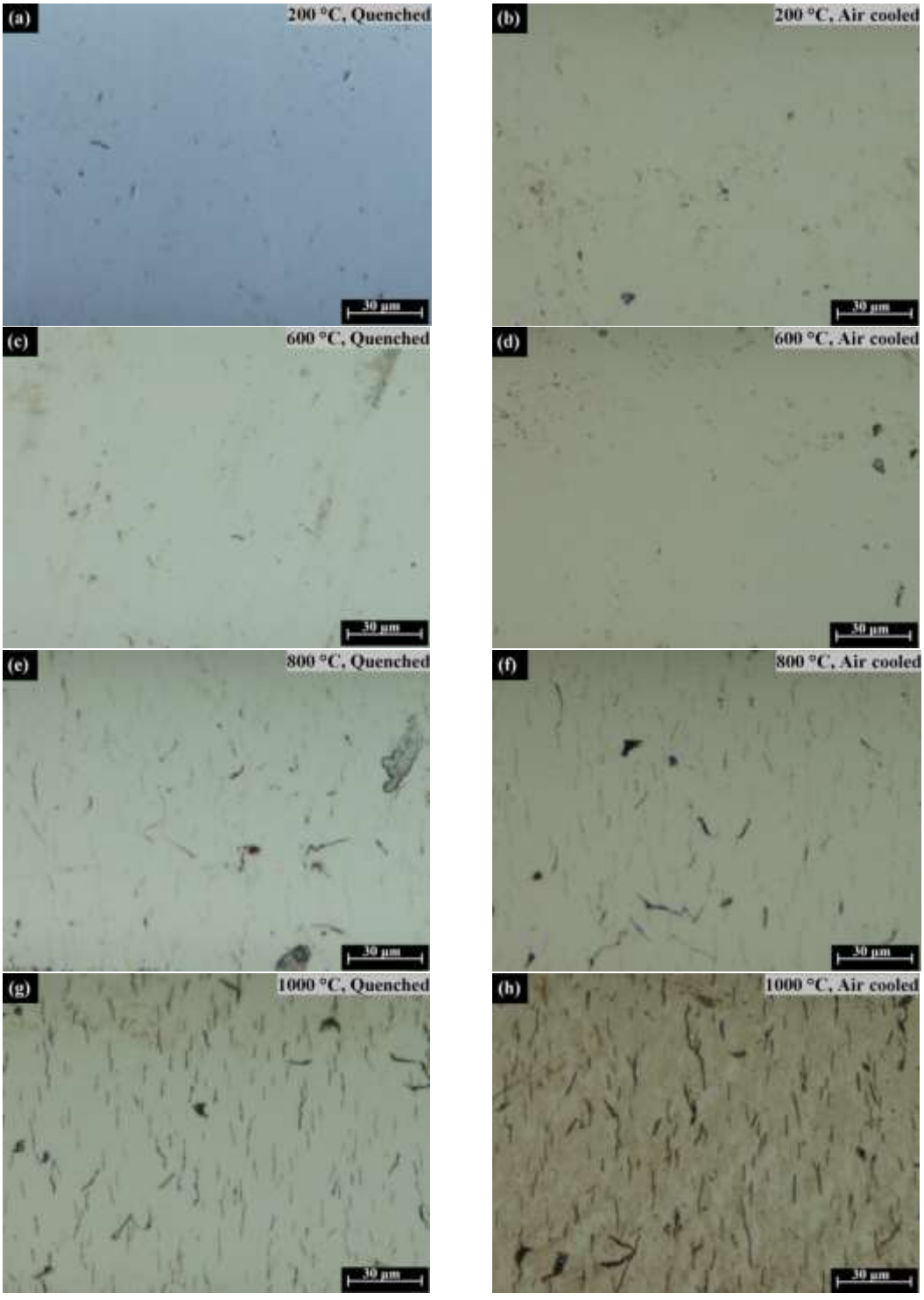

Figure 4-21 **Close up images showing the inherent cracks on the coating cross-section heated at (a) 200 °C and quenched, (b) 200 °C and air cooled, (c) 600 °C and quenched, (d) 600 °C and air cooled, (e) 800 °C and quenched, (f) 800 °C and air cooled, (g) 1000 °C and quenched and (h) 1000 °C and air cooled.**

4.2.3 Cracking Density of Coating Cross-Section

The proceeding observations were quantified using the Nascimento and Voorwald [43] technique described earlier and presented in Figure 4-22. These crack densities include the inherent ones as well as the cracks induced thermally. It is clear that there is no significant difference between quenched and air cooled samples in terms of cross-sectional crack density. Beyond 600 °C, a remarkable increase in crack density can be seen explaining why the coating hardness drops off rapidly at 600 °C. At 1000 °C, the crack density is 41% higher than the unheated sample.

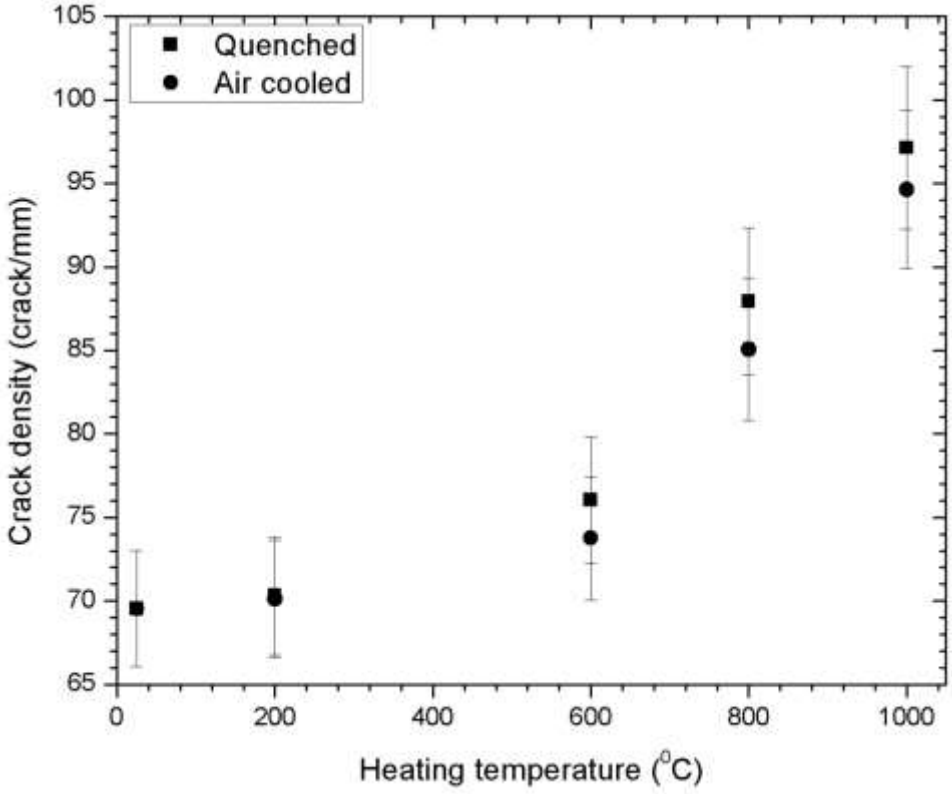

Figure 4-22 **Cross-sectional density of cracks as a function of heating temperature.**

4.2.4 Residual Stress Results

XRD was used to determine the residual stresses on the coating surfaces. Figure 4-23 shows the maximum and minimum principal stresses on the surface of quenched and air cooled chromium coatings as a function of heating temperature. Residual stresses on the coating surface heated to 600 °C doubled for both quenched and the air cooled sample as compared to as-deposited coating. Maximum principal stresses of the quenched and the air cooled coatings increased from 260 to 552 MPa and to 589 MPa, respectively. This large increase is believed to be due to thermal expansion coefficient mismatch between the coating and the steel substrate. During cooling the coating surface cooled faster than the stainless steel core. As a result, the surface tensile stresses remain on the coating surface as the coating/substrate cool. It is worth mentioning that these residual stress values were slightly less than the tensile strength of chromium which is around 650 MPa [46], and evidently was not high enough to initiate crack formation which would have released some of the residual stress. At 1000 °C, the quenched chromium coating exhibits compressive stresses, around -15 and -300 MPa for maximum and minimum principal stresses, respectively. Cracking due to the thermal expansion coefficient mismatch and martensite formation released the existing tensile residual stress which caused the residual stresses on the coating surface to drop (Figure 4-23). Moreover, heating to 1000 °C caused the austenitic phase to form which transformed to martensitic phase upon rapid cooling by quenching. Martensite formation was evidenced by the large increase in substrate hardness (see Figure 4-17). After cracking and releasing of residual stresses, further cooling of the steel substrate core might have caused an additional drop in surface residual stress placing the coating surface in compression. Air cooling is expected to

produce less martensite; as a result, the surface of air cooled chromium coating exhibited tensile stress. Coatings were isotropic except for the sample air cooled at 600 °C and sample quenched at 1000 °C as indicated by the gap between maximum and minimum principal stresses.

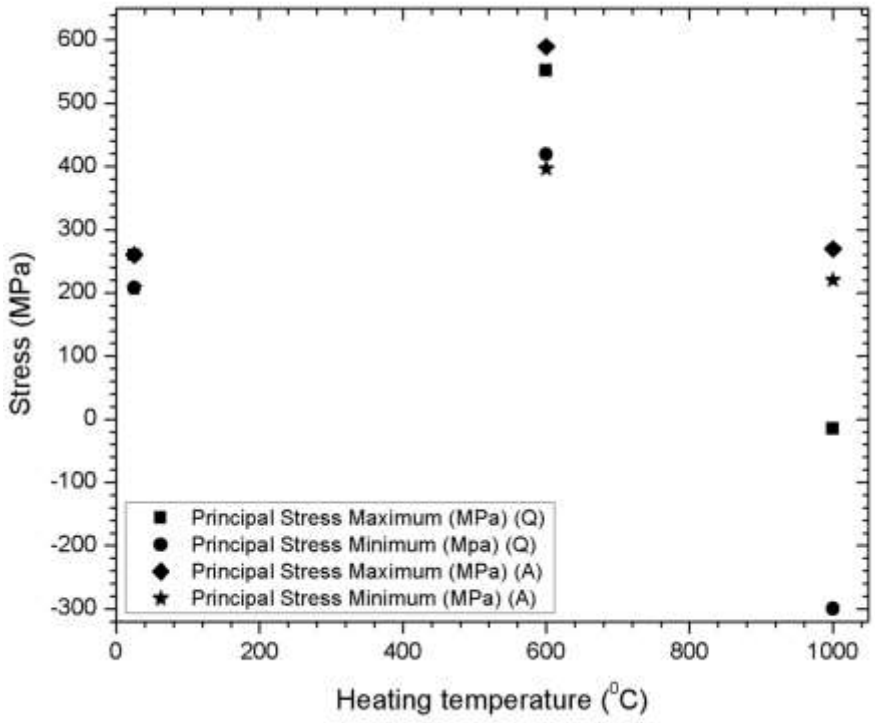

Figure 4-23 **Residual stress of quenched (Q) and air cooled (A) chromium coatings as a function of heat treatment temperature**

4.2.5 Indentation Results

An indentation study was carried out to evaluate the mechanical damage of the chromium coatings after thermal cycling. Profilometry scans were also performed on individual indentations and analyzed to obtain geometric features such as, depth, width, and volume of indentation impressions. Unheated specimen revealed similar damage mode to that of intermediate coating thickness region as shown in Figure 4-14 (e, f). Figure 4-24 and

Figure 4-25 show the top and cross-sectional views of indentations on the specimens that received heating. Up to 600 °C, similar damage modes to those of as-deposited samples were observed. Coatings heated up to 800 °C showed less cracking. Partially developed ring and radial bend cracks were observed. At 800 °C surface radial cracks due to indentation totally disappeared. At 1000 °C, no cracks due to indentation were observed. Instead, the material piled up around the indentation. Pile-up is a feature that is usually exhibited by ductile materials. It is believed that chromium coatings heated to 1000 °C exhibit pseudo-ductile behavior. They act similar to ductile materials at the macroscale, but they are brittle and fracture at the microscale [50].

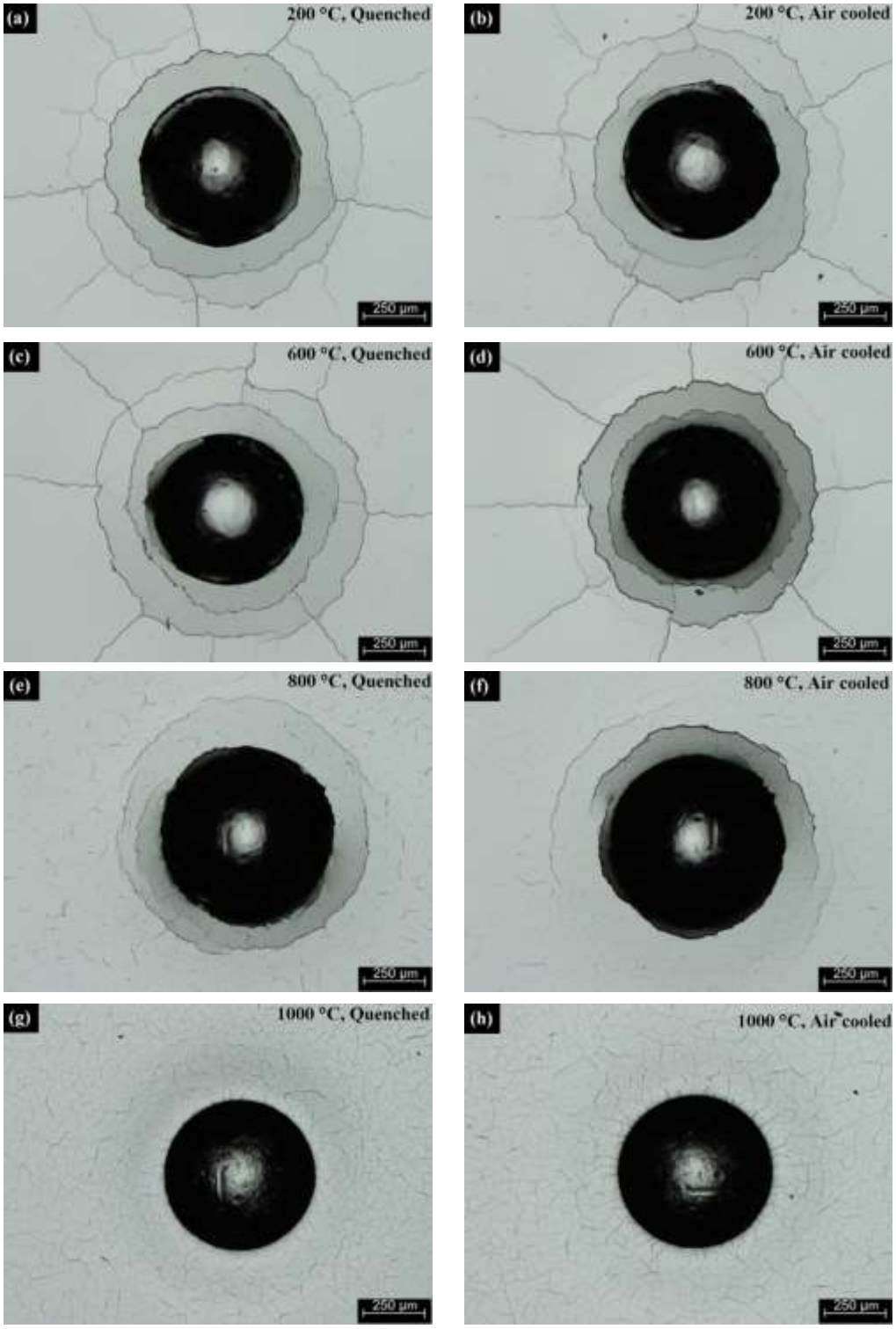

Figure 4-24 **Micrographs showing top view of indentation on specimens heat at (a) 200 °C and quenched, (b) 200 °C and air cooled, (c) 600 °C and quenched, (d) 600 °C and air cooled, (e) 800 °C and quenched, (f) 800 °C and air cooled, (g) 1000 °C and quenched and (h) 1000 °C and air cooled.**

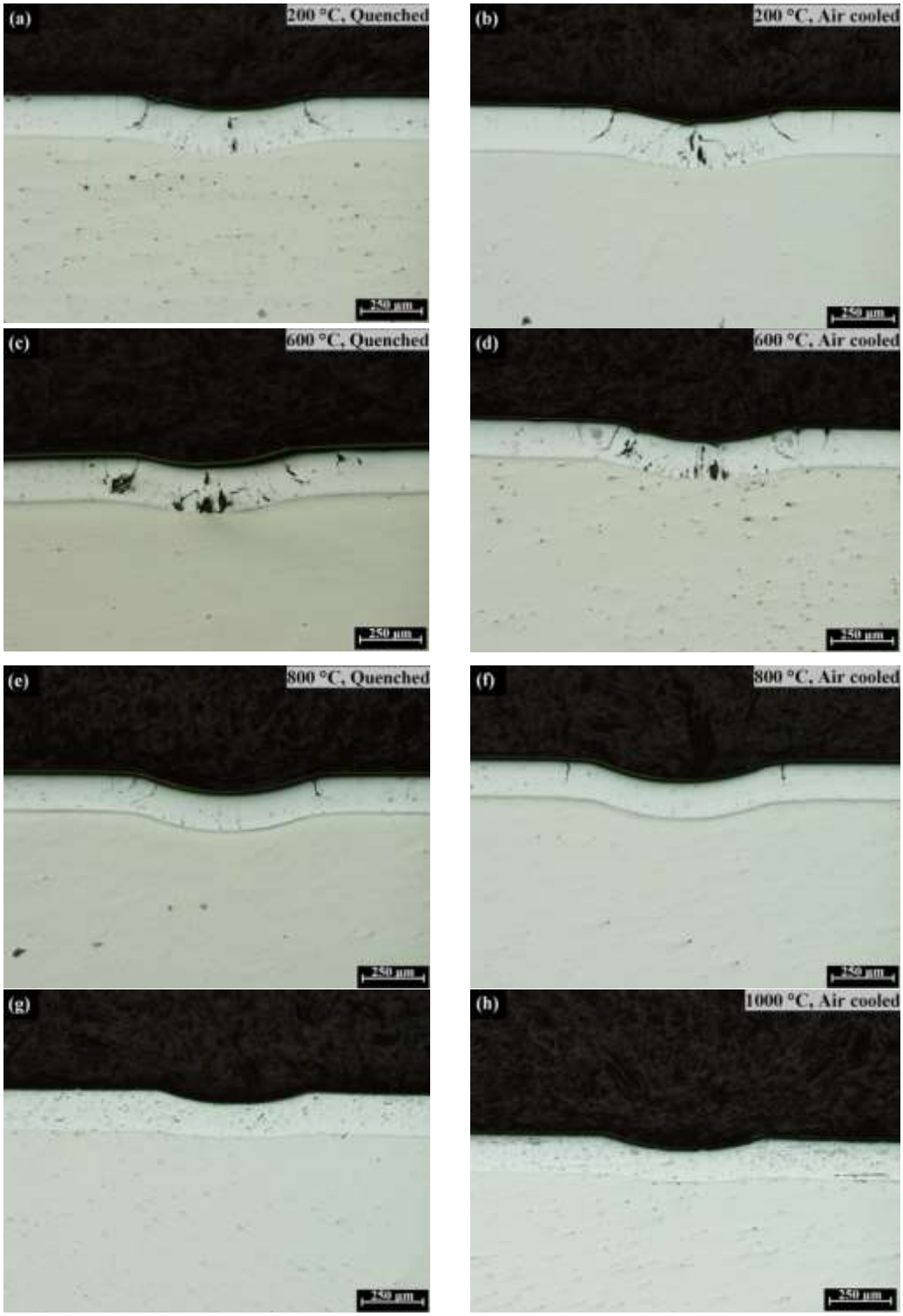

Figure 4-25 **Micrographs showing cross-sectional view of indentation on specimens heat at (a) 200 °C and quenched, (b) 200 °C and air cooled, (c) 600 °C and quenched, (d) 600 °C and air cooled, (e) 800 °C and quenched, (f) 800 °C and air cooled, (g) 1000 °C and quenched and (h) 1000 °C and air cooled.**

The volume of the indentation impressions were measured from profilometry scans and plotted as a function of heating temperature, as shown in Figure 4-26. Representative examples of indentation profile are presented in Figure 4-27. Up to 600 °C, there was no significant change in terms of indentation volume. At 800 °C, there was a remarkable increase in impression volume. This is due to the fact that chromium coating cracked as a result of heating as shown in Figure 4-19 (e, f) and cannot resist loading as those coatings which did not thermally crack. As a result, the mechanical response to indentation loading was dominated by the substrate plastic deformation. The impression volume of the indentations on specimens heated to 1000 °C was the smallest among all specimens. This is because the substrate became harder as a result of martensite formation. Observation of indentation cross-section revealed that coating displacement was higher than that of the substrate. This occurred because the chromium flows around the indentation rather than pushing and deforming the hard substrate as shown in Figure 4-24 (g, h) and Figure 4-25 (g, h). Compared to as-deposited sample, indentation profiles obtained from the scans confirm optical microscopy observation for the pile-up material around indentations in specimens heated up to 1000 °C, as shown in Figure 4-27 (C).

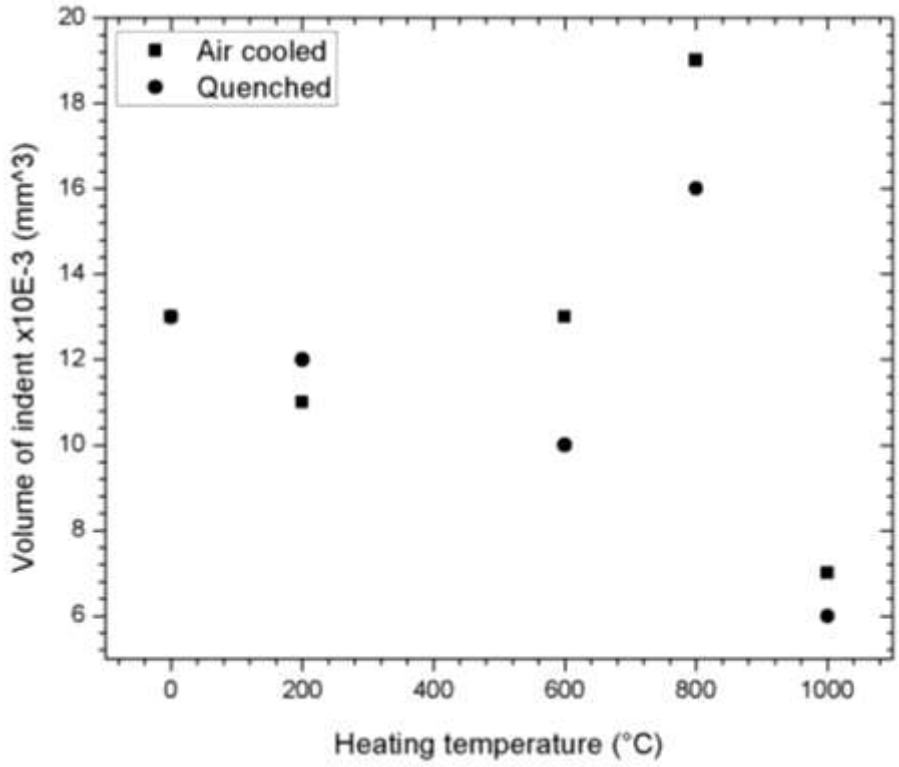

Figure 4-26 Volume of indentation as a function of heating temperature.

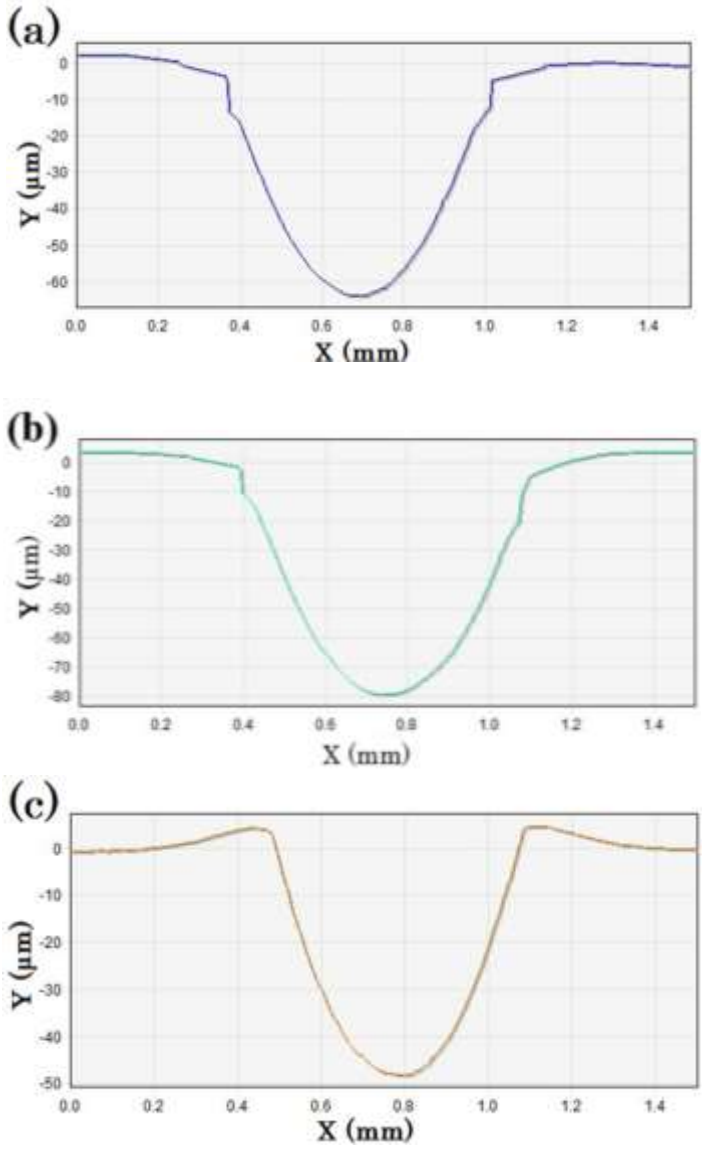

Figure 4-27 **Indentation profile of (a) as-deposited (b) heated at 800 °C and quenched (c) heated at 1000 °C and quenched samples (aspect ratio is 1:12).**

4.2.6 Summary

Thermal damage of chromium coatings and its effect on mechanical damage was investigated as a function of heating temperature and cooling rate. The samples were heated to different temperature and then cooled down either by water quenching or by air cooling. The hardness of thermally cycled coatings decreases as heating temperature

increases. No thermal damage was observed up to 600 °C. At 800 °C, the density of thermally-induced cracking damage increased. There was no significant difference between quenched and air cooled specimens in terms of thermally-induced cracks. Thermal cracks formed to release tensile stresses induced by the thermal expansion coefficient mismatch between the coating and the substrate. Heating extended the inherent cracks. At 1000 °C, martensite formed in the stainless steel substrate during cooling, which further increased cracking damage as well as hardened the substrate. Residual stresses in the coating surface were affected by both heating temperature and cooling method. Residual stresses increased when the samples heated to 600 °C due to the thermal expansion coefficient mismatch. Hertzian-type indentation tests were carried out on the coated specimens. The as-deposited sample and those heated up to 600 °C exhibited the same pattern of cracking damage due to indentation: ring, cone, surface radial and radial bend cracks. At 800 °C, indentation damage showed partially developed ring and radial bend cracks. Pseudo-ductile deformation was observed on the specimen heated to 1000 °C as a result of indentation loading and no indentation cracks were observed. Furthermore, the hardened substrate reduced the volume of indentation impression and forced the chromium coating to pile up on the sides of the impression.

4.3 Detailed Investigation of Indentation Damage for Intermediate Coating Thickness

The big picture of the mechanical damage of chromium coatings due to spherical indentation as a function of thickness has been obtained. In this section, an intermediate coating thickness (167 μm) was selected for a detailed investigation. This is because in the intermediate coating thickness region, a combination of bending and residual stress effects takes place resulting in a variety of damage modes. Furthermore, a novel method of determining strain is applied to these samples.

4.3.1 Focused Ion Beam Circles Analysis on Coating Surface

After FIB circles were created on the surface of the sample, an indentation test was performed. Figure 4-28 shows an optical image of the damage due to indentation made on the surface. As expected, the crack patterns observed in this study were the same as those observed in the optical studies for the same thickness range, specifically, a mix of radial and ring cracks. It was observed that no cracks initiated at the center of the indentation when examined from the top view of the indentation, as shown in region A of Figure 4-29. This is because the coating surface is under compressive stress at the center of indentation. At some radial distance, ring and surface radial cracks begin to form. It is believed that ring cracks form once the applied load reaches a critical load [24]. Similarly, radial cracks form once a second critical load is reached, during the elastic-plastic loading, which implies that ring cracks occur before radial cracks [24], [28]. Since chromium is brittle, it will not undergo plastic deformation. However, the 416 stainless steel substrate does exhibit plastic deformation under loading. The resulting indentation is

a combination of the brittle fracture of the coating and the plastic deformation of the substrate. For this work, the elastic-plastic region occurs when the substrate undergoes plastic deformation.

A novel use of FIB and SEM imagery will be used to investigate the deformation in the 416 stainless steel substrate. When a crack interacts with a FIB circle, material displacement can be observed and, therefore, stress direction causing crack initiation can be determined and the order of radial vs ring crack can be determined. For instance, one can observe that in Figure 4-30, which is a magnified image of region B in Figure 4-29, part of the FIB circle has been cracked and displaced after fracture. It is believed that the crack is caused by principal radial stress σ_{11} perpendicular to crack opening direction and then pulled by hoop stress σ_{22}.

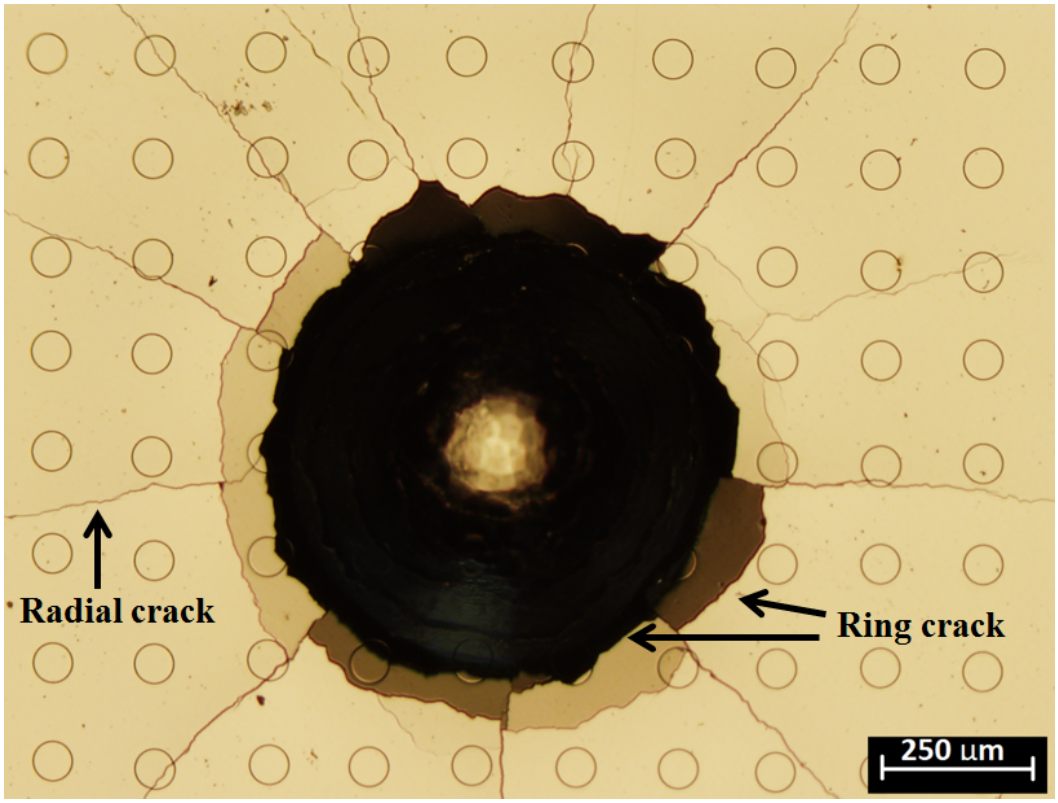

Figure 4-28 An optical micrograph showing indented surface.

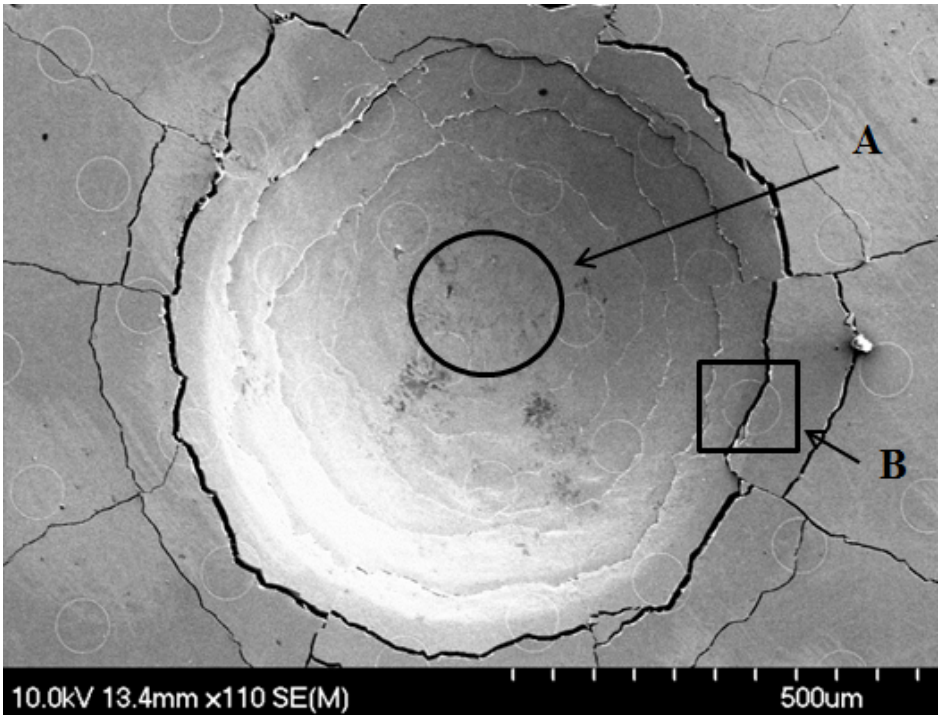

Figure 4-29 **An SEM micrograph showing a more detailed image of the inside the indentation.**

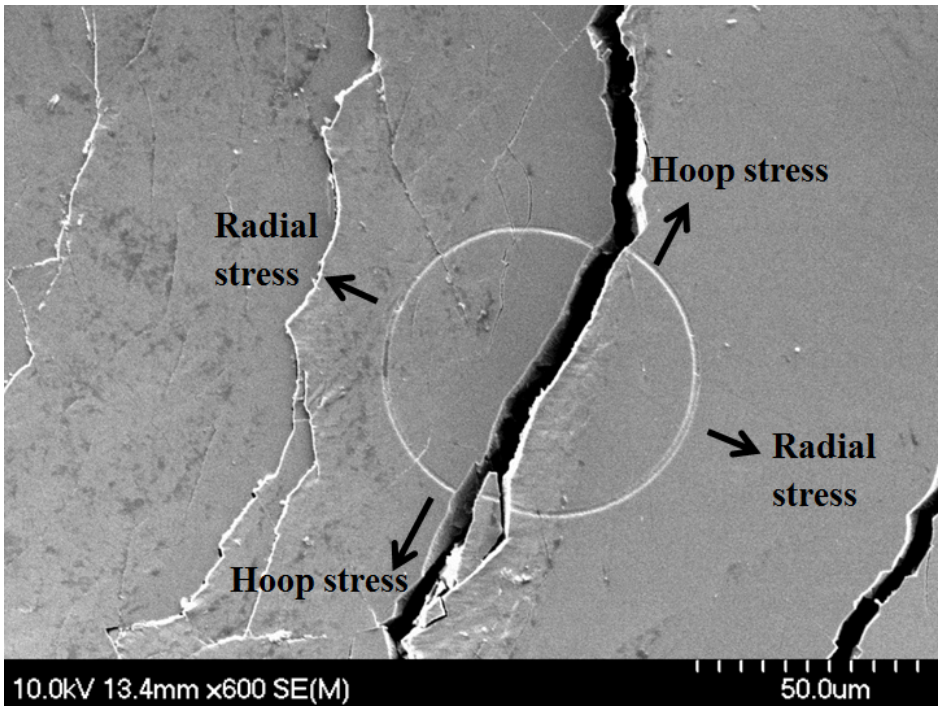

Figure 4-30 **A magnified image of region B in Figure 4-38 showing a cracked circle due to indentation and the direction (arrow) of principal stress causing fracture.**

4.3.1.1 Interactions of Indentation Cracks

Indentation cracks are those caused by indentation loading, such as ring and radial cracks. To help understanding the formation of indentation cracks in chrome coatings, ring/radial crack interaction was examined. Figure 4-31 shows micrograph of an indented specimen where ring and radial cracks interact. At some distance from the contact center, the Hertzian ring crack H_1 formed as a result of radial stress followed by the radial crack R_1 caused by the hoop stress. This order occurred because Hertzian cracks form during elastic deformation, while radial cracks develop during elastic-plastic contact. The order of crack formation can be identified by examining the radial/ring intersections. When two cracks are propagating in different directions, the crack that formed first would prevent the intersecting crack from propagating further. For example, crack H_2 formed and subsequently followed by crack R_2. Subsequently, Hertzian cracks H_3 and H_4 formed but could not cross radial crack R_2.

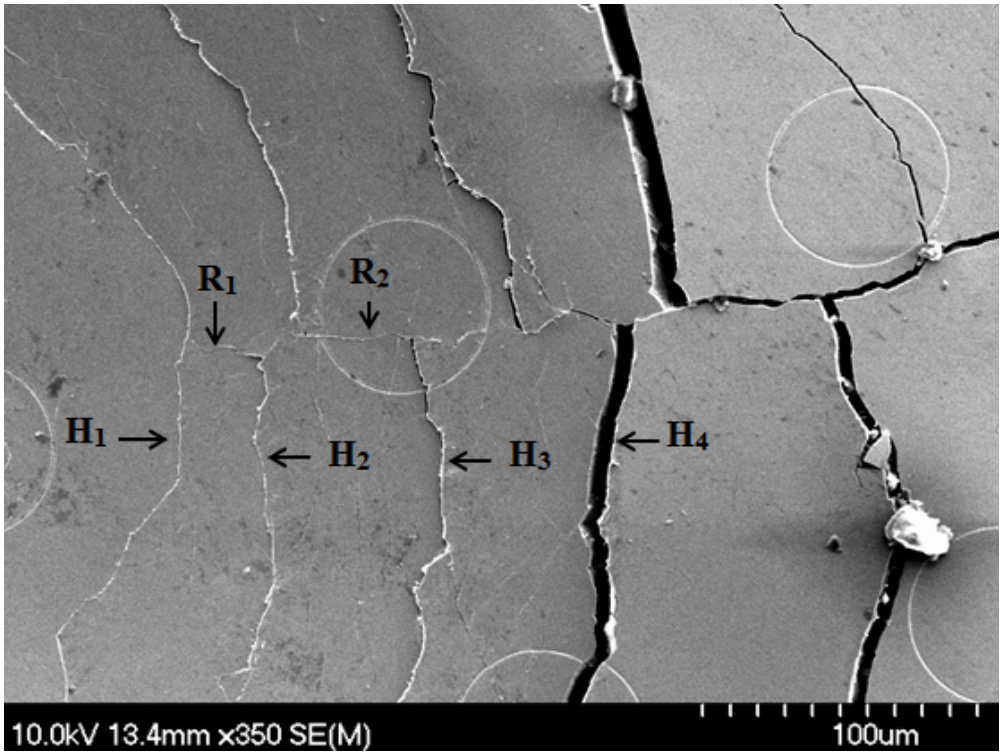

Figure 4-31 **Hertzian and radial cracks interaction occurred during indentation.**

4.3.1.2 Inherent and Indentation Cracks Interactions

One can also notice that most cracks do not propagate in perfect straight lines. That is due to the fact that crack propagation generally follows the path of less resistance. In this case are inherent crack. Figure 4-32 (a) shows an overall view of the whole indentation and Figure 4-32 (b) is a magnified micrograph of region C. One can observe that the radial crack changed its path when it encountered an inherent crack as it provided an easy path for propagation. The direction change in the radial crack path was for a short distance because the radial crack was forced to follow the maximum stress direction which is not in the same direction as the inherent crack. This figure also shows a radial crack initiated at an inherent crack suggesting that inherent cracks are also location of crack initiation.

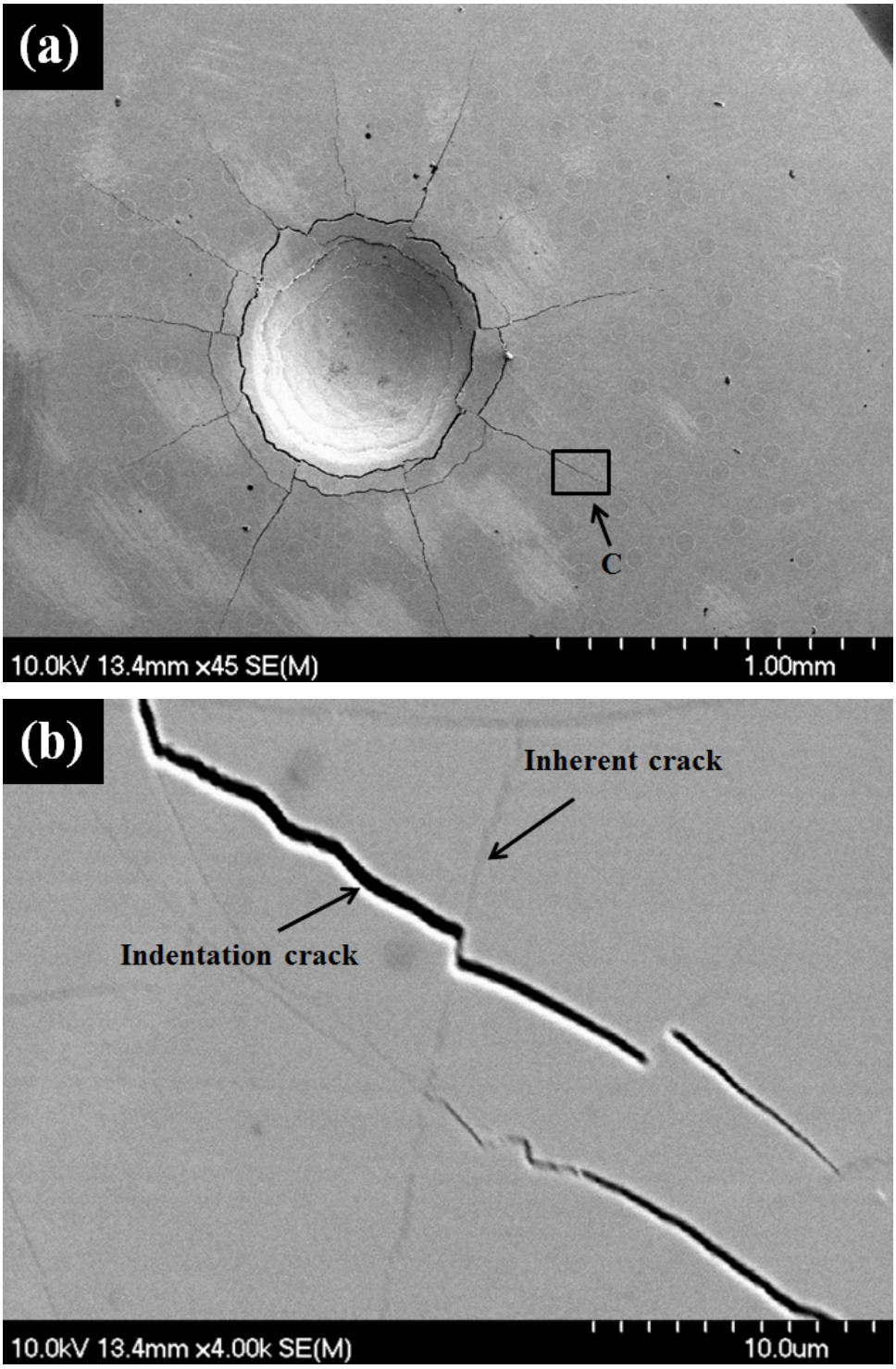

Figure 4-32 **(a) SEM micrograph showing the whole indentation (b) a magnified image of region C showing inherent crack and indentation crack interaction.**

4.3.2 Focused Ion Beam Circles Analysis on Coating Cross-Section

SEM examination of FIB circles on the coating cross-section was conducted after indentation, as shown in Figure 4-33. Boxes ‘a’ though ‘f’ indicate the regions were higher magnification SEM images were taken. The diameters of the FIB circles were measured on the coating and on the substrate. There was no change in diameter of FIB circles located on the coating cross-section pre and post indentation. For example, Figure 4-34 is a magnified micrograph of region ‘a’ of Figure 4-33 showing a FIB circle that did not crack due to indentation. The diameter of this circle was 32 μm before and after indentation. This indicates that the chromium coatings did not plastically deform. Instead, chromium coating cracked when the induced stress exceeded the bulk strength of the chromium because of the brittleness of the chromium coatings. Circles on the stainless steel substrate were distorted due to plastic deformation forming an elliptical shape, as shown in Figure 4-35 which is a magnified image of region ‘b’ in Figure 4-33. Figure 4-36 is a magnified micrograph of region ‘c’ of Figure 4-33 showing a circle at the coating/substrate interface where the circle cracked on the coating and deformed on the stainless steel substrate.

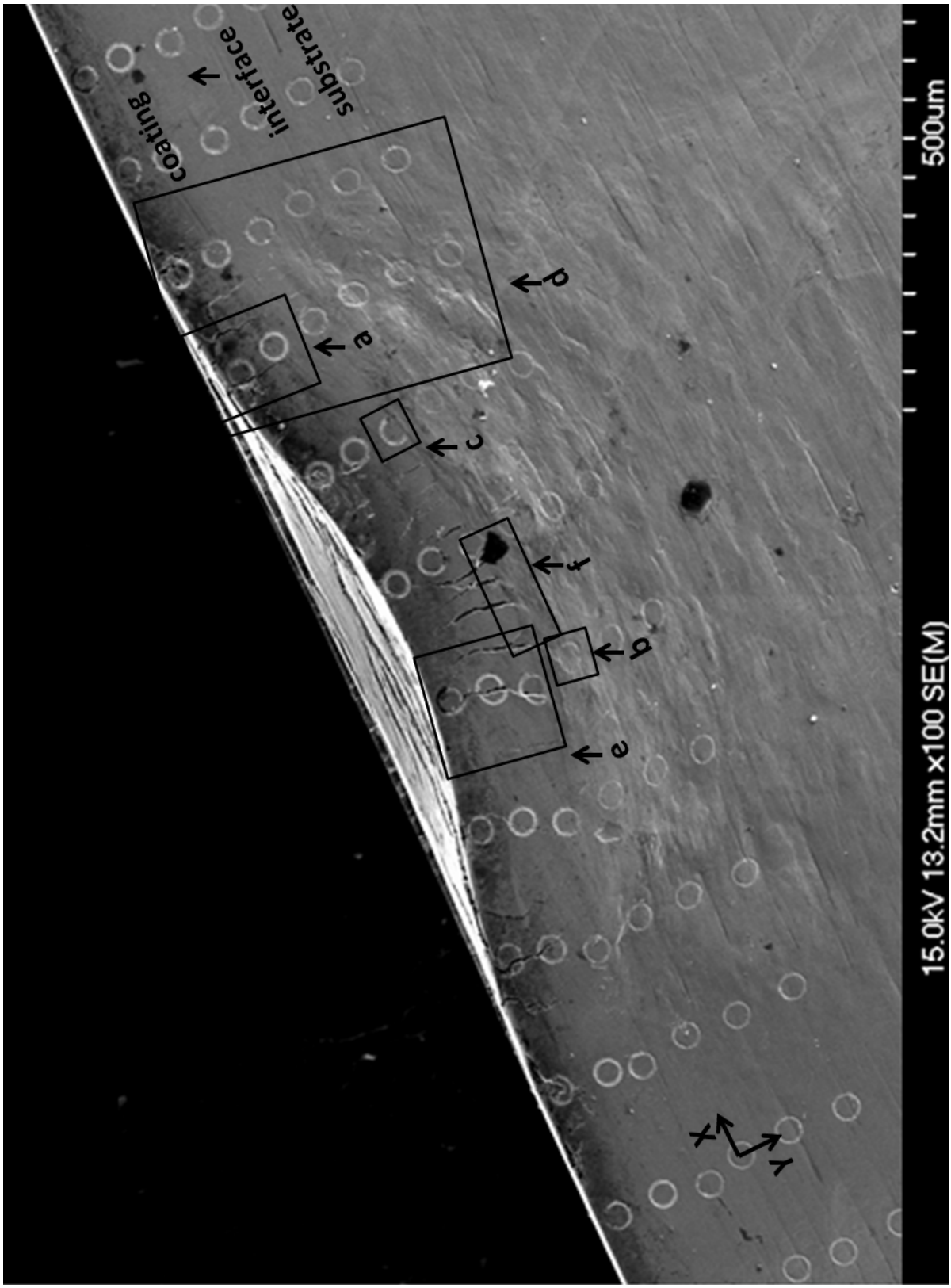

Figure 4-33 SEM image of the indentation cross section showing the circles.

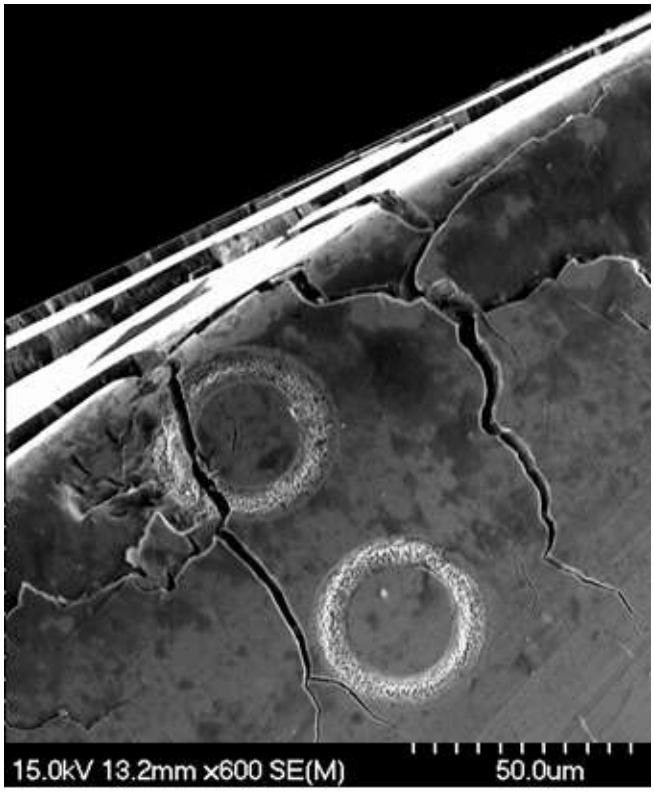

Figure 4-34 **A magnified SEM image of region 'a' in Figure 4-33 showing a circle made on the coating that did not change due to indentation**

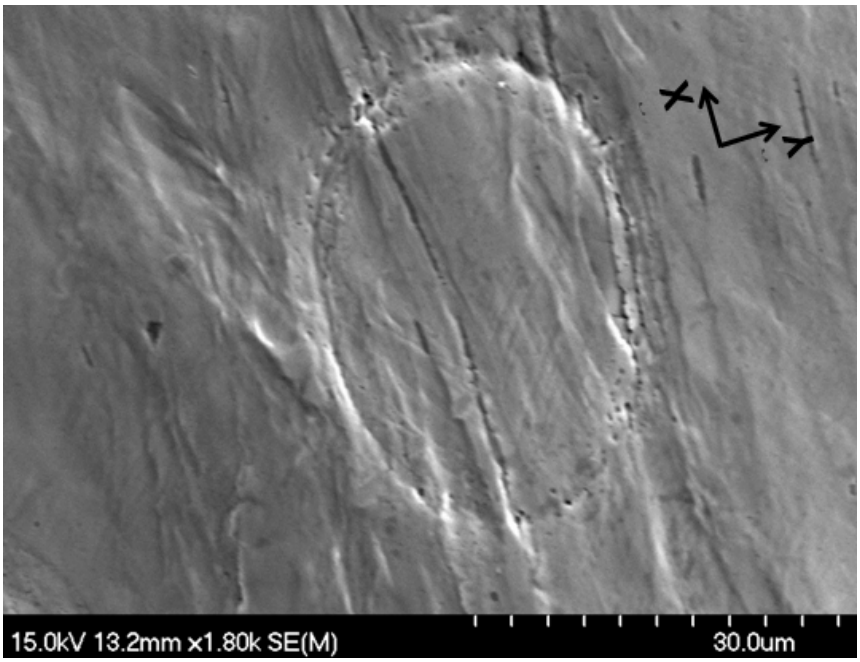

Figure 4-35 **A magnified micrograph of region 'b' in Figure 4-33 showing a circle made on the substrate and distorted due to indentation.**

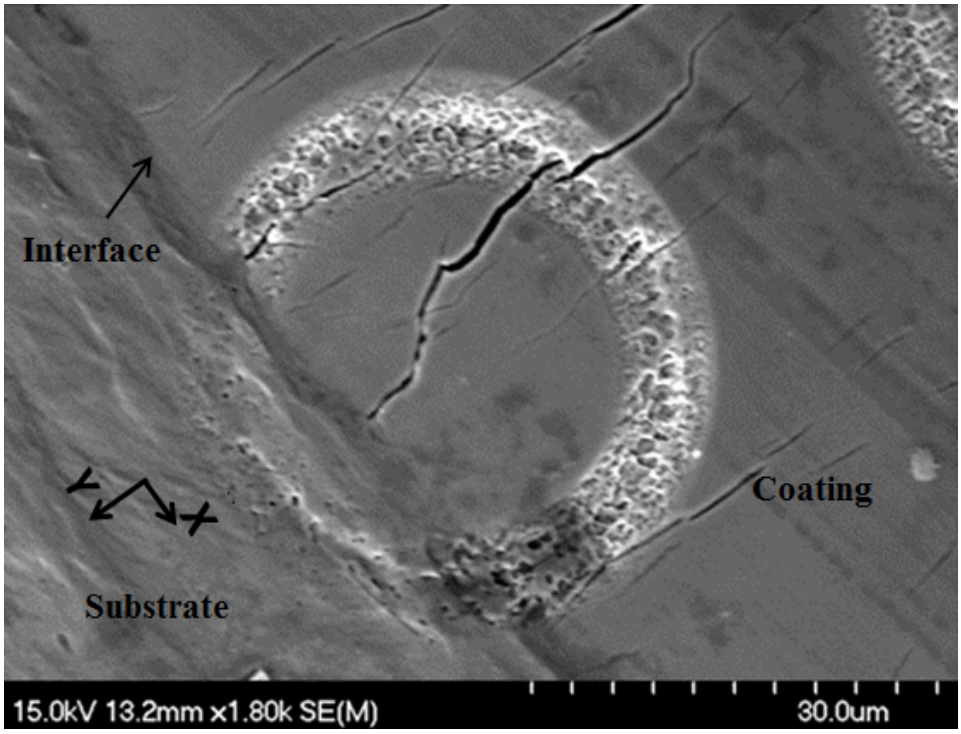

Figure 4-36 A magnified SEM micrograph of region 'c' in Figure 4-33 showing a circle on the coating/substrate interface.

4.3.2.1 Damage Modes on Coating Cross-Section

In this sub-section the different types of cracks (damage modes) in the cross section are identified and discussed. Figure 4-37 is a magnified image of region 'd' of Figure 4-33. Figure 4-37 shows how the radial and Hertzian cracks formed on the surface interact with each other. One can see the radial cracks coming from the back intersecting Hertzian cracks. Hertzian cone cracks initiate at the surface and extend downward at an angle with the loading axis. Region 'e' of Figure 4-33 is magnified in Figure 4-38. Bend radial cracks initiated at the interface extend upward, as shown in Figure 4-38. The crack edge having the wider opening indicates the location of crack initiation, where the maximum stress occurred. Delamination occurred in region 'f' due to indentation, as shown in Figure 4-39.

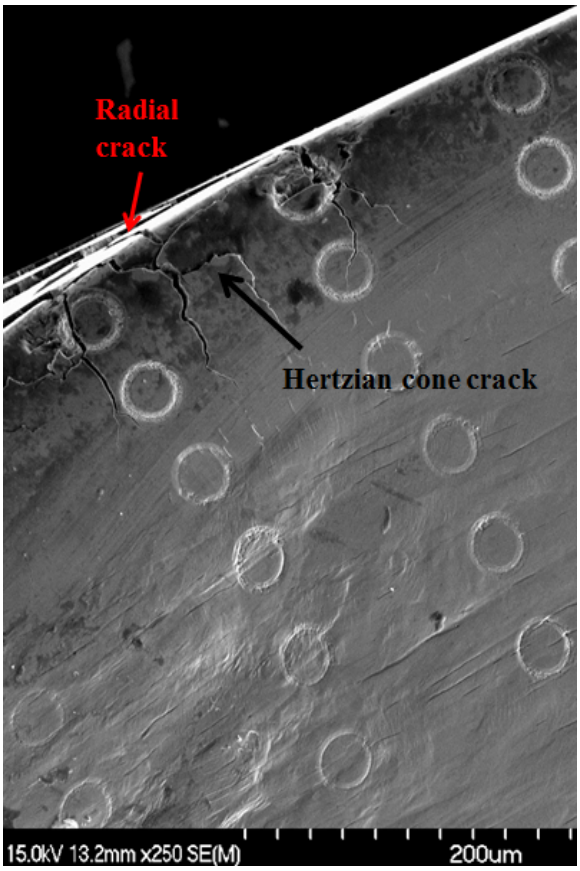

Figure 4-37 **A magnified SEM image of region 'd' in Figure 4-33 showing radial/Hertzian cracks interaction**

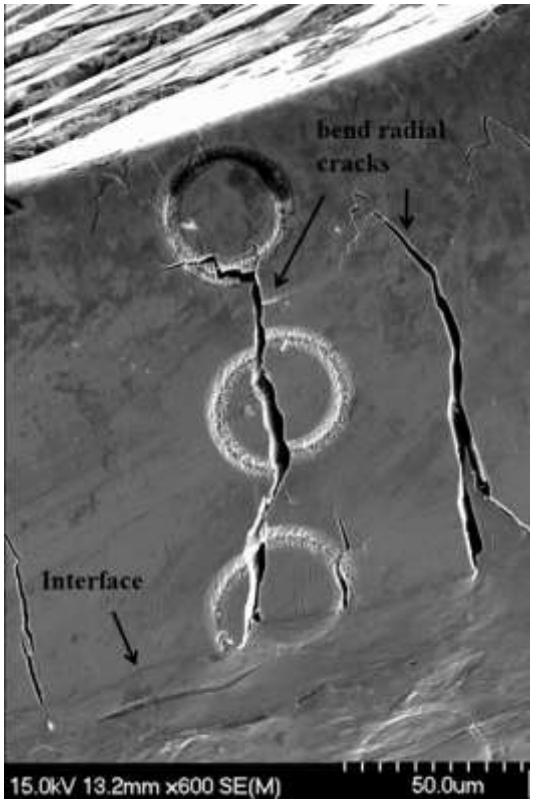

Figure 4-38 **A magnified micrograph of region 'e' in Figure 4-33 showing bend radial cracks initiated at the interface.**

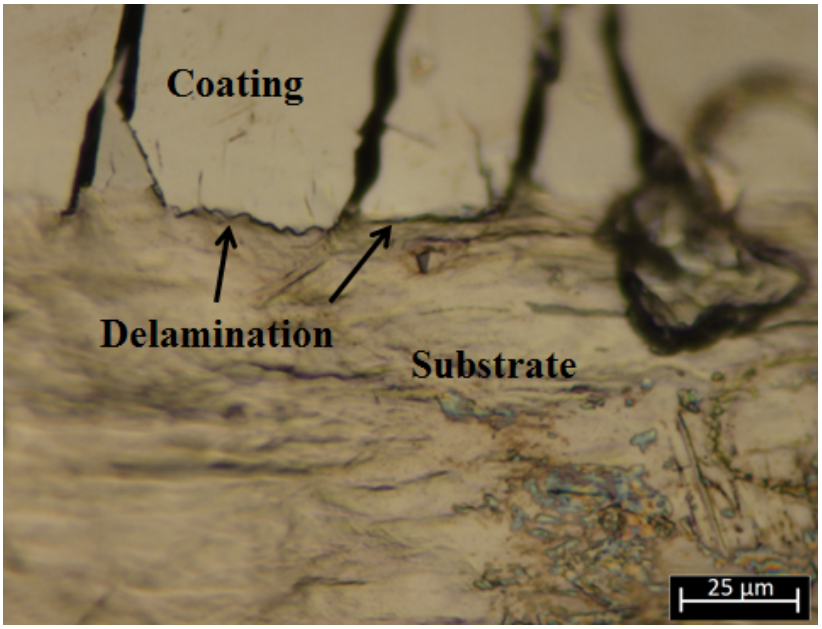

Figure 4-39 **A magnified optical micrograph of region 'f' in Figure 4-33 showing delamination at the coating/substrate interface due to indentation.**

4.3.2.2 Strain Contours and Directions of Substrate

Major and minor strains and their directions in the stainless streel substrate due to indentation were determined from FIB circles, as discussed in section 3.8. Shear strain developed at each individual circle was calculated. Contours of major, minor and shear strains are shown in Figure 4-40. An array of circles that was 3 circles deep and 10 circles wide was used for these calculations. The frame of reference (upper left hand corner of the array) is shown in Figure 4-33. Although the stress distribution that caused the strain distributions shown in Figure 4-40 could not be measured directly, it is reasonable to assume that it would be similar to the strain distribution. The directions of major and minor strains are shown in Figure 4-41 (a) and (b), respectively. It was found that the major strain follows the principal radial stress σ_{11} trajectories shown in Figure 2-6 and reproduced in the insert of Figure 4-41 (a). Furthermore, the minor strain is in the same direction as the normal principal stress σ_{33}. Therefore, it is believed that major strain was caused by principal tensile stress σ_{11}, while the minor strain is caused by the principal compressive stress σ_{33}, as described by the Hertzian contact theory.

For a Hertzian stress distribution, the radial stress σ_{11} is compressive below the indenter and its magnitude decreases down to zero, as shown in Figure 4-42 (left). Subsequently, σ_{11} becomes tensile and increases until it reaches a maximum value, after which it starts drop. However, the distribution in Figure 4-40 (a) is somewhat different. The maximum stress is tensile in the middle section and there is no compressive stress at all. It is believed that the region of the compressive stress occurred within the coating and could not be measured due to the brittle nature of chromium. Only the region of positive stress occurred in the substrate, as shown in Figure 4-42 (right).

Similarly, the distribution of principal stress σ_{33} was different from that of Hertzian contact of monolithic materials shown in Figure 4-43 (left). In Hertzian contact, the principal stress σ_{33} is essentially compressive everywhere in the contact zone. Its magnitude reaches a maximum value just below the indenter and decreases with increasing depth below the surface. However, the contours in Figure 4-40 (b) show that the highest compressive strain was around 100 μm below the interface. It is believed that coating delamination shown in Figure 4-39 released some of the compressive stress close to the interface. This led to a decrease in the compressive stress in the vicinity of the interface.

The contours of the shear strain are in agreement with the shear distribution of Hertzian contact of monolithic materials shown in Figure 4-44. The maximum shear stress occurred at a distance below the indenter. In addition to the justifications discussed above, Hertzian contact assumes that the contact is elastic, but the indentation in this study is elastic-plastic contact which may slightly alter the stresses distribution. The FIB circle method makes it possible, for the first time, to analyze the stress (strain) distribution of spherical indentation experimentally.

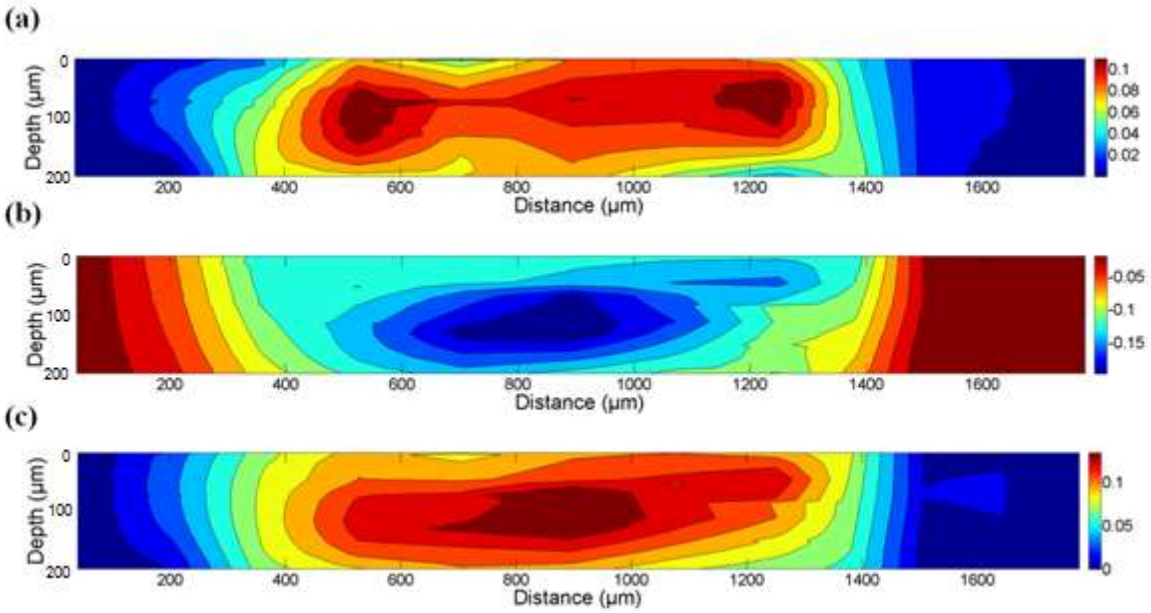

Figure 4-40 **Contours of (a) major (b) minor and (c) shear strain experienced by the circles on the stainless steel substrate.**

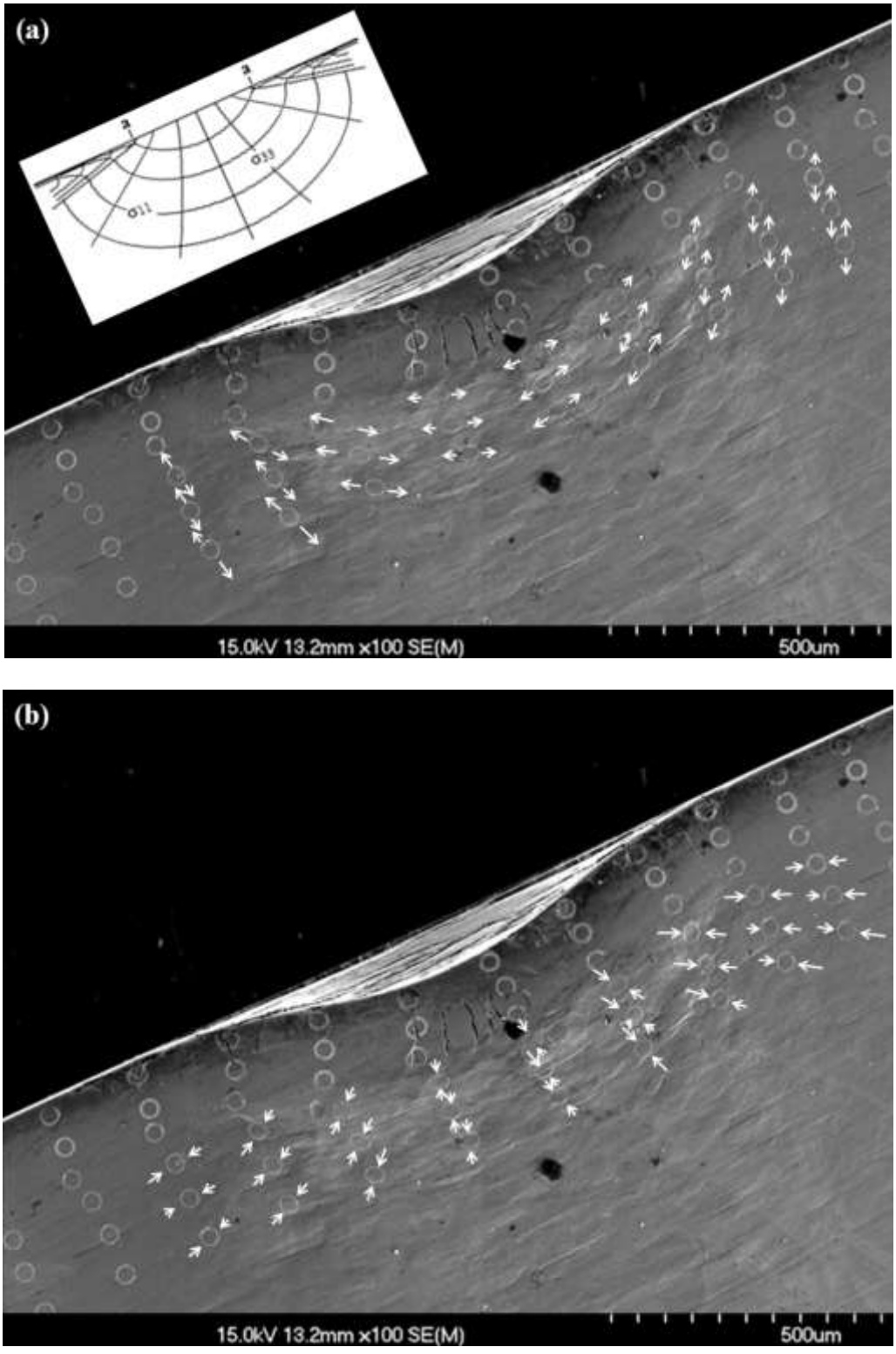

Figure 4-41 **Direction of (a) major and (b) minor strain for each individual distorted circle on the substrate.**

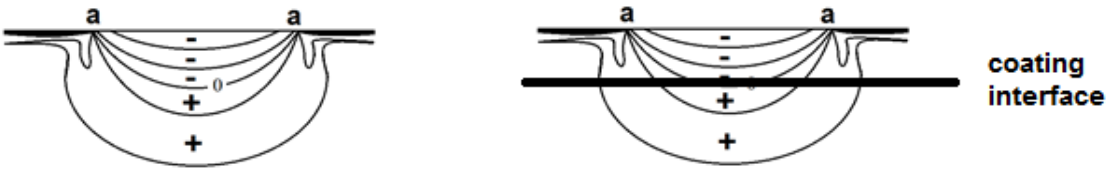

Figure 4-42 **Stress contours of σ_{11} due to Hertzian contact (left) and the effect of coating on the stress contours (right).**

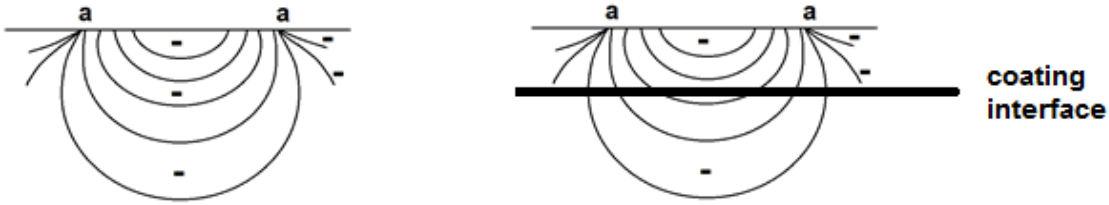

Figure 4-43 **Stress contours of σ_{33} due to Hertzian contact (left) and the effect of coating on the stress contours (right).**

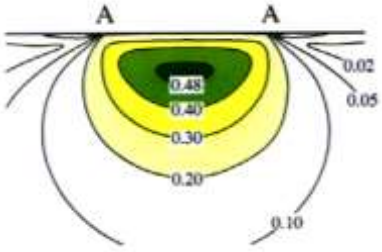

Figure 4-44 **Contours of principal shear stress due to Hertzian contact [13].**

4.3.3 Summary

A detailed investigation of mechanical damage using FIB circles provided insight on the behavior of chromium coatings during indentation. Cracked circles on chromium coating surface helped identify the direction of stresses acting on the coating due to indentation. Ring cracks form first during elastic loading, while radial cracks form during elastic-plastic loading. Major and minor strain contours and direction on steel substrate due to indentation were determined. Major and minor strain directions were similar to those of

principal radial stress σ_{11} and principal stress σ_{33}, respectively. Contours of strain distribution were plotted and compared to those of Hertzian contact of monolithic materials. Differences in trends between experimental and theoretical Hertzian distribution are related to the presence of the chromium coating and the plastic-elastic behavior. The novel technique developed in this work assisted to analyze the stress distribution experimentally.

Chapter 5

Conclusions

The first objective was to investigate the mechanical damage of hard chromium coating as a function of coating thickness and load. To achieve this objective, a series of spherical indentations were carried out as a function of coating thickness using different loads (60, 100, 150 kg). It was found that coating bending and residual stresses significantly affect the extent of coating damage. The mechanical damage of the chromium coatings as a function of coating thickness is characterized by three regions, namely thin, intermediate, and thick coating. Each region has a distinctive damage pattern. Thin coatings are predominated by Hertzian ring and radial cracks. Intermediate coatings experienced Hertzian and bend ring cracks and surface and bottom radial cracks. Thick coatings exhibit Hertzian and radial cracks only. Increasing the load did not change cracking pattern, but increased the severity of the damage. This indicates that the stress distribution does not change with changing load, only magnitude.

The second objective was to investigate the thermal damage of hard chromium coatings as a function of heating temperature and the effect of heating and quenching on the mechanical response of the coatings. Coated specimens were heated to different temperatures (200, 600, 800, 1000 °C) and then cooled down by water quenching or by air cooling. Heated specimens were then indented with a spherical indenter using 100 kg

load. Optical microscopy observations revealed that no thermally-induced cracks were observed up to 600 °C. Beyond 600 °C, thermal cracks were observed and increased with temperature. Thermally-induced cracks were caused by heat cycling due to the thermal expansion coefficient mismatch between the chromium coating and the stainless steel substrate. At 1000 °C, martensite formed in the substrate due to the heat cycling, which led to increase in the thermal crack density. Thermally-induced cracks had a significant effect on the mechanical response of chromium coatings. At 800 °C, indentation damage exhibited partially developed ring and radial bend cracks. At 800 °C, Pseudo-ductile behavior was observed as a result of indentation loading and no indentation cracks were observed. Further, the hardness of the substrate substantially increased due to martensite formation that led to a dramatic decrease in the volume of the indentation impression.

The third objective was to investigate inherent and indentation cracks interactions and to study the strain distribution on the substrate due to spherical indentation. A detailed investigation was conducted for accomplishing this objective. It was found that when an indentation crack encountered an inherent crack, the damage crack follow the inherent crack for a short distance as the later provides an easy path for crack propagation. Lastly, a novel technique was developed to investigate the deformation in the substrate. FIB circles were machined on the coating cross-section to examine any distortion caused by the indentation. Strain values and directions were determined. Strain contours were plotted and compared to those of Hertzian monolithic materials.

This research work provides chromium plating manufacturers with insight on processes that may take place during grinding, i.e, accidental overloading and overheating. The study also have shown that the chromium coatings within the range of intermediate

coating ($40 < d \leq 184$ μm) may results in excessive damage compared to thinner and thicker coatings. This work includes information to conduct a study on optimization grinding process of hard chromium coatings.

6.1 Recommendations for Future Work

A study that examines a wider range of chromium coating thickness should be carried out to identify the optimal coating thickness in terms of mechanical damage. In terms of thermal damage, a wider range of heating temperatures can help determine the temperature at which the coating thermally fails. Covering a larger area of the substrate by FIB circles can provide more strain contours. Sometimes steel substrates are shot peened before chromium plating, which may change the surface roughness. Therefore, it would be interesting to investigate the effect of surface roughness on chromium coating adhesion, mechanical properties, and mechanical failure. A material model should be built using finite element method for more analysis of the damage. The finite element model should be able to determine the critical loads at which cracks initiate for all the damage modes. It should also be capable of identifying the optimal coating thickness at which damage is minimized. Utilizing the results of the thermal damage investigation, an optimization of the grinding process parameters can be carried out.

References

[1] H. Geng, “Finishing metal surfaces,” *Manuf. Eng. Handb.*, p. 35, 2004.

[2] R. Guffie, *The handbook of hard chromium plating*. Cincinnati Ohio (6600 Clough Pike Cincinnati 45244-4090): Gardner Publications, 1986.

[3] K. Newby, “Functional Chromium Plating,” *Met. Finish. -NEW JERSEY-*, vol. 91, no. 1, 1993.

[4] C. Cotell, *Surface engineering*. Materials Park OH: ASM International, 1994.

[5] N. Mandich, “Electrodeposition of Chromium,” pp. 205 – 248, 2011.

[6] G. Dubpernell, “Chromium Plating,” *Trans. Electrochem. Soc.*, vol. 80, no. 1, 1941.

[7] C. Snavely, “A Theory for the Mechanism of Chromium Plating A Theory for the Physical Characteristics of Chromium Plate,” *Trans. Electrochem. Soc.*, vol. 92, no. 1, 1947.

[8] J. K. DENNIS and T. E. SUCH, *Nickel and Chromium Plating*. Elsevier, 1993.

[9] R. Cook, “Direct Observation and Analysis of Indentation Cracking in Glasses and Ceramics,” *J. Am. Ceram. Soc.*, vol. 73, no. 4, pp. 787 – 817, 1990.

[10] C. Jinju, “Indentation-based methods to assess fracture toughness for thin coatings,” *J. Phys. D. Appl. Phys.*, vol. 45, no. 20, 2012.

[11] F. Frank, “On the Theory of Hertzian Fracture,” *Proc. R. Soc. A Math. Phys. Eng. Sci.*, vol. 299, no. 1458, pp. 291 – 306, 1967.

[12] S. Chen, “Contact mechanics of Hertzian cone cracking,” *Int. J. solids Struct.*, vol. 32, no. 3/4, 1995.

[13] B. Lawn, “Indentation of Ceramics with Spheres: A Century after Hertz,” *J. Am. Ceram. Soc.*, vol. 81, no. 8, pp. 1977 – 1994, 1998.

[14] A. Pajares, “Mechanical characterization of plasma sprayed ceramic coatings on metal substrates by contact testing.” Elsevier.

[15] B. Lawn, “Use of contact testing in the characterization and design of all-ceramic

crownlike layer structures: a review.," *J. Prosthet. Dent.*, vol. 86, no. 5, pp. 495 – 510, 2001.

[16] B. Lawn, *Fracture of brittle solids*. Cambridge [etc.]: Cambridge University Press, 1993.

[17] B. Lawn, "Indentation fracture: principles and applications," *J. Mater. Sci.*, vol. 10, no. 6, pp. 1049 – 1081, 1975.

[18] B. Lawn, "Hertzian Fracture in Single Crystals with the Diamond Structure," *J. Appl. Phys.*, vol. 39, no. 10, 1968.

[19] K. S. Lee, S. K. Lee, B. R. Lawn, and D. K. Kim, "Contact Damage and Strength Degradation in Brittle/Quasi-Plastic Silicon Nitride Bilayers," *J. Am. Ceram. Soc.*, vol. 81, no. 9, pp. 2394–2404, Jan. 2005.

[20] J. Malzbender, "Measuring mechanical properties of coatings: a methodology applied to nano-particle-filled sol–gel coatings on glass," *Mater. Sci. Eng. R Reports*, vol. 36, no. 2–3, pp. 47 – 103, 2002.

[21] Y. Deng, "Characterization of damage modes in dental ceramic bilayer structures," *J. Biomed. Mater. Res.*, vol. 63, no. 2, pp. 137 – 145, 2002.

[22] Y. G. Jung, S. Wuttiphan, I. M. Peterson, and B. R. Lawn, "Damage modes in dental layer structures.," *J. Dent. Res.*, vol. 78, no. 4, pp. 887–97, 1999.

[23] K. S. Lee, S. Wuttiphan, X.-Z. Hu, S. K. Lee, and B. R. Lawn, "Contact-Induced Transverse Fractures in Brittle Layers on Soft Substrates: A Study on Silicon Nitride Bilayers," *J. Am. Ceram. Soc.*, vol. 81, no. 3, pp. 571–580, Jan. 2005.

[24] H. Chai, "Fracture modes in brittle coatings with large interlayer modulus mismatch," *J. Mater. Res. -PITTSBURGH-*, vol. 14, no. 9, pp. 3805 – 3817, 1999.

[25] H. Chai, "Transverse fracture in thin-film coatings under spherical indentation," *Acta Mater.*, vol. 53, no. 2, pp. 487 – 498, 2005.

[26] A. C. Fischer-Cripps, B. R. Lawn, A. Pajares, and L. Wei, "Stress Analysis of Elastic-Plastic Contact Damage in Ceramic Coatings on Metal Substrates," *J. Am. Ceram. Soc.*, vol. 79, no. 10, pp. 2619–2625, Aug. 2005.

[27] W. Chen, "Modeling elasto-plastic indentation on layered materials using the equivalent inclusion method," *Int. J. Solids Struct.*, vol. 47, no. 20, pp. 2841 – 2854, 2010.

[28] C. Hardy, C. N. Baronet, and G. V. Tordion, "The elasto-plastic indentation of a half-space by a rigid sphere," *Int. J. Numer. Methods Eng.*, vol. 3, no. 4, pp. 451–462, Oct. 1971.

[29] X.-L. Gao, X. N. Jing, and G. Subhash, “Two new expanding cavity models for indentation deformations of elastic strain-hardening materials,” *Int. J. Solids Struct.*, vol. 43, no. 7–8, pp. 2193–2208, Apr. 2006.

[30] H. Chai, “Fracture mode transitions in brittle coatings on compliant substrates as a function of thickness,” *J. Mater. Res.*, vol. 19, no. 06, pp. 1752 – 1761, 2004.

[31] M. B. Bush, “Simulation of contact-induced fracture,” *Eng. Anal. Bound. Elem.*, vol. 23, no. 1, pp. 59–66, Jan. 1999.

[32] L. An, “Damage-resistant alumina-based layer composites,” *J. Mater. Res.*, vol. 11, no. 01, pp. 204 – 210, 1996.

[33] H. Chai, “Fracture mechanics analysis of thin coatings under plane-strain indentation,” *Int. J. Solids Struct.*, vol. 40, no. 3, pp. 591 – 610, 2003.

[34] R. Serway, *Physics for scientists & engineers*. Philadelphia: Saunders College Pub., 1990.

[35] Y. Fei, “Thermal expansion,” *Miner. Phys. Crystallogr. - A Handb. Phys. Constants, AGU Ref. shelf 2.*, vol. 2, pp. 29–44, 1995.

[36] *Heat treating*. Metals Park Ohio: American Society for Metals, 1981.

[37] A. N. Khan, J. Lu, and H. Liao, “Heat treatment of thermal barrier coatings,” *Mater. Sci. Eng. A*, vol. 359, no. 1–2, pp. 129–136, Oct. 2003.

[38] V. Teixeira, M. Andritschky, W. Fischer, H. P. Buchkremer, and D. Stöver, “Effects of deposition temperature and thermal cycling on residual stress state in zirconia-based thermal barrier coatings,” *Surf. Coatings Technol.*, vol. 120–121, pp. 103–111, Nov. 1999.

[39] W. C. Oliver and G. M. Pharr, “An improved technique for determining hardness and elastic modulus using load and displacement sensing indentation experiments,” *J. Mater. Res.*, vol. 7, no. 06, pp. 1564–1583, Jan. 2011.

[40] *Standard test method for Knoop and Vickers hardness of materials.* West Conshohocken PA: ASTM International, 2010.

[41] A. Fischer-Cripps, *The IBIS handbook of nanoindentation*. Forestville NSW: Fischer-Cripps Laboratories, 2009.

[42] P. S. Prevéy, “X-ray diffraction residual stress techniques,” *Met. Handbook. 10. Met. Park*, no. 513, pp. 380–392, 1986.

[43] N. Do, “The significance and determination by image analysis of microcrack density in hard chromium plating,” *Plat. Surf. Finish.*, vol. 95, no. 4, pp. 36 – 42, 2008.

[44] *Standard Guide for Engineering Chromium Electroplating*. 2011.

[45] L. Vernhes, "Alternatives for hard chromium plating: Nanostructured coatings for severe-service valves," *Mater. Chem. Phys.*, vol. 140, no. 2–3, pp. 522 – 528, 2013.

[46] M. Ashby, *Materials selection in mechanical design*. Amsterdam: Butterworth-Heinemann, 2011.

[47] W. Pfeiffer, "Residual stresses and strength of hard chromium coatings," *Mater. Sci. Forum*, vol. 681, pp. 133 – 138, 2011.

[48] K. Johnson, *Contact mechanics*. Cambridge [Cambridgeshire] ;;New York: Cambridge University Press, 1985.

[49] J. Lackner, "Tribology and Micromechanics of Chromium Nitride Based Multilayer Coatings on Soft and Hard Substrates," *Coatings*, vol. 4, no. 1, pp. 121 – 138, 2014.

[50] I. M. Peterson, A. Pajares, B. R. Lawn, V. P. Thompson, and E. D. Rekow, "Mechanical characterization of dental ceramics by hertzian contacts," *J. Dent. Res.*, vol. 77, no. 4, pp. 589–602, 1998.

Appendix A

Mechanical Damage

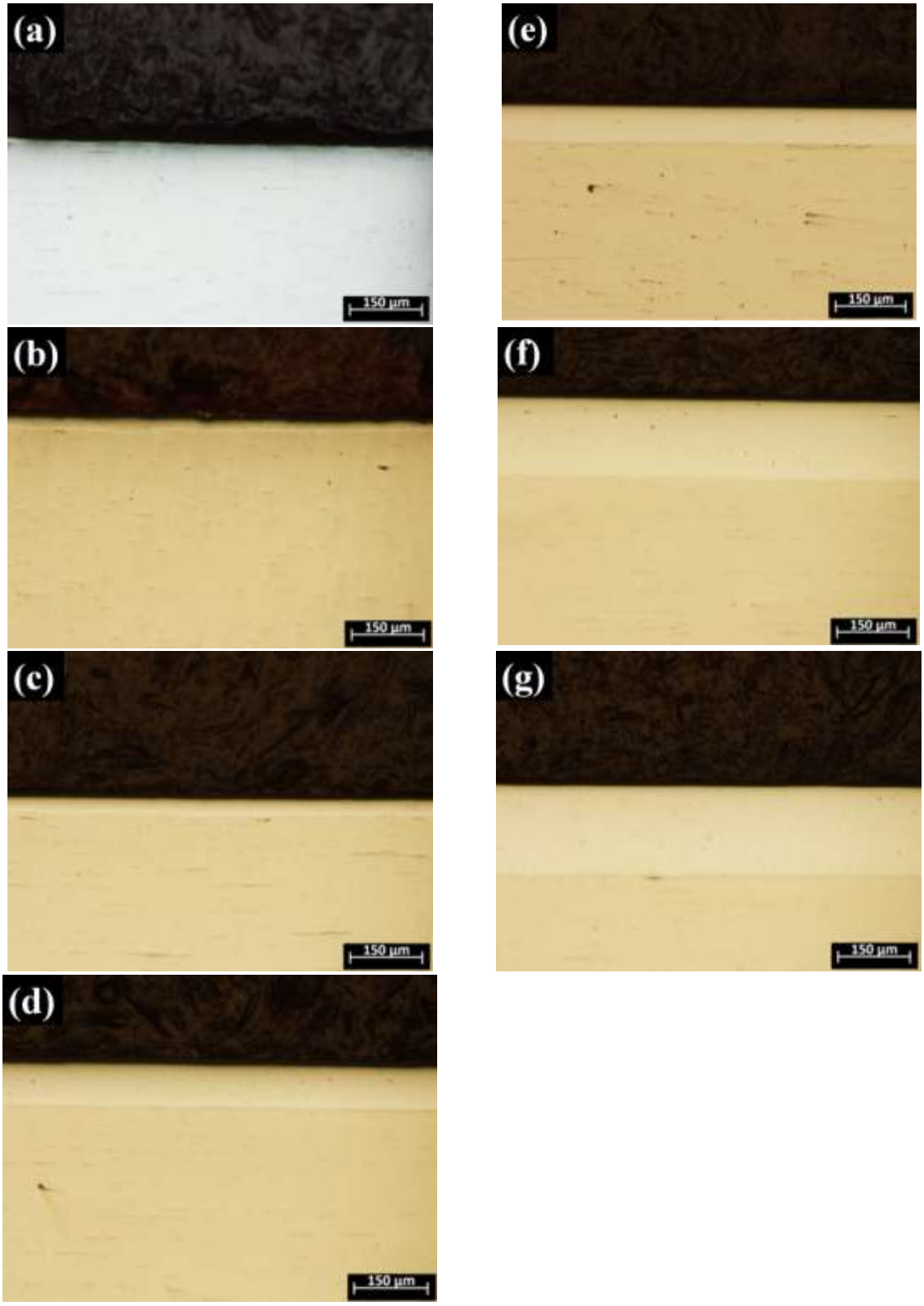

Figure A-1 **Cross-sections of a chromium coating plated for (a) 2 h, (b) 10 h, (c) 12 h, (d) 14 h, (e) 16 h, (f) 20 h and (g) 25 h.**

Thickness (μm)	60 kg	100 kg	150 kg
11	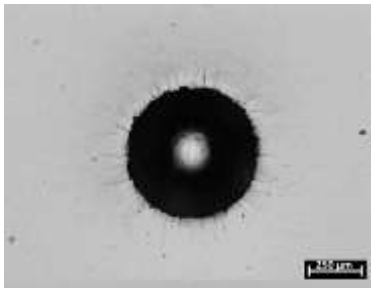	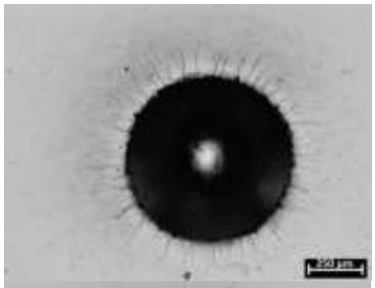	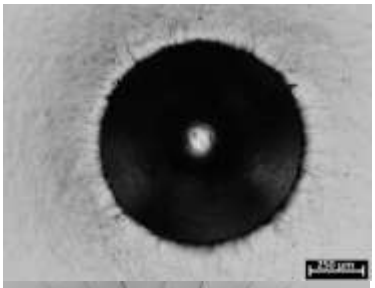
40	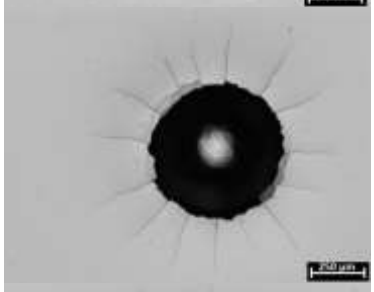	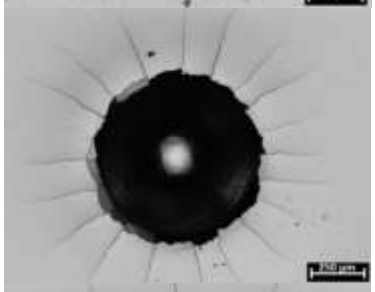	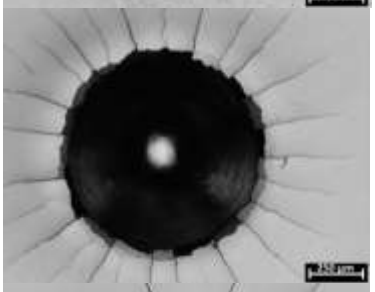
87	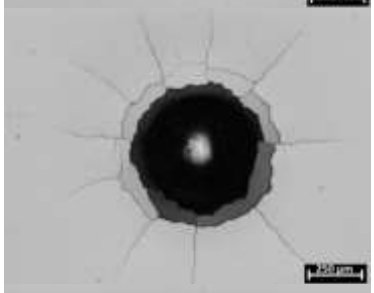	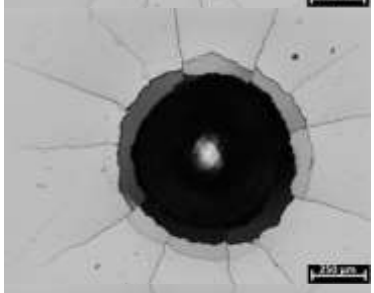	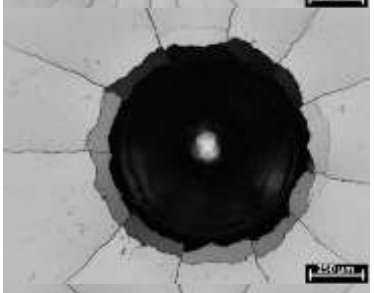
100	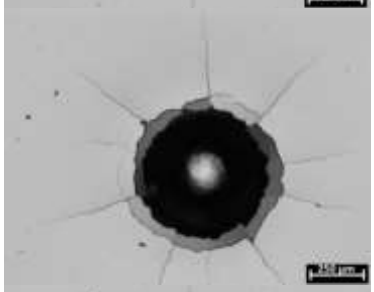	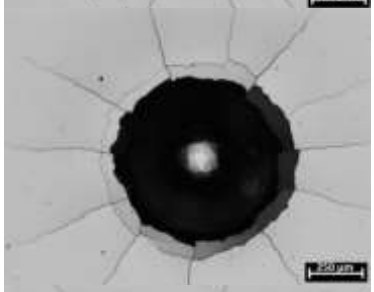	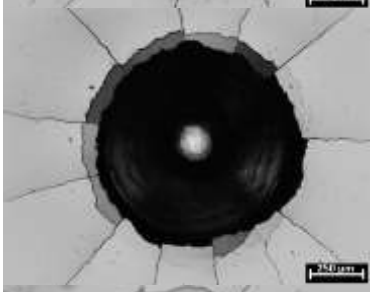
167	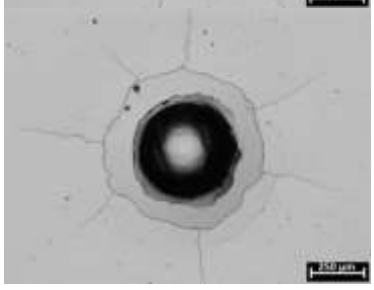	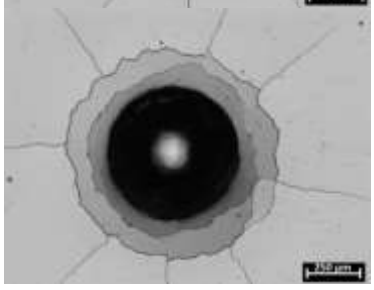	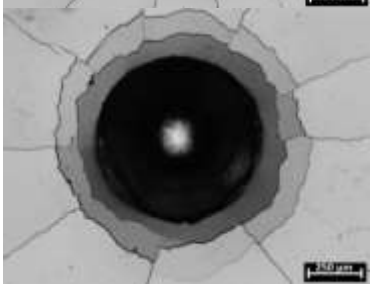

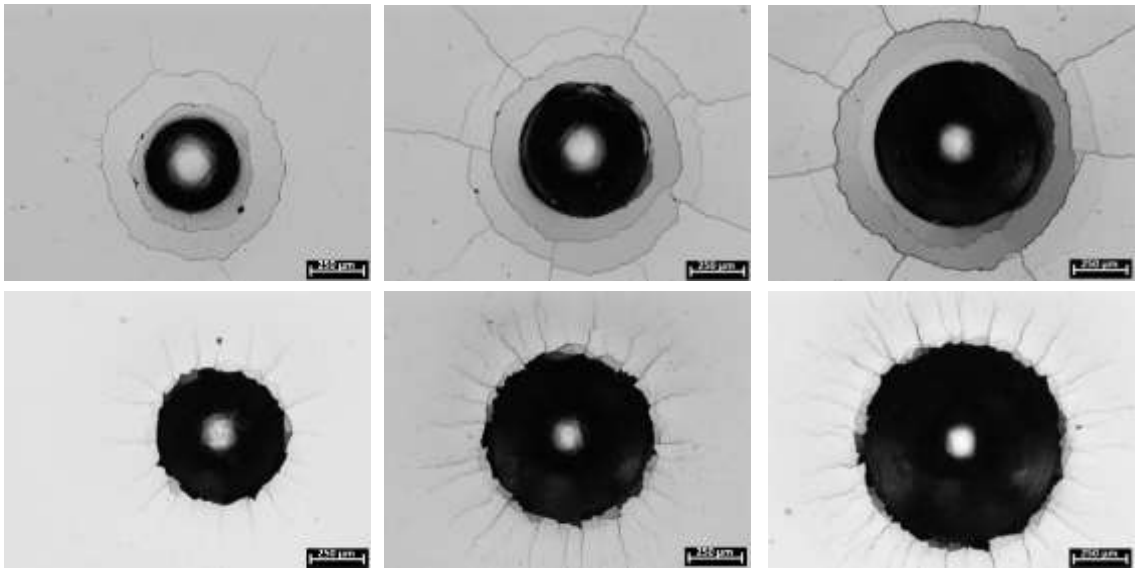

Figure A-2 **Optical micrographs showing cracking pattern of chromium coating surface indented with a sphere under various loads for different coating thickness.**

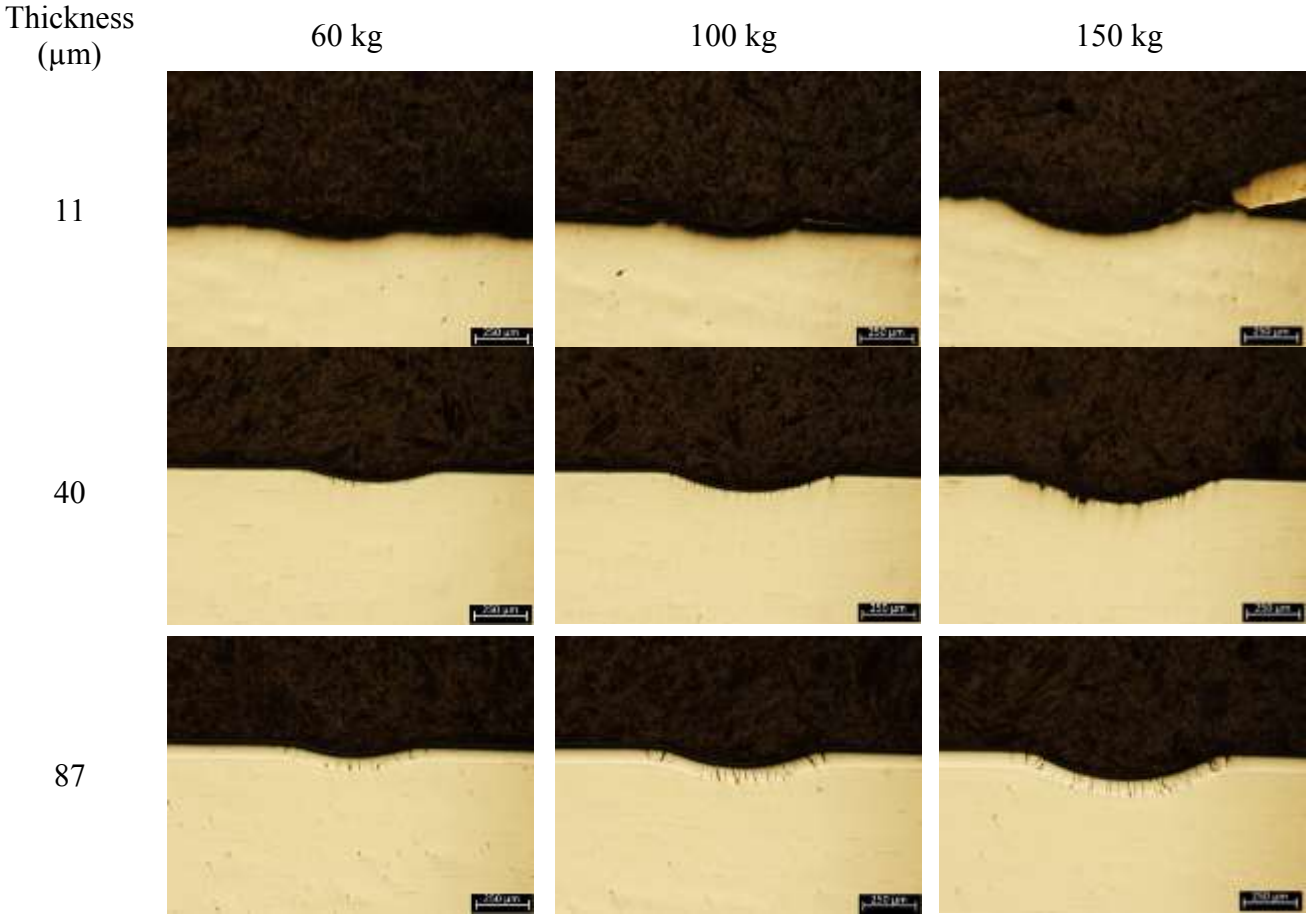

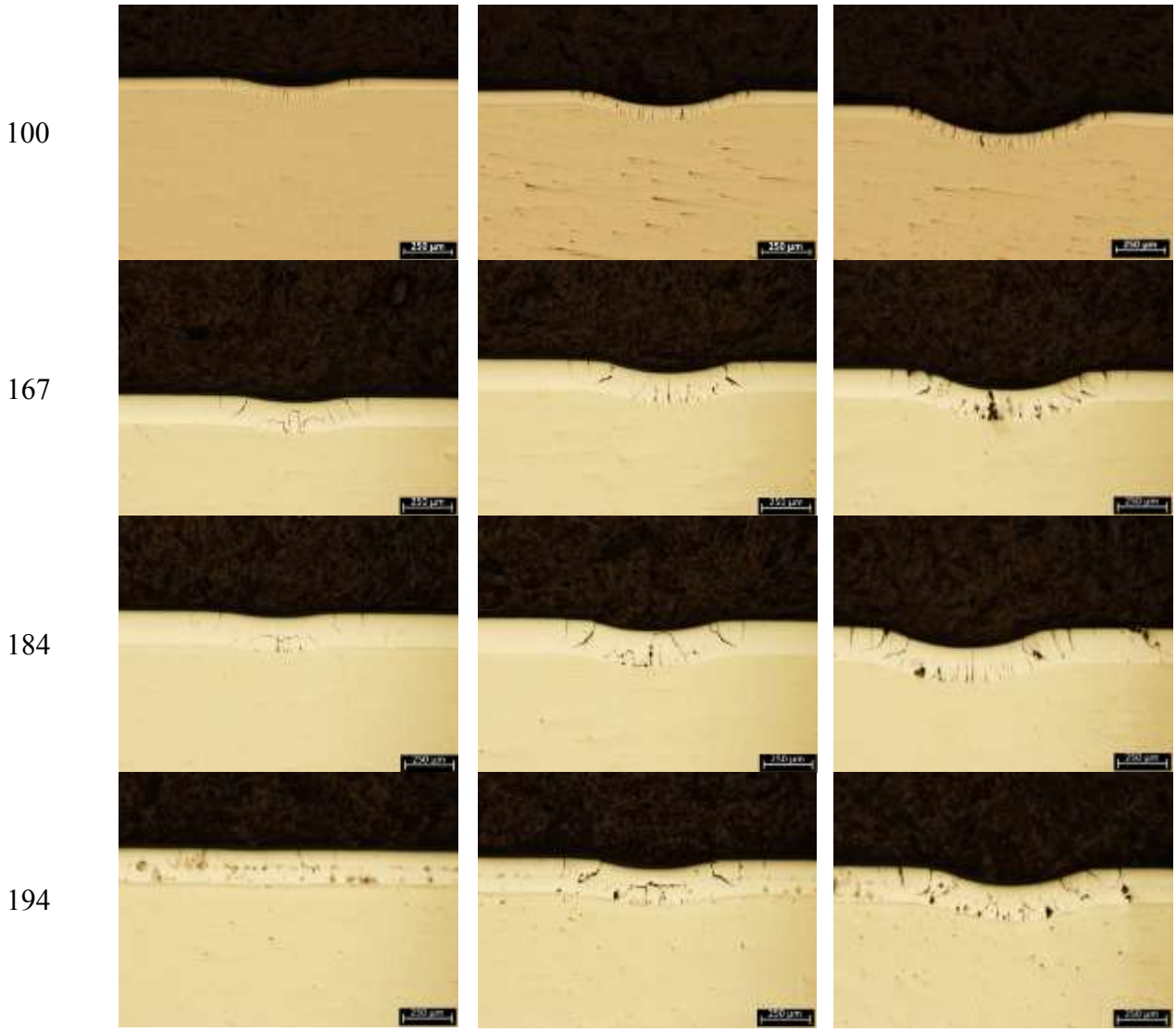

Figure A-3 **Optical micrographs showing cross-sections of chromium coating indented with a sphere under various loads for different coating thickness.**